The Sun as an X-ray Star: Spectral Models of Solar Coronal Regions and Their Application to Stellar Coronae

Dissertation

der Mathematisch-Naturwissenschaftlichen Fakultät

der Eberhard Karls Universität Tübingen

zur Erlangung des Grades eines

Doktors der Naturwissenschaften

(Dr. rer. nat.)

vorgelegt von

Wilhelmina Maryann Joseph

aus Hyderabad/Indien

Tübingen

2026

Gedruckt mit Genehmigung der Mathematisch-Naturwissenschaftlichen Fakultät der Eberhard Karls Universität Tübingen.

Tag der mündlichen Qualifikation:	08.05.2026
Dekan:	Prof. Dr. Thilo Stehle
1. Berichterstatterin:	Prof. Dr. Beate Stelzer
2. Berichterstatter:	Prof. Dr. Andrea Santangelo

Contents

Abstract

Understanding stellar coronae requires connecting the integrated X-ray emission I observe from unresolved stars to the physical magnetic structures producing that emission. The Sun uniquely enables this connection: I can observe both its spatially resolved coronal structures and its integrated X-ray spectrum as it would appear from a stellar distance. This dissertation develops a new implementation of the "Sun as an X-ray Star" (SaXS) methodology that directly retrieves the surface coverage (filling factors) of different coronal region types—background corona, active regions, cores, and flares—from X-ray spectral fitting.

I construct spectral models for XSPEC from emission measure distributions derived from *Yohkoh* observations of solar coronal regions. Each region type becomes a multi-temperature model with fixed temperature structure and free normalization corresponding to its projected surface area. This direct fitting approach eliminates the computational overhead of synthetic spectral grids while providing transparent physical interpretation: fitted normalizations immediately yield filling factors without intermediate parameter-space matching.

I validate the method on the Sun itself using full-disk soft X-ray spectra from the DAXSS (Dual Aperture X-ray Solar Spectrometer) CubeSat instrument at two activity levels. Comparing spectral-fit-derived filling factors with the actual spatial distribution visible in contemporaneous *Hinode*/XRT images demonstrates that the method successfully recovers known coronal structure. The quiescent Sun shows ∼21% active region coverage (with refined fits using vari-

able abundances), while flaring periods show $\sim$15% active region coverage, $\sim$3% core coverage, and $\sim$0.07% flare coverage (with refined fits using variable abundances and non-equilibrium ionization for flares). Spectral filling factors systematically exceed image-based measurements because spectra naturally include limb emission extending to coronal scale heights, providing a more complete picture of total coronal output as seen from stellar distances.

Application to AD Leo, a nearby active M3.5V dwarf, reveals both capabilities and limitations of solar-derived templates. During quiescent periods, the corona appears dominated by hot cores with significant background but minimal active region contribution, suggesting either fundamentally different magnetic structures or templates that incompletely capture stellar active regions. The star exhibits continuous low-level flaring even in nominally quiescent phases. The spectacular November 2021 "November 2021 Great Flare" (GOES X1445 equivalent) produces systematic high-energy residuals: even our hottest solar flare template (X9.0, $\sim$30 MK) cannot reproduce emission above 2–3 keV. Adding thermal components reaching several tens of MK eliminates residuals, demonstrating that AD Leo's superflares produce plasma significantly hotter than any solar analog.

This analysis reveals a fundamental degeneracy in X-ray spectral analysis: for fixed emission measure, electron density and filling factor trade off (EM $\propto n_e^2 f$). Initial density estimates from literature extrapolation yielded unphysically small filling factors, requiring iterative density refinement constrained by the requirement that regions occupy at least one coronal loop's projected area. Breaking this degeneracy definitively requires independent density measurements from high-resolution spectroscopy, underscoring the importance of complementary observations for future applications.

The dissertation establishes that solar-derived spectral models can characterize stellar coronae in terms of physical magnetic structures, validates the filling factor retrieval methodology through direct comparison with spatially resolved solar observations, and identifies critical limitations—particularly the need for expanded emission measure libraries extending to super-solar temperatures and independent density constraints—that must be addressed for robust application to active stellar populations.

Zusammenfassung

Um stellare Koronen zu verstehen, ist es notwendig, die integrierte Röntgenemission unaufgelöster Sterne mit den physikalischen Magnetstrukturen die diese Emission erzeugen zu verknüpfen.

Die Sonne ermöglicht diese Verknüpfung auf einzigartige Weise: Ich kann sowohl ihre räumlich aufgelösten Koronastrukturen als auch ihr integriertes Röntgenspektrum beobachten, so wie es aus stellarer Entfernung erscheinen würde. Diese Dissertation entwickelt eine neue Implementierung der „Sun as an X-ray Star“ (SaXS)-Methodik, die den Flächenanteil (Füllfaktoren) verschiedener Koronaregionstypen—Hintergrundkorona, aktive Regionen, Kerne und Flares—direkt aus der Anpassung von Röntgenspektren bestimmt.

Ich konstruiere Spektralmodelle für XSPEC aus Emissionsmaßverteilungen, die aus *Yohkoh*-Beobachtungen solarer Koronaregionen abgeleitet wurden. Jeder Regionstyp wird zu einem Mehr-Temperatur-Modell mit fester Temperaturstruktur und freier Normierung, die seiner projizierten Oberflächenfläche entspricht. Dieser direkte Anpassungsansatz eliminiert den Rechenaufwand synthetischer Spektralraster und bietet gleichzeitig eine transparente physikalische Interpretation: Die angepassten Normierungen liefern unmittelbar Füllfaktoren ohne zwischengeschalteten Parameterraum-Abgleich.

Ich validiere die Methode an der Sonne selbst mithilfe von Röntgenspektren der gesamten Sonnenscheibe aufgenommen mit dem DAXSS (Dual Aperture X-ray Solar Spectrometer) CubeSat-Instrument bei zwei Aktivitätsniveaus. Der Vergleich der spektral bestimmten Füllfaktoren mit der tatsächlichen räum-

lichen Verteilung, die in zeitgleichen *Hinode*/XRT-Aufnahmen sichtbar ist, zeigt, dass die Methode die bekannte Koronastruktur erfolgreich reproduziert. Die Sonne weist in der ruhigen Phase eine Bedeckung durch aktive Regionen von $\sim$21% auf (bei verfeinerten Anpassungen mit variablen Häufigkeiten), während Flare-Perioden eine Bedeckung durch aktive Regionen von $\sim$15%, durch Kerne von $\sim$3% und durch Flares von $\sim$0,07% zeigen (bei verfeinerten Anpassungen mit variablen Häufigkeiten und Nicht-Gleichgewichts-Ionisation für Flares). Spektrale Füllfaktoren übersteigen systematisch bildbasierte Messungen, da Spektren auf natürliche Weise die Limb-Emission einschließen, die sich bis zu koronalen Skalenhöhen erstreckt, und damit ein vollständigeres Bild der gesamten Koronaemission aus stellarer Perspektive liefern.

Die Anwendung auf AD Leo, einen nahen aktiven M3.5V-Zwergstern, zeigt sowohl die Möglichkeiten als auch die Grenzen solar abgeleiteter Vorlagen. In ruhigen Phasen wird die Korona von heißen Kernen dominiert, mit erheblichem Hintergrundanteil aber minimalem Beitrag aktiver Regionen, was entweder auf grundlegend andere Magnetstrukturen oder auf Vorlagen hindeutet, die stellare aktive Regionen unvollständig erfassen. Der Stern zeigt auch in nominell ruhigen Phasen kontinuierliche schwache Flare-Aktivität. Die spektakuläre „Große Flare vom November 2021" (GOES X1445-Äquivalent) erzeugt systematische Residuen bei hohen Energien: Selbst unsere heißeste solare Flare-Vorlage (X9.0, $\sim$30 MK) kann die Emission oberhalb von 2–3 keV nicht reproduzieren. Das Hinzufügen thermischer Komponenten mit Temperaturen von mehreren zehn MK eliminiert die Residuen und zeigt, dass die Superflares von AD Leo Plasma erzeugen, das deutlich heißer ist als jedes solare Analogon.

Diese Analyse offenbart eine grundlegende Entartung in der Röntgenspektralanalyse: Bei festem Emissionsmaß tauschen Elektronendichte und Füllfaktor gegeneinander aus (EM $\propto n_e^2 f$). Anfängliche Dichteschätzungen aus der Literatur lieferten unphysikalisch kleine Füllfaktoren und erforderten eine iterative Dichtekorrektur, die durch die Bedingung eingeschränkt wird, dass Regionen mindestens die projizierte Fläche einer koronalen Magnetschleife einnehmen müssen. Eine endgültige Auflösung dieser Entartung erfordert unabhängige Dichtemessungen aus hochauflösender Spektroskopie, was die Bedeutung komplementärer Beobachtungen für künftige Anwendungen unterstreicht.

Die Dissertation zeigt, dass solar abgeleitete Spektralmodelle eine Charakterisierung stellarer Koronen anhand ihrer magnetischen Strukturen ermöglichen, validiert die Methodik zur Bestimmung von Füllfaktoren durch direkten Vergleich mit räumlich aufgelösten Sonnenbeobachtungen und identifiziert kritische Einschränkungen—insbesondere den Bedarf an erweiterten Emissionsmaßbibliotheken, die bis zu übersolaren Temperaturen reichen, sowie unabhängige Dichtebeschränkungen-die für eine robuste Anwendung auf aktive Sternpopulationen adressiert werden müssen.

1 Introduction

Every solar eclipse, as the darkness of the Moon subdues the brightness of the Sun, a phenomenon that usually eludes the naked eye reveals itself. Delicate arcs manifest, and striking tendrils of light sweep far out from behind the darkness (Fig. 1.1). Recorded in writing as early as 968 CE (Stephenson et al., 1997), these wispy features belong to none other than the still elusive outermost layer of the solar atmosphere: the solar corona.

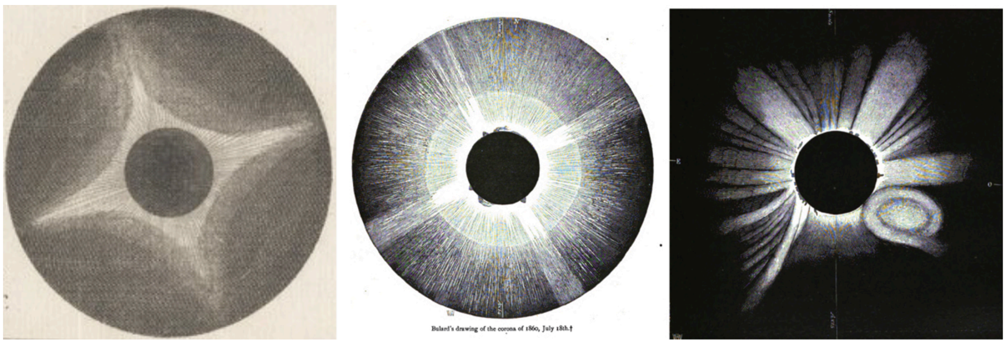

Figure 1.1: Historical drawings of the solar corona observed during total solar eclipses, showing the characteristic streamers, plumes, and extended structures that have captivated astronomers for over a millennium. These observations revealed the corona's complex morphology long before X-ray and EUV observations connected these structures to magnetic field lines (Hayakawa et al., 2021). Licensed under CC BY 4.0.

The greatest mystery surrounding the solar corona lies in its anomalously high temperatures. The visible surface of the Sun, the photosphere, rests at a mere 5,800 K. Yet moving upward through the solar atmosphere into the chromosphere and transition region, rather than cooling as thermodynamics would dictate, the temperature rises dramatically: first to tens of thousands of Kelvin, then to millions of Kelvin before reaching the hottest region of all, the solar corona itself, at several million Kelvin (Fig. 1.2).

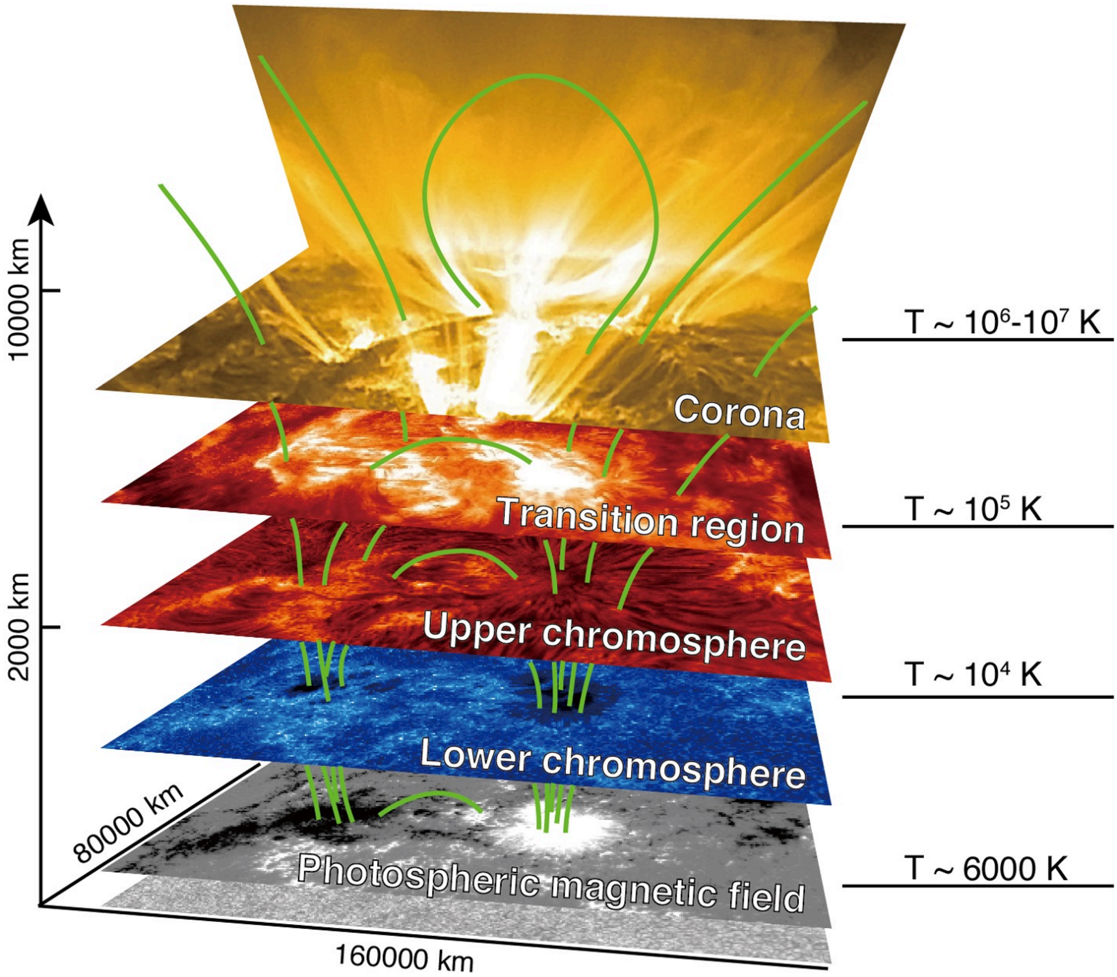

Figure 1.2: Structure of the solar atmosphere showing the photosphere, chromosphere, transition region, and corona connected by magnetic field lines. Temperature increases counterintuitively from the photosphere (∼6,000 K) through the transition region to the corona (several million K). The corona's hot, tenuous plasma is confined and structured by magnetic loops anchored at the photosphere. Credit: Solar images from NAOJ/JAXA and NASA.

This inverted temperature profile, growing hotter with distance from the heat source, violates our intuitive understanding of heat flow. The mechanism responsible for heating the corona to such extreme temperatures remains one of the major unsolved problems in solar physics (Klimchuk, 2006).

The key to understanding this phenomenon lies in the corona's magnetic architecture. When observed in X-rays (by spacecraft like *Yohkoh* and *Hinode*) or extreme ultraviolet wavelengths (e.g., by instruments aboard the Solar Dynamics Observatory), the corona reveals a complex network of magnetic structures: loops, arcs, and streamers threading through space, all anchored to the photosphere below. These coronal loops appear far brighter and hotter than the surrounding diffuse plasma, indicating that magnetic fields play a central role in the corona's heating.

These magnetic structures evolve continuously in response to the churning convection beneath the Sun's surface, and their behavior is closely tied to the solar activity cycle (Hathaway, 2010). During solar maximum, when sunspots proliferate across the photosphere, magnetic loops emerge in abundance, the corona brightens in X-rays, and flares (violent releases of magnetic energy) erupt with increasing frequency. During solar minimum, sunspots diminish, magnetic structures become less prominent, and the corona grows quieter. Understanding the magnetic field is clearly essential to understanding not just the corona's heat, but its structure and evolution.

The Sun's corona is not unique. X-ray observations from satellites like ROSAT, *XMM-Newton* (X-ray Multi-Mirror Mission), and Chandra have revealed that cool stars (those of spectral types F, G, K, and M) possess coronae of their own, with temperatures reaching or even exceeding the Sun's several million Kelvin (Güdel et al., 2004; Pizzolato et al., 2003). More active stars show brighter X-ray emission, higher flare rates, and stronger chromospheric emission, mirroring the Sun's behavior through its 11-year cycle. Yet there is a fundamental observational difference: while I can resolve the Sun's surface and map its magnetic structures in detail, other stars appear as point sources. Their coronae remain unresolved, their X-ray emission an integrated signal from regions spanning vast ranges in temperature and density. I observe stellar spectra and light curves, but the physical structures producing that emission (the loops, active regions, and flares) remain hidden from direct view.

This observational limitation is particularly important when studying M dwarfs, the galaxy's most abundant stellar population. Comprising roughly 75% of all stars (Bochanski et al., 2010; Henry et al., 2006) and hosting many discovered exoplanets, including planets within habitable zones where liquid water might exist, M dwarfs exhibit intense magnetic activity despite their small size and cool photospheres. They flare frequently and energetically, maintain high X-ray luminosities relative to their total light output, and generate strong chromospheric emission. This intense activity poses a direct threat to any nearby planets: frequent flares deliver high-energy radiation capable of dissociating atmospheric molecules, while coronal mass ejections (large-scale eruptions of plasma and magnetic field that often accompany flares) can strip away planetary atmospheres through sustained bombardment (Airapetian et al., 2017; Lammer et al., 2007; Segura et al., 2010). Understanding M dwarf magnetic activity is therefore crucial for assessing whether planets in their habitable zones could actually support life.

Yet how can I characterize stellar coronae when I cannot see their individual structures? Current stellar activity metrics (X-ray luminosity, the ratio of X-ray to total luminosity, chromospheric line strengths, rotation periods) are phenomenological measures that indicate how active a star is without revealing what that activity looks like physically. They do not tell us whether a star's corona is dominated by stable active regions or transient flares, whether hot bright cores or diffuse background plasma fills its magnetic structures. The fundamental question is whether I can diagnose stellar coronae in terms of the actual magnetic features I observe on the Sun (active regions, cores, flares) rather than relying solely on empirical correlations.

The answer lies in the Sun itself. Only for our star can I simultaneously observe both the integrated X-ray emission (as I would for any distant star) and the spatially resolved structures producing that emission. This unique position enables "Sun-as-a-star" experiments: I can treat the Sun as if it were unresolved, synthesizing what its spectrum would look like from a great distance, and test whether analysis methods designed for stars can recover the solar coronal properties I already know from imaging. If stellar coronae are structured like the

Sun's, if they too contain background corona, active regions, cores, and flares in varying proportions, then solar-derived models should provide a framework for interpreting unresolved stellar observations.

This insight motivated the original "Sun as an X-ray Star" (SaXS) methodology, developed in the early 2000s (Orlando et al., 2000, 2001, 2004; Peres et al., 2000; Reale et al., 2001). They extracted emission measure distributions (EMDs) (quantifications of how much plasma exists at each temperature) for different solar coronal region types (quiet background, active regions, cores, flares) from spatially resolved *Yohkoh* soft X-ray telescope observations.Building on these templates, later work (Coffaro et al., 2022; Orlando et al., 2017) synthesized stellar-like spectra by combining the solar regions in various proportions, then fitted those synthetic spectra with simple thermal models to derive average temperatures and luminosities. Comparing these synthetic temperature-luminosity pairs with actual stellar observations allowed them to infer which combination of solar regions best matched a given star. The approach successfully demonstrated that stellar coronae could be understood in terms of solar structures, but required extensive grids of synthetic spectra and parameter-space matching to infer the filling factors (fractional surface coverage) of each region type.

This dissertation takes a different approach. Rather than generating synthetic spectra and inferring filling factors indirectly through parameter-space matching, I construct spectral models directly from the solar EMDs and implement them as fitting components in XSPEC, the standard X-ray spectral analysis software. Each coronal region type (background corona, active regions, cores, and flares; see Sect. 2.2) becomes a multi-temperature model with a fixed temperature structure (derived from the solar template) and a free normalization that corresponds directly to the projected area that region occupies on the stellar surface. Fitting observed spectra with these models retrieves the filling factors immediately from the model normalizations. This direct spectral-fitting approach eliminates the computational overhead of synthetic grids while providing a more transparent physical interpretation: the fitted normalizations indicate, without intermediate steps, how much of the star's visible surface is covered by each type of coronal structure.

I validate this approach where validation is possible: on the Sun itself. Using full-disk soft X-ray spectra from DAXSS (the Dual Aperture X-ray Solar Spectrometer aboard the INSPIRESat-1 CubeSat) at two activity levels, one relatively quiescent, one during a flaring period, I fit our solar-derived models and extract filling factors. I then compare these spectral-fit-derived filling factors with the actual spatial distribution of coronal regions visible in contemporaneous full-disk images from *Hinode*'s X-Ray Telescope. This represents the first direct validation of SaXS filling factor retrieval against spatially resolved imaging, demonstrating that the method successfully reproduces observed coronal structure.

With the method validated on solar data, I apply it to a star where spatially resolved imaging is not currently available: AD Leo, a nearby M dwarf of spectral type M3.5V known for its intense magnetic activity and frequent, powerful flares. I analyze a single *XMM-Newton* observation spanning both quiescent periods and the spectacular "November 2021 Great Flare" of November 2021—a superflare reaching X1445 class on the GOES flux scale (where X-class flares represent the most energetic category, with X1 flares having peak flux of 10^{-4} W m^{-2} in the 1–8 Å band, and each number denoting a tenfold increase)—that severely tests the limits of solar-derived templates.

The solar validation confirms that the method successfully recovers filling factors consistent with the spatial distribution of coronal structures visible in *Hinode* images, providing the first direct test of SaXS filling factor retrieval against spatially resolved imaging. Applied to AD Leo, the method reveals a corona dominated by hot, bright cores even during quiescent periods, while the November 2021 Great Flare exposes the limits of solar-derived templates: the most energetic events produce plasma significantly hotter than anything observed in solar flares. These results demonstrate both the diagnostic power of the SaXS approach and the refinements needed to extend it to the most active stellar coronae.

The remainder of this dissertation proceeds as follows. Chapter 2 provides the theoretical and observational foundation: the physics of coronal loops and magnetic heating, the solar dynamo and stellar activity, the taxonomy of solar coronal regions, and the instrumentation enabling both spatially resolved solar observations and stellar spectroscopy. Chapter 3 describes the construction of our XSPEC spectral models from solar EMDs and the methodology for retrieving filling factors from spectral fits. Chapter 4 presents the solar validation using DAXSS spectra and *Hinode* images at two activity levels, demonstrating that the method successfully recovers known coronal structure. Chapter 5 details the application to AD Leo, including light curve analysis and spectral segmentation, initial fitting with solar-derived models, identification of problematic segments, development of two alternative solution approaches (frozen baseline with VAPEC components versus physical restructuring), and comprehensive discussion of methodological challenges including density refinement and abundance considerations. Section 6 provides broader context by discussing the need for an expanded EMD library, the method's applicability to different stellar types, extensions to stellar populations, theoretical developments, and the role of SaXS as an activity diagnostic. It also summarizes our contributions, discusses lessons learned and methodological improvements needed, outlines immediate next steps for solar refinement and stellar applications, and presents the long-term vision for population-level coronal characterization and theoretical framework development.

2

Background and Previous Work

2.1 | Coronal loops: fundamental plasma structures

Coronal loops are magnetically confined plasma structures formed by field lines that emerge from the photosphere and extend into the corona, with their footpoints rooted in sunspots or starspots. The interaction between plasma and magnetic field differs markedly between the photosphere and corona. In the photosphere, plasma pressure dominates (high plasma-β), allowing plasma motion to drag magnetic field lines. In contrast, the corona operates in a low plasma-β regime where magnetic pressure dominates, guiding plasma motion along field lines.

For analytical purposes, loops can be approximated as half-toruses (Reale, 2014) with a characteristic semi-length L representing the distance measured along the loop from footpoint to loop apex (Fig. 2.1). Typical geometries vary by region type (Reale, 2014): quiet or static loops (background corona, active regions; see Sect. 2.2) have $L \sim 10^9$ to 10^{10} cm, while flaring loops are more compact at $L \sim 10^9$ cm where heating is particularly intense. Loop cross-sections are typically modeled with a minor radius $r \approx 0.1L$. These geometric parameters determine the loop volume, projected area, and cooling timescales, all of which become important in later filling-factor calculations.

The physical state of plasma within loops depends strongly on whether the

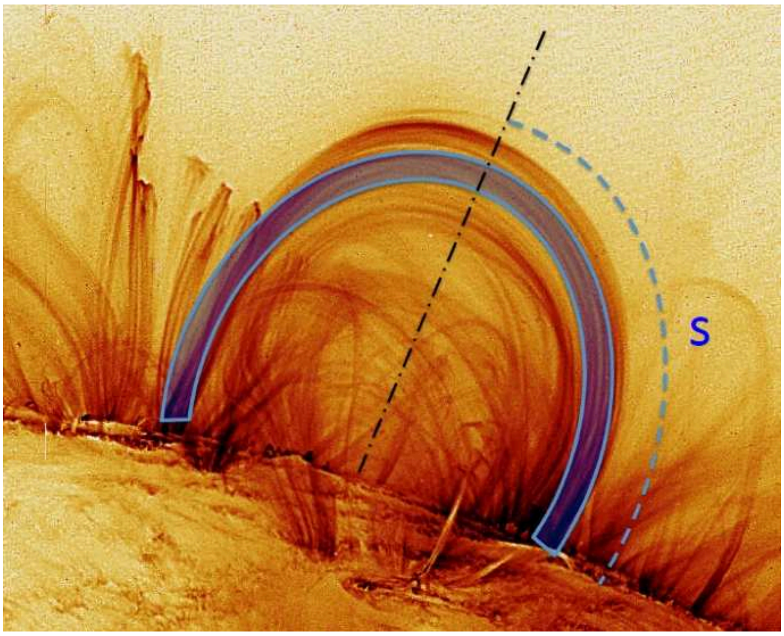

Figure 2.1: Coronal loop observed by TRACE on 6 November 1999, 2 UT, showing the loop semi-length (marked as S in the image, corresponding to our notation L). The plasma confined in a loop can be described with one-dimensional hydrodynamic modeling, with a single coordinate along the loop. Image credit: Reale (2014). Licensed under CC BY-NC 3.0 DE

structure is static or dynamic. Static or quasi-static loops, such as those in the background corona and quiet active regions, maintain thermal equilibrium where heating balances radiative and conductive cooling. These structures also achieve ionization equilibrium, meaning ionization states are determined by local temperature as collisional ionization and recombination rates balance. Such loops are long-lived (hours to days) and can be modeled as isothermal or slowly varying multi-temperature plasma in collisional ionization equilibrium (CIE).

Dynamic loops, particularly flaring loops, behave quite differently. They do not maintain thermal equilibrium; instead, they undergo rapid heating during an impulsive phase followed by cooling. In principle, these structures may require non-equilibrium ionization (NEI) treatment where ionization states lag behind rapidly changing temperatures. The timescales are much shorter: seconds to minutes for the impulsive phase, minutes to hours for decay. Whether NEI is necessary depends on the event timescale. For timescales shorter than the ionization timescale, NEI treatment is required; for longer timescales, the CIE approximation remains valid even for flares.

2.2 | Taxonomy of solar coronal region types

I can classify solar coronal structures into several distinct types based on their physical characteristics, as illustrated in Fig. 2.2.The following regions have been classified as such by Orlando et al. 2000, Reale et al. 2001, and Peres et al. 2000. The quiet Sun or background corona (BKC) consists of diffuse emission from low-lying, low-temperature loops that fill the spaces between active regions. Coronal holes (CH) are regions with open magnetic field lines that do not trap plasma and appear as X-ray dark regions; they contribute negligibly to X-ray spectra and are not considered in this work. Active regions (AR) are complexes of hot coronal loops rooted in sunspot groups that appear bright in X-rays. Within these active regions, I find cores of active regions (CO), which are the hottest loop systems with the highest temperatures and emission measures. Finally, flaring loops (FL) are transiently heated and brightened loops during flare events, characterized by rapid temperature evolution (Fletcher et al., 2011; Reeves et al., 2007).

Each region type relates to underlying loop populations and magnetic topology in distinct ways.

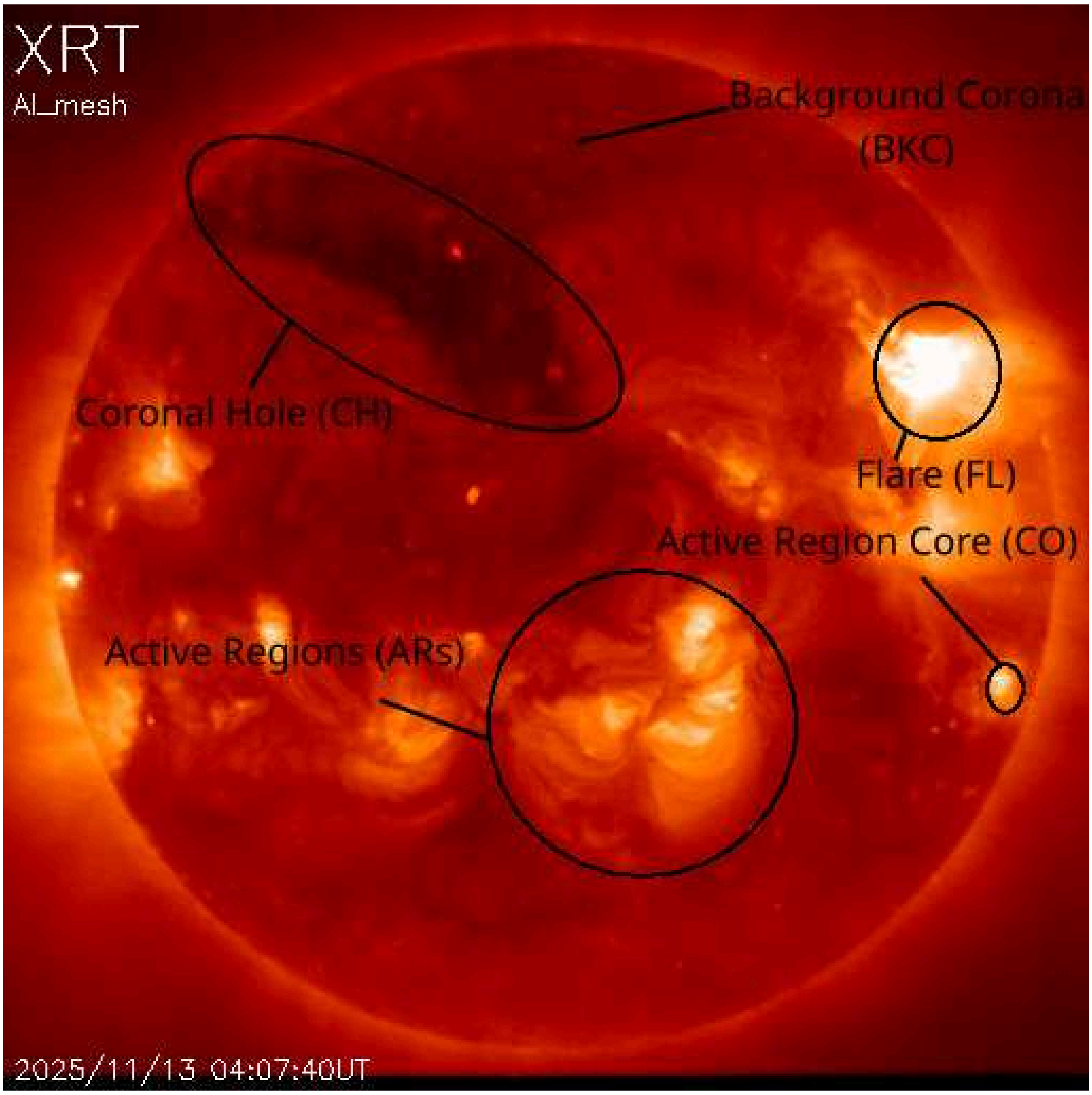

Figure 2.2: *Hinode*/XRT synoptic composite image from November 13, 2025, adapted to illustrate different coronal region types. Labeled features include: coronal holes (dark regions with open field lines), background corona (diffuse emission), active regions (bright loop complexes), active region cores (hottest, densest structures), and flares (transient brightenings). Each region type exhibits distinct thermal and morphological characteristics that form the basis of the SaXS classification scheme. Image credit: *Hinode*/XRT synoptic program, Montana State University (`https://solar.physics.montana.edu/HINODE/XRT/SCIA/daily_pages/2025/20251113_SYN.html`), adapted by the author.

2.3 | Theories of coronal heating

The fundamental question of how the corona achieves and maintains temperatures of several million Kelvin—far exceeding the photosphere's 5,800 K—remains one of solar physics' major unsolved problems (Klimchuk, 2006, 2015). While magnetic fields clearly play a central role in structuring and heating the corona, the specific mechanisms by which magnetic energy converts to thermal energy continue to be debated. Two primary mechanisms have been proposed to explain this heating.

The first, Alfvén wave heating, relies on the fact that magnetic field lines threading the corona can support Alfvén waves, which are transverse magnetohydrodynamic waves. Convective turbulence at the photosphere excites these waves, which then propagate along field lines into the corona. The wave energy dissipates through various mechanisms such as phase mixing, resonant absorption, and turbulent cascades, depositing heat into the coronal plasma.

The second mechanism involves magnetic reconnection and what is known as nanoflare heating. Stressed and twisted magnetic field lines undergo reconnection events that release stored magnetic energy. While large reconnection events produce observable flares, the nanoflare hypothesis proposes that coronal heating is actually dominated by countless small, unresolved reconnection events occurring constantly across the solar surface. Each nanoflare releases bursts of hot plasma and energetic particles into coronal loops, maintaining the high temperatures I observe.

The current consensus is that both mechanisms likely contribute to coronal heating, with their relative importance varying by location and activity level.

While these mechanisms explain the persistent heating of quasi-static coronal structures, they cannot account for the sudden, violent energy releases that characterize solar flares. Flares represent a distinct regime of magnetic energy conversion, where stressed field configurations undergo catastrophic reconnection events releasing energy far more rapidly than in steady-state heating processes.

2.4 | The standard flare model

Solar flares are among the most energetic events on the Sun, representing sudden, violent releases of magnetic energy stored in stressed or sheared coronal magnetic field configurations (Benz, 2017). The largest solar flares can release up to 10^{33} erg of energy over timescales ranging from minutes to hours, with the energy appearing across the electromagnetic spectrum from radio waves through gamma rays. The most energetic flares are often accompanied by coronal mass ejections (CMEs)—large-scale eruptions of plasma and magnetic field into interplanetary space—that can drive space weather events affecting Earth's magnetosphere and technological infrastructure (Yashiro et al., 2005).

Solar flares are classified according to their peak X-ray flux in the 1–8 Å wavelength band as measured by the GOES satellites (Garcia, 1994). The classification uses a logarithmic scale: C-class flares have peak flux of 10^{-6} to 10^{-5} W m^{-2}, M-class flares range from 10^{-5} to 10^{-4} W m^{-2}, and X-class flares exceed 10^{-4} W m^{-2}. Within each class, a numerical multiplier indicates the strength (e.g., an M5 flare is five times stronger than an M1). The most powerful flares observed on the Sun include the Carrington Event of 1–2 September 1859 (Carrington, 1859), estimated to be equivalent to an X40+ flare (Cliver and Svalgaard, 2004), X20-class events observed in 1989 and 2001, and the November 4, 2003 flare initially measured as X28 but later upgraded to approximately X45 based on ionospheric effects (Thomson et al., 2004)—saturating the GOES detectors and representing the strongest directly measured solar flare on record. Understanding flare physics is crucial not only for predicting space weather impacts but also for interpreting stellar flare observations, where similar—but often far more energetic—events occur on active stars.

The standard flare model, illustrated in Fig. 2.3, describes the sequence of physical processes during a solar flare. The process begins with magnetic reconnection at the loop top, where oppositely directed magnetic field lines break and reconnect, converting stored magnetic energy into kinetic energy, thermal energy, and energetic particle acceleration. This reconnection accelerates electrons to high energies (tens to hundreds of keV), which then spiral down magnetic field lines toward the loop footpoints guided by the magnetic geometry.

These accelerated electrons bombard the dense chromosphere at the footpoints, depositing their energy through collisions with ambient plasma. This impulsive energy deposition heats the chromospheric material explosively, producing hard X-ray bremsstrahlung emission and intense optical continuum emission (white-light flares) at the footpoints. The heated chromospheric plasma rapidly expands and evaporates upward into the coronal loop along the magnetic field lines, filling the loop with hot, dense plasma. This evaporated plasma collects at the loop top where it cools more slowly through radiation and thermal conduction, producing the bright soft X-ray emission characteristic of the flare's gradual phase. Flares emit across the electromagnetic spectrum—from radio through gamma rays—with different wavelengths tracing different physical processes and regions of the flare structure. The contrast between impulsive emission (including hard X-rays, white-light, and optical continuum) from footpoints and gradual soft X-ray emission from the loop top reflects the different physical processes and timescales at work.

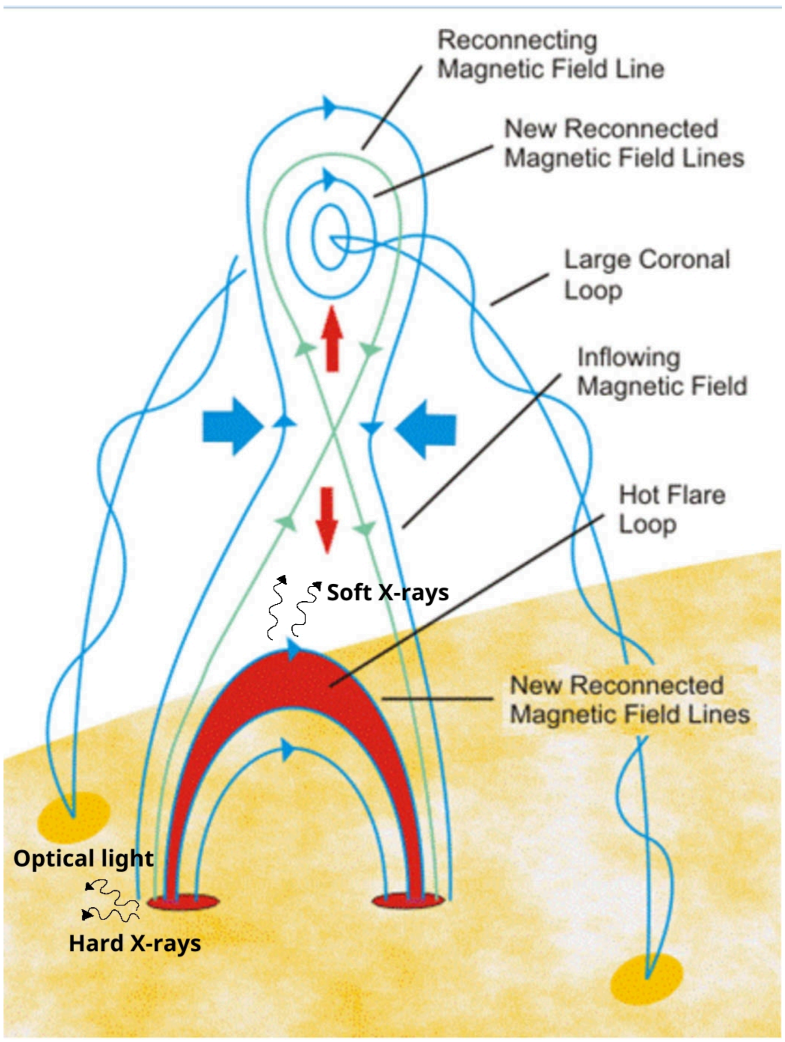

Figure 2.3: Standard solar flare model showing different evolutionary stages and associated emission signatures. Magnetic reconnection at the loop top accelerates electrons that bombard the chromosphere at footpoints, driving chromospheric evaporation and producing hard X-ray and optical emission at the footpoints and soft X-ray emission from hot plasma at the loop top. The diagram illustrates the multiple emission mechanisms occurring simultaneously during different flare phases, though this work focuses on the soft X-ray emission from the hot loop-top plasma. Image credit: NASA (`https://www.nasa.gov/image-article/reconnection-sun/`), adapted by the author

This process explains the Neupert effect [citation needed: Neupert effect], which describes the temporal relationship between footpoint emissions (hard X-rays, optical continuum) during the impulsive phase and soft X-ray emission from the loop top during the gradual phase. The hard X-ray flux derivative approximately traces the rate of energy input to the chromosphere, while the soft X-ray emission reflects the accumulated thermal energy in the coronal loop. Thus, the soft X-ray light curve appears as the time-integrated version of the hard X-ray light curve, reflecting the fact that chromospheric evaporation driven by energetic electron bombardment builds up the hot coronal plasma observed in soft X-rays.

2.4.1 | Post-flare arcades and sympathetic flaring

Following major flares, particularly those associated with coronal mass ejections, long-lived systems of bright coronal loops often form, known as post-flare arcades (Sheeley et al., 1975; Tripathi et al., 2004) (Fig. 2.4). These arcade structures consist of multiple hot loops arranged in an arch-like configuration, appearing as extended bright features in soft X-ray and EUV observations. Post-flare arcades form as the coronal magnetic field relaxes and reconnects following the disruption caused by the primary flare and CME, gradually building up a system of newly-closed field lines that trap hot plasma. These structures can persist for hours to days after the initial trigger event, slowly cooling as they radiate energy (McKenzie, 2000).

Extremely energetic flares can also trigger sympathetic or "arcade" flaring—a cascade of secondary flares in surrounding active regions (Biesecker et al., 1994; Moon et al., 2003). The primary flare releases enormous energy via magnetic reconnection, disrupting the large-scale coronal magnetic field structure. This disturbance propagates outward as pressure waves, shock fronts, and magnetic perturbations, triggering neighboring active regions with stressed or near-critical magnetic field configurations into reconnection. The result is a series of secondary flares that may form an extended pattern of brightenings across the stellar surface, appearing minutes to hours after the primary event (Schrijver and Title, 2011). While these secondary flares are typically weaker than the pri-

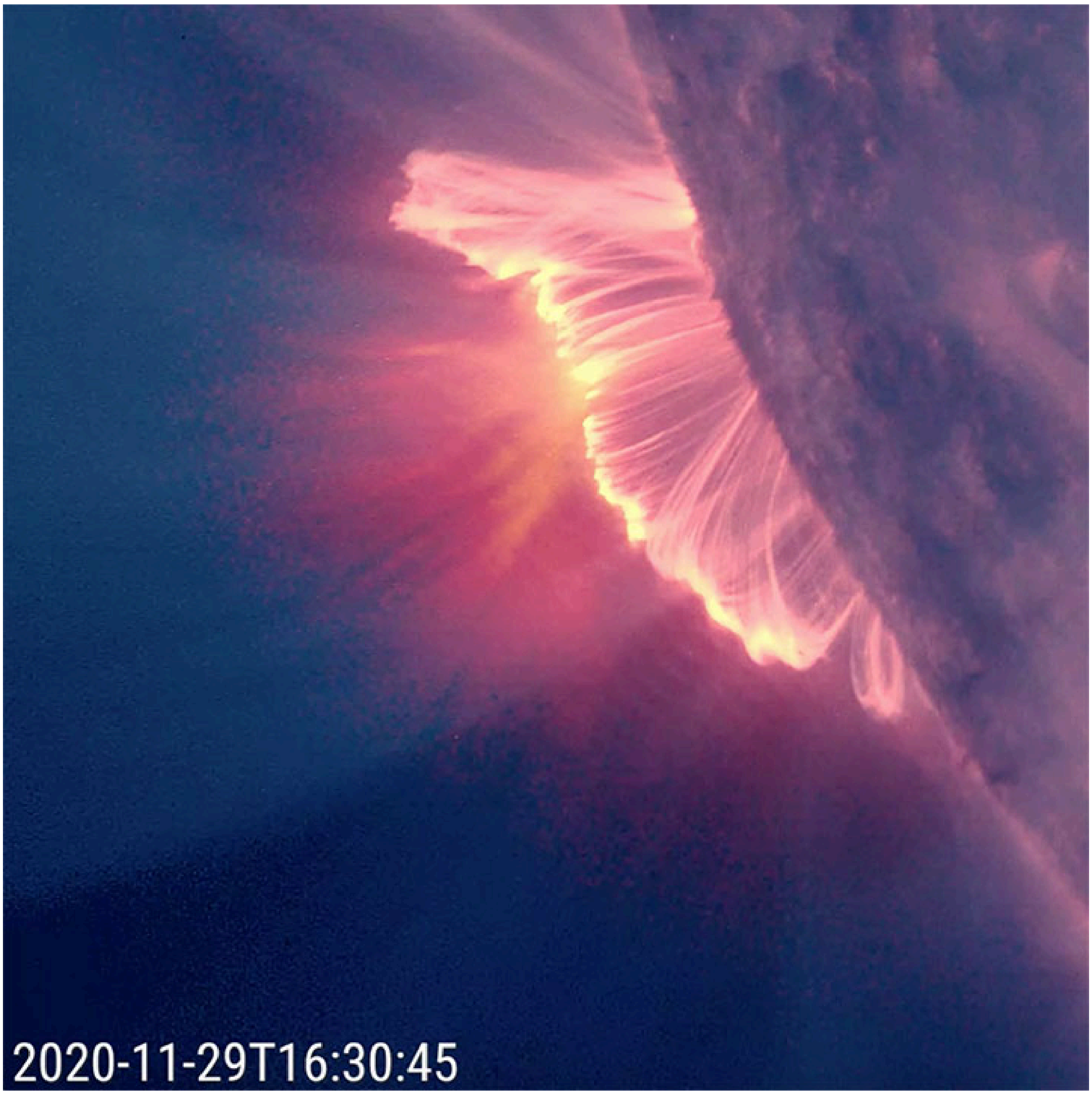

Figure 2.4: An arcade flare observed by the Atmospheric Imaging Assembly (AIA) aboard NASA's Solar Dynamics Observatory (SDO) on 29 November 2020. Credit: NASA/SDO.

mary trigger, their combined contribution can significantly enhance the total coronal emission following major flare events.

On the Sun, sympathetic flaring has been observed and documented extensively, particularly during periods of high solar activity when multiple active regions are present simultaneously (Moon et al., 2003). For unresolved stellar observations, distinguishing between a single large flare and multiple sympathetic flares is challenging, as the integrated X-ray emission simply shows elevated flux. The temporal signature may show complex structure with multiple peaks or extended decay phases if sympathetic flares occur in sequence, but unambiguous identification requires spatially resolved observations that are currently unavailable for stars.

2.4.2 | Flare signatures in observations of unresolved stars

Flares produce distinctive temporal signatures in X-ray light curves, characterized by rapid rises in count rate followed by more gradual exponential or linear decays (see Fig. 5.3). The flare evolution typically consists of several phases: a fast rise to peak as magnetic energy is rapidly released through reconnection, a plateau or peak phase where emission remains elevated, and decay phases (initially exponential, sometimes transitioning to linear) as the heated plasma cools through radiation and conduction.

On active stars, particularly M dwarfs, high count rates or sudden jumps in X-ray light curves are typically attributed to flaring activity. The baseline count rate represents quiescent coronal emission, while flare events appear as distinct excursions above this baseline. On highly active stars, distinguishing true quiescence from overlapping low-level flare activity can be challenging, as the corona may host continuous small-scale reconnection events that elevate the apparent baseline. The amplitude and duration of flare signatures scale with the energy released, with stellar superflares producing count rate increases that can exceed quiescent levels by orders of magnitude and persist for hours to days.

In addition to temporal signatures in light curves, flares dramatically affect X-ray spectra: they contribute substantial high-energy flux and increase the overall count rate, particularly at energies above a ≈ 2 keV where thermal emission from multi-million Kelvin plasma dominates.

2.5 | The stellar dynamo: origin of magnetic fields

To understand how magnetic structures in stellar coronae form and evolve, I must first examine the dynamo processes that generate magnetic fields in the stellar interior. Magnetic field generation in stars with exterior convective envelopes occurs through dynamo processes operating at the interface between these zones (Charbonneau, 2014).

Two primary processes operate in concert in the α–Ω dynamo to generate and sustain magnetic fields in stars with convective envelopes. Magnetic fields are produced by electric currents in the highly conducting plasma. The Ω-effect arises from differential rotation, both in latitude and in radius ($\partial\Omega/\partial r$), with strong shear at the base of the convection zone (the tachocline). This shear stretches pre-existing poloidal field lines into toroidal (azimuthal) configurations. The α-effect is driven by helical convection: Coriolis forces impart systematic twist to rising and sinking convective motions, allowing toroidal fields to be converted back into poloidal fields and thereby closing the dynamo cycle.

The interplay between these α- and Ω-effects constitutes the $\alpha\Omega$ dynamo mechanism, illustrated in Fig. 2.5. This dynamo cycle produces periodic reversals of magnetic field polarity, which manifest as stellar activity cycles such as the Sun's well-known 11-year cycle and analogous cycles observed in other stars.

In the convection zone, strong heat gradients drive vigorous convective currents, and the motion of plasma within this zone amplifies and transports magnetic fields generated by the dynamo. Deep in the stellar interior, conditions favor a high plasma-β regime where plasma pressure dominates over magnetic pressure, causing magnetic field lines to follow plasma motion. These convective currents drag magnetic field lines from the interior toward the surface. At

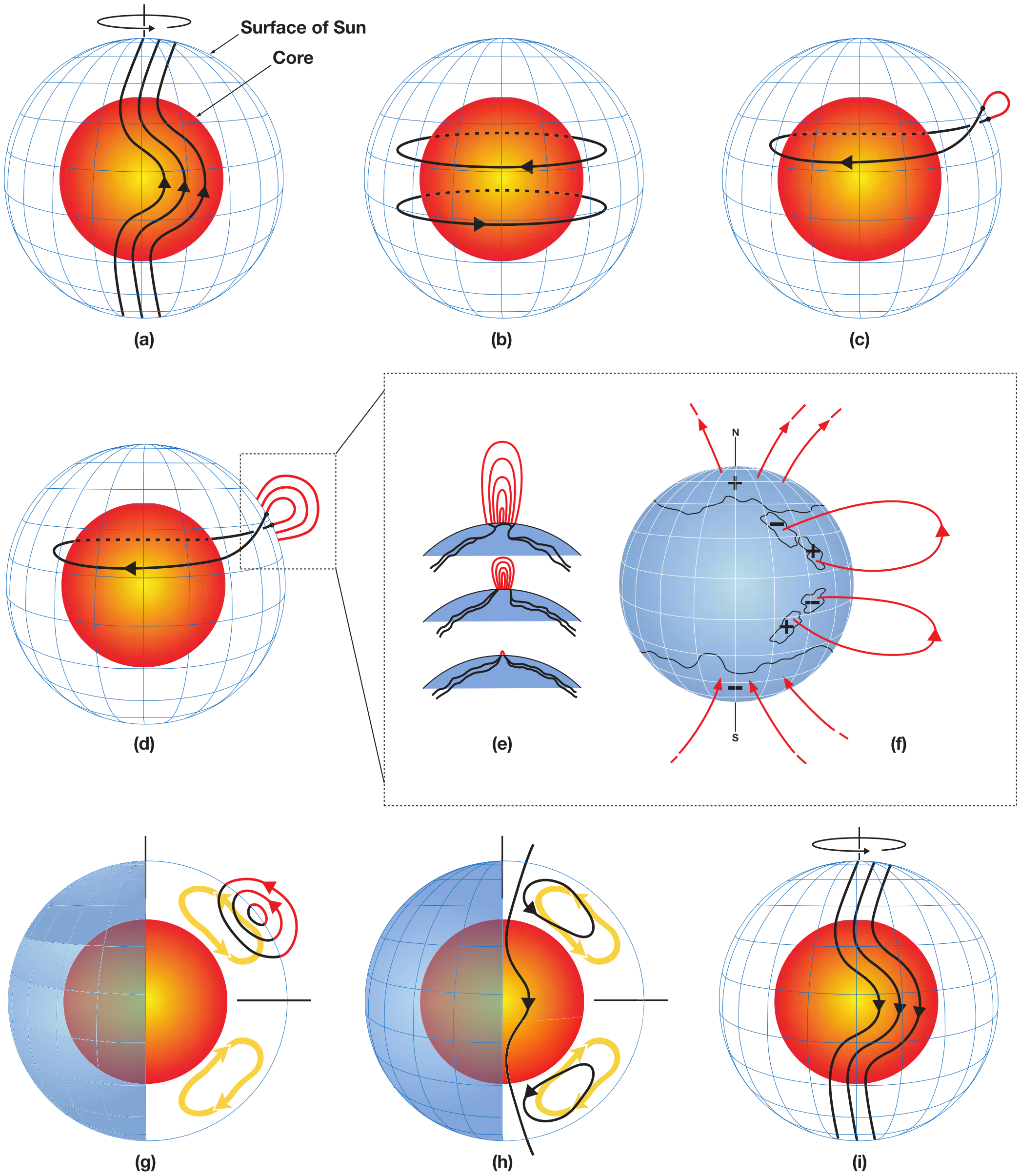

Figure 2.5: Babcock dynamo model illustrating how magnetic field lines are generated in the solar interior and emerge on the surface as coronal loops (Dikpati and Gilman, 2008). Reproduced with permission from Springer Nature.

the photosphere, magnetic field lines emerge as loops anchored at footpoints, marking a transition to the low plasma-β regime of the corona where magnetic pressure dominates and magnetic fields structure the coronal plasma into the loops, arcs, and active regions I observe.

2.6 | M dwarfs and stellar activity

M dwarfs with masses $\leq 0.35 M_{\odot}$ lack radiative cores and are instead fully convective throughout their interiors (Chabrier et al., 2000). This means efficient convection operates throughout the entire star with no clear interface between radiative and convective zones. The enhanced magnetic activity observed in M dwarfs is attributed to this efficient convection, which drives stronger and more pervasive dynamo action.

Multiple lines of evidence point to high activity levels in M dwarfs (Güdel et al., 2004; Hawley et al., 2014; West et al., 2008). They exhibit high X-ray luminosities relative to their bolometric luminosity, frequent and energetic flaring activity, strong chromospheric emission (visible in Hα and Ca II H & K lines), and persistent coronal heating evidenced by sustained X-ray emission.

The space weather implications of this intense activity are particularly relevant for exoplanet habitability. Coronal mass ejections (CMEs), which are large-scale eruptions of plasma and magnetic field from the corona into interplanetary space, often accompany major flares and release stored magnetic energy. On the Sun, CMEs can carry 10^{15} to 10^{16} g of plasma at velocities ranging from hundreds to thousands of kilometers per second (Vourlidas et al., 2010).

On Earth, the magnetosphere provides partial protection from direct radiation damage. Nevertheless, CMEs trigger geomagnetic storms that produce aurorae at high latitudes, and strong CMEs can disrupt satellite operations, GPS systems, and power grids. Telecommunication infrastructure is particularly vulnerable during severe space weather events.

For exoplanets orbiting active M dwarfs, the situation is potentially more dire. Stellar flares on these stars may be accompanied by proportionally more energetic CMEs. Repeated CME impacts on exoplanets can lead to atmospheric erosion over time. Additionally, high-energy radiation from flares, including X-rays and extreme ultraviolet photons, dissociates atmospheric constituents such as H_2O and CO_2. The combined effects of radiation and particle bombardment threaten long-term atmospheric stability. Planets in M dwarf habitable zones are particularly vulnerable because the close orbital distances required by low stellar luminosity place them in high-radiation, high-particle-flux environments.

Understanding M dwarf magnetic activity is therefore critical for evaluating the habitability of discovered exoplanets. The frequency and energy of flares, strength of CMEs, and sustained high-energy radiation all factor into habitability models.

2.6.1 | AD Leo

AD Leo (GJ 388, spectral type M3.5V) is a nearby (d $\approx$ 4.9 pc) M dwarf exhibiting high coronal activity (Favata et al., 2000; Hawley and Pettersen, 1991). It has been extensively studied as a prototypical active M dwarf (Hawley and Pettersen, 1991; Saar and Linsky, 1985; Stelzer et al., 2022), with well-characterized flaring behavior and coronal properties from optical, UV, and X-ray campaigns. Known for frequent and powerful flares—including superflares orders of magnitude more energetic than the largest solar events—it provides an ideal test case for determining whether solar-derived SaXS models can extend to stellar coronae with fundamentally higher activity levels and potentially super-solar temperatures. The star's proximity, brightness, and extreme activity make it both observationally accessible and scientifically interesting for understanding magnetic activity at the high-activity end of the M dwarf population.

2.7 | Emission Measure Distributions (EMDs)

Understanding coronal thermal structure requires quantifying how much emitting plasma exists at each temperature. The emission measure (EM) represents the integral of squared electron density along the line of sight: EM = $\int n_e^2 dV$, typically expressed in units of cm^{-3}. For spatially extended sources like the solar corona, I often work with emission measure per unit projected area, measured in cm^{-5}. An emission measure distribution (EMD) describes how this quantity varies with temperature, essentially providing a temperature census of the plasma—revealing whether the corona is dominated by cool, warm, or hot plasma, and how that plasma is distributed across temperature space.

The foundational EMDs for this work come from *Yohkoh*/SXT observations analyzed in landmark studies by Orlando et al. (2001, 2004); Reale et al. (2001). The methodology followed a systematic two-step process: first, *Yohkoh*/SXT images were used to identify and classify different coronal regions based on their X-ray intensity and morphology (quiet background, active regions, cores, flares). Then, for each classified region type, spectral information from multiple filters was used to derive the characteristic EMD—the distribution of emission measure as a function of temperature—for that region type.

These studies produced EMDs per unit projected area for distinct coronal region types. Orlando et al. (2001) analyzed 23 synoptic images containing various region types (BKC, AR, CO) (Fig. 2.6), while Orlando et al. (2004) followed a single active region through 78 observations spanning its evolution. Reale et al. (2001) derived EMDs for eight flares of different GOES classes (C5.8, M1.0, M1.1, M2.8, M4.2, M7.6, X1.5, X9.0), covering different phases from rise to peak and decay, as shown in Fig. 2.7.

The resulting EMDs exhibit distinct characteristic shapes that reflect the physical conditions in each region type. Background corona EMDs peak at relatively low temperatures (around 1–2 MK) with modest emission measures. Active region EMDs shift to higher temperatures (2–4 MK) and show substantially greater emission measures, reflecting hotter and denser loop populations. Cores—the hottest regions within active regions—peak at even higher temperatures (4–8 MK) with the highest emission measures. Flare EMDs extend to the highest temperatures (tens of MK), with emission strongly weighted toward hot plasma created during impulsive heating. This progression from BKC $\rightarrow$ AR $\rightarrow$ CO $\rightarrow$ FL represents increasingly energetic magnetic structures with progressively hotter and more emissive plasma.

For flares, Reale et al. (2001) derived EMDs for multiple snapshots of each flare, capturing temporal evolution (Fig. 2.8). For practical applications in this

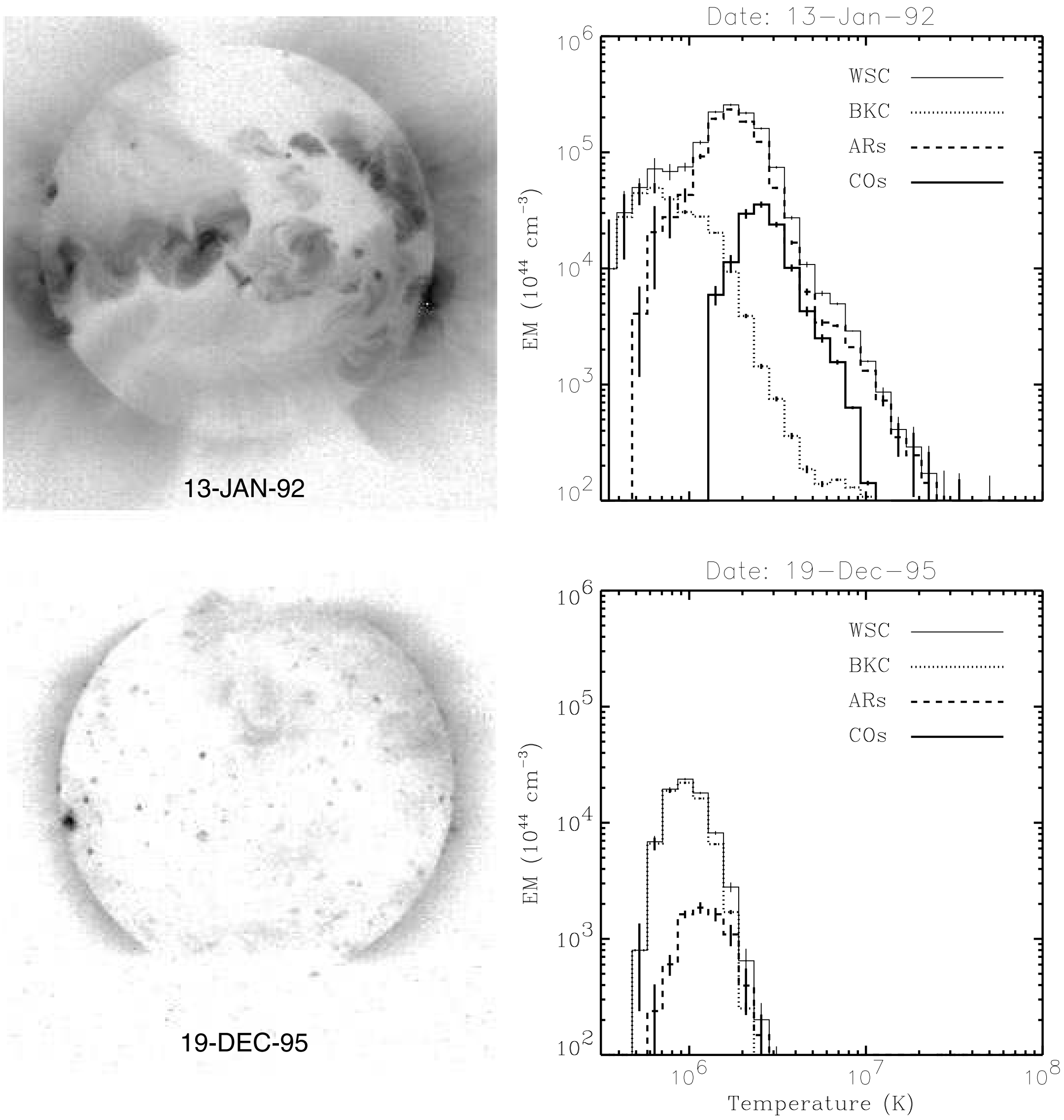

Figure 2.6: EMDs per unit projected area for distinct solar coronal region types, reproduced from Orlando et al. (2001). Left panels show full-disk *Yohkoh*/SXT images, and right panels show the corresponding EMDs as a function of temperature for background corona (dotted line), active regions (dashed line), and cores of active regions (solid line). Results are shown for solar maximum (1992 January, top) and solar minimum (1995 December, bottom), illustrating how the relative contributions of each region type vary across the activity cycle. These EMDs form the thermal templates used in the SaXS spectral models developed in this work.

work, time-averaged flare EMDs can be constructed by averaging EMDs from all snapshots of each flare.

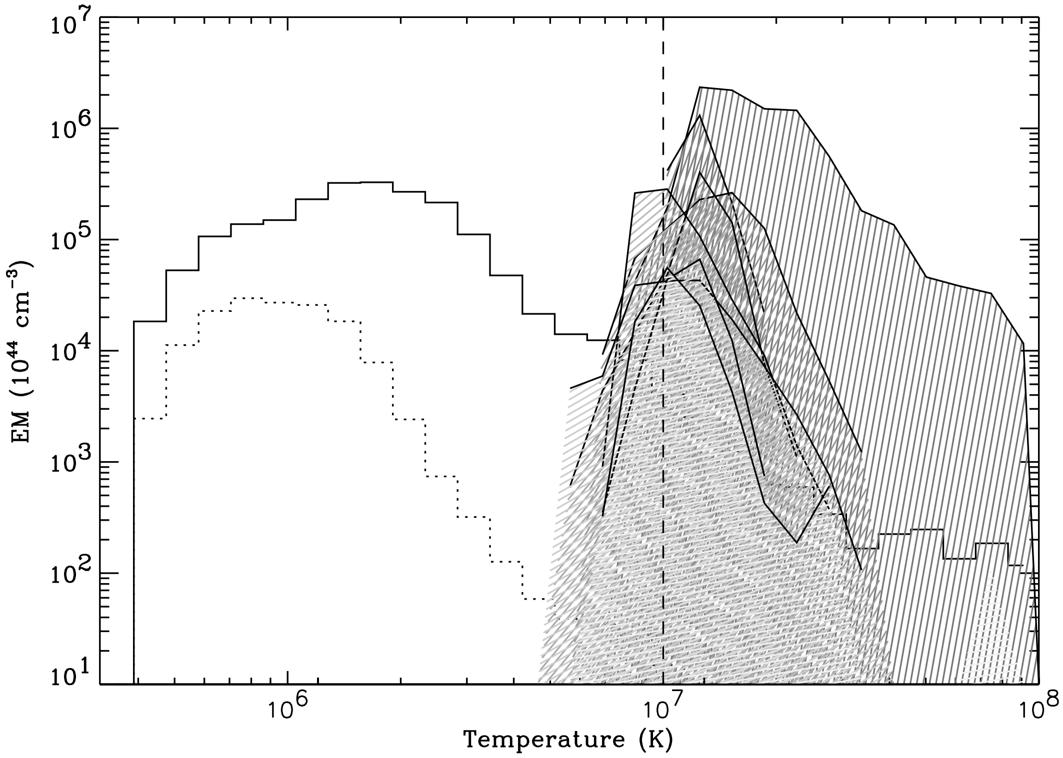

Figure 2.7: EMDs for 8 solar flares of different GOES classes (C5.8 to X9.0) from Reale et al. (2001), shown as variously shaded regions. For reference, full-Sun EMDs at solar maximum (solid histogram) and minimum (dashed histogram) from Peres et al. (2000) are overlaid. Each flare EMD represents time-averaged thermal structure across all evolutionary phases, providing templates for different flare energy classes in the SaXS method.

The basic assumption underlying these distributions is that each temperature bin in an EMD can be approximated as isothermal plasma. The multi-temperature structure emerges from summing contributions across temperature bins.

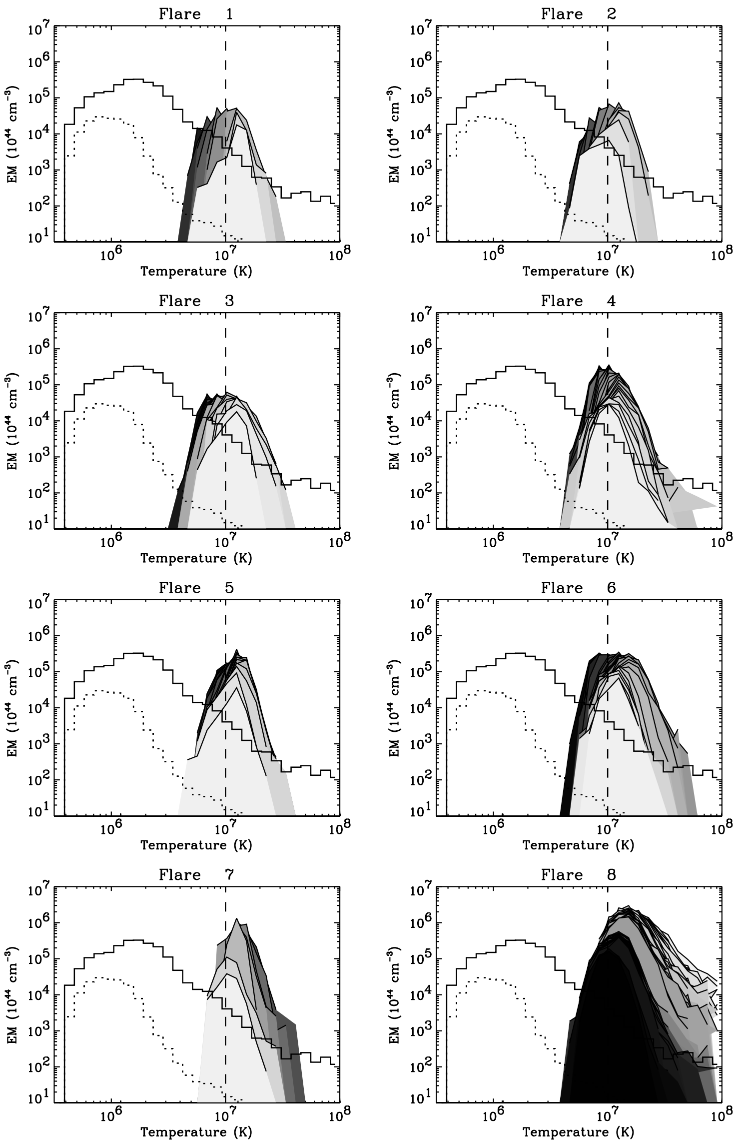

Figure 2.8: Temporal evolution of EMDs for eight selected flares, reproduced from Reale et al. (2001). EMDs are sampled approximately every two minutes from the start of each event, with the time sequence progressing from lighter to darker gray shading. For reference, full-Sun EMDs at solar maximum (solid histogram) and minimum (dashed histogram) from Peres et al. (2000) are overlaid on each panel. The vertical dashed line marks 10^7 K. The systematic evolution from hot, peaked distributions during the impulsive phase toward cooler profiles during decay motivates the use of time-averaged flare EMDs as thermal templates in the SaXS framework developed in this work.

2.8 | Traditional approaches to X-ray spectral modeling

The XSPEC model APEC (Astrophysical Plasma Emission Code) and related thermal plasma models serve as standard tools for fitting optically thin, collisionally ionized plasma in stellar coronae (Smith et al., 2001). APEC calculates emission spectra from hot, diffuse gas in collisional ionization equilibrium (CIE), incorporating line emission and continuum processes across the X-ray band. The typical approach involves fitting observed X-ray spectra with one or two thermal components to derive average coronal temperatures and emission measures. These models typically assume solar or stellar abundance patterns, with abundances either fixed or allowed to vary globally.

However, simple thermal models have important limitations. They result in a loss of information about multi-temperature structure and spatial distribution. They cannot distinguish contributions from different coronal region types, and they introduce ambiguity in the physical interpretation of fitted parameters.

2.9 | Soft X-ray instrumentation

The SaXS methodology developed in this dissertation draws on four distinct instruments, each playing a specific role. The foundational coronal region EMDs are derived from spatially resolved full-disk observations by the Soft X-ray Telescope (SXT) aboard *Yohkoh*, which provided the imaging capability needed to classify and extract EMDs for each coronal region type. The resulting spectral models are then tested against full-disk solar spectra from the Dual Aperture X-ray Solar Spectrometer (DAXSS) aboard INSPIRESat-1, which offers the spectral resolution needed to validate the models against solar soft X-ray spectra. Filling factors retrieved from these spectral fits are verified by comparison with contemporaneous spatially resolved coronal images from the X-Ray Telescope (XRT) aboard *Hinode*, providing the only available ground truth for what fraction of the solar disk each region type occupies. Finally, the validated models are applied to stellar X-ray spectra of AD Leo obtained with the European Photon Imaging Camera (EPIC/pn) aboard *XMM-Newton*, extending the SaXS framework from solar to stellar coronae. The following subsections describe each instrument in turn.

2.9.1 | *Yohkoh*/SXT (1991–2001)

The *Yohkoh* mission (Fig. 2.9) was a Japanese solar observatory launched on 30 August 1991 and operated until 14 December 2001, when the mission terminated due to spacecraft power failure. The mission aimed to study high-energy solar phenomena including flares, active regions, and coronal heating. It observed the solar corona in soft X-rays with unprecedented spatial and temporal resolution and investigated magnetic field evolution and energy release in the solar atmosphere.

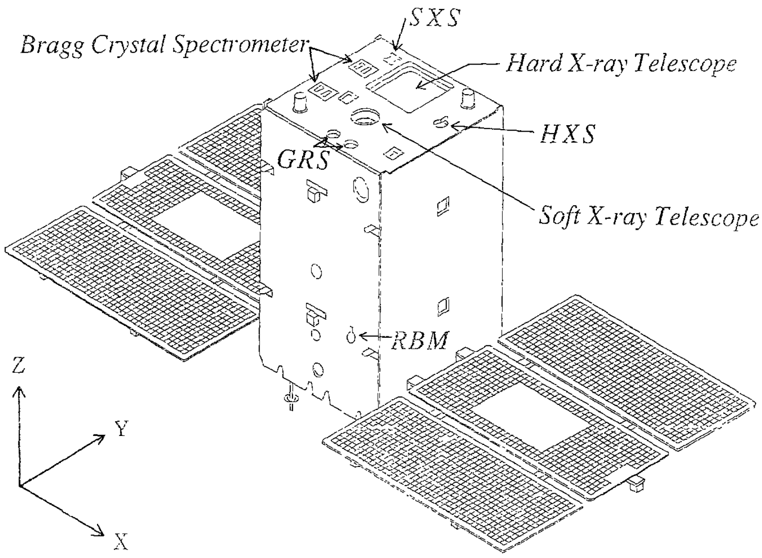

Figure 2.9: Schematic diagram of the *Yohkoh* solar observatory. The spacecraft carried four instruments including the Soft X-ray Telescope (SXT) for coronal imaging, operating from 1991 to 2001. Reproduced from Ogawara et al. (1991)

The Soft X-ray Telescope (SXT), shown in Fig. 2.10, was a grazing-incidence telescope with a CCD detector. It covered an energy range of 0.25 to 4.0 keV (approximately 3 to 50 Å) with a spatial resolution of 2.5 arcsec per pixel. The field of view was 42 × 42 arcmin in full frame mode. The cadence was typically on the order of minutes, though sub-second cadence was achievable for flare observations.

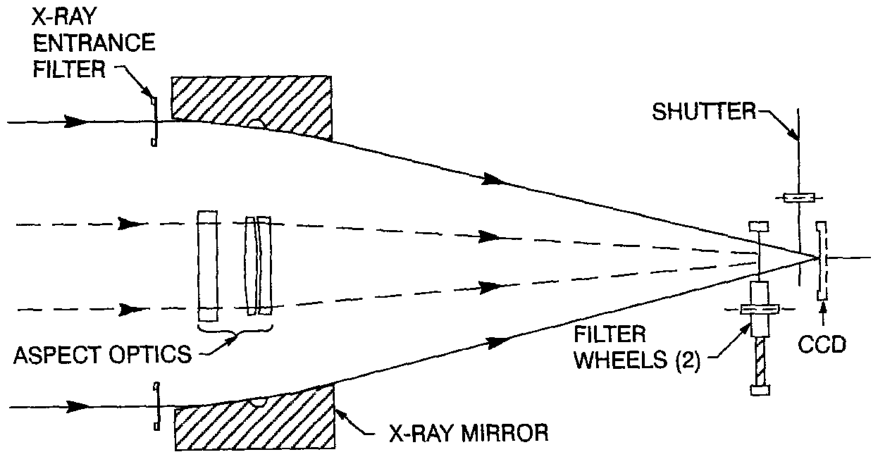

Figure 2.10: Schematic diagram of the *Yohkoh* Soft X-ray Telescope (SXT). The grazing-incidence optics with CCD detector and filter wheel system enabled temperature and emission measure diagnostics via filter-ratio methods. Reproduced from Ogawara et al. (1991)

The SXT's filter system consisted of five analysis filters plus one open position on a filter wheel. The filters included Al.1 (thin aluminum), AlMg (aluminum-magnesium), Al12 (thick aluminum), Be119 (beryllium), and Dagwood (multilayer composite). Different filter combinations enabled temperature diagnostics via the filter-ratio method, with temperature sensitivity ranging from approximately 2 to 30 MK.

Yohkoh/SXT was the first mission to provide high-cadence, high-resolution soft X-ray imaging of the full solar disk. Its filter-based imaging enabled temperature and emission measure diagnostics and established a framework for characterizing the thermal structure of different coronal region types.

The relevance of *Yohkoh*/SXT to this work cannot be overstated. It serves as the source of the EMDs used in the SaXS method. These EMDs were derived from *Yohkoh*/SXT observations by Orlando et al. (2001, 2004); Reale et al. (2001). The mission was foundational for SaXS because it established that different coronal region types (quiet Sun, active regions, coronal holes) have distinct characteristic thermal structures.

2.9.2 | *Hinode*/XRT (2006–present)

Hinode is a Japanese-led international solar mission launched on 23 September 2006, and the mission remains ongoing (Fig. 2.11). This is a joint mission involving JAXA (Japan Aerospace Exploration Agency), the National Aeronautics and Space Administration (NASA), STFC (UK Science and Technology Facilities Council), and ESA (European Space Agency).

The mission's scientific goals are to understand magnetic field generation, evolution, and dissipation in the solar atmosphere; study energy transfer from the photosphere through the chromosphere to the corona; investigate trigger mechanisms and energy release processes in flares and coronal mass ejections; and bridge spatial scales from small-scale magnetic reconnection to large-scale coronal structures. *Hinode* operates in a Sun-synchronous polar orbit at 600 km altitude with an inclination of 98°, allowing 9 months of continuous observation followed by a 3-month eclipse season.

The spacecraft carries three coordinated instruments. The Solar Optical Telescope (SOT) has a 50 cm aperture and achieves 0.2 to 0.3 arcsec resolution, providing photospheric vector magnetograms and chromospheric imaging. The EUV Imaging Spectrometer (EIS) operates in two wavelength ranges (170 to 210 Å and 250 to 290 Å) for spectroscopic plasma diagnostics. The X-Ray Telescope (XRT), which is the focus of this work, provides soft X-ray coronal imaging.

The XRT (Fig. 2.12) employs grazing-incidence Wolter-I optics with a back-illuminated CCD detector. It covers an energy range of 0.2 to 12 keV (approximately 1 to 60 Å) with a spatial resolution of 1 arcsec per pixel (2 arcsec optical resolution). The field of view is 34 $\times$ 34 arcmin in full CCD frame mode, corresponding to 2048 $\times$ 2048 pixels. The CCD detector is an E2V CCD42-40 with 13.5 μm pixel size, back-illuminated for enhanced quantum efficiency. It is passively cooled to temperatures below -43°C, with typical operating temperatures around -60°C.

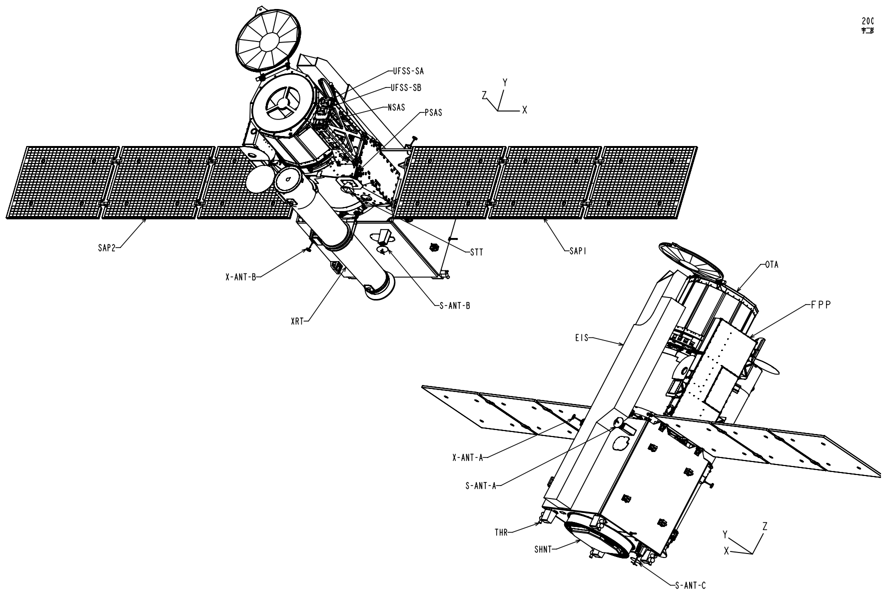

Figure 2.11: Schematic diagram of the *Hinode* solar observatory showing the three coordinated instruments: Solar Optical Telescope (SOT), EUV Imaging Spectrometer (EIS), and X-Ray Telescope (XRT). Reproduced from Kosugi et al. (2007)

The XRT's filter system (Fig. 2.13) provides nine X-ray analysis filter combinations using two filter wheels with six positions each. Filter Wheel 1 contains: Open, Al_poly, C_poly, Be_thin, Be_med, and Al_med. Filter Wheel 2 contains: Open, Al_mesh, Ti_poly, G-band, Al_thick, and Be_thick. Combining the two wheels yields filter pairs optimized for different temperature regimes. The temperature sensitivity ranges from approximately 0.5 to 30 MK, a broader range than *Yohkoh*/SXT. An additional G-band filter at 4305 Å enables visible-light imaging and coalignment with SOT.

Hinode/XRT offers several key improvements over *Yohkoh*/SXT. It provides superior spatial resolution of 2 arcsec compared to 2.5 arcsec, a larger number of filter combinations (9 analysis filters versus 5), improved CCD technology with higher quantum efficiency and lower noise, continuous operation with no interruptions from South Atlantic Anomaly passages (due to optimized orbit), and coordinated observations with simultaneous magnetic field (SOT) and spectro-

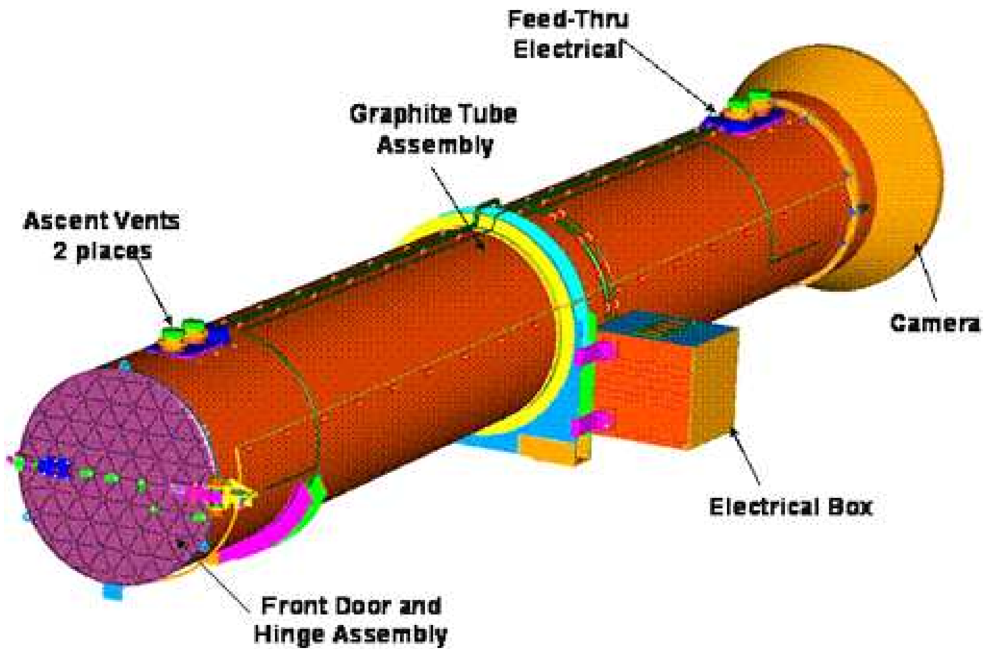

Figure 2.12: Schematic diagram of the *Hinode* X-Ray Telescope (XRT) showing its major components, with the optics located inside the entrance aperture door. Reproduced from Golub et al. (2007).

scopic (EIS) context.

The synoptic program takes full-disk observations 2 to 4 times daily when *Hinode* points at Sun center. Long and short exposure pairs are combined into high-dynamic-range composite images. Level 2 synoptic composites are fully calibrated and coaligned to heliographic coordinates (Takeda et al., 2016). The archive is available at `http://solar.physics.montana.edu/HINODE/XRT/SCIA/latest_month.html`.

For this work, Level 2 synoptic composite images are used for validation of the filling factors found using SaXS models on contemporaneous DAXSS spetcra. High-resolution full-disk observations enable direct comparison between the observed spatial distribution of coronal regions and SaXS-derived filling factors. Simultaneous imaging and spectral constraints test the consistency of SaXS decomposition. The images provide "ground truth" for validating spectral decomposition of integrated solar X-ray flux.

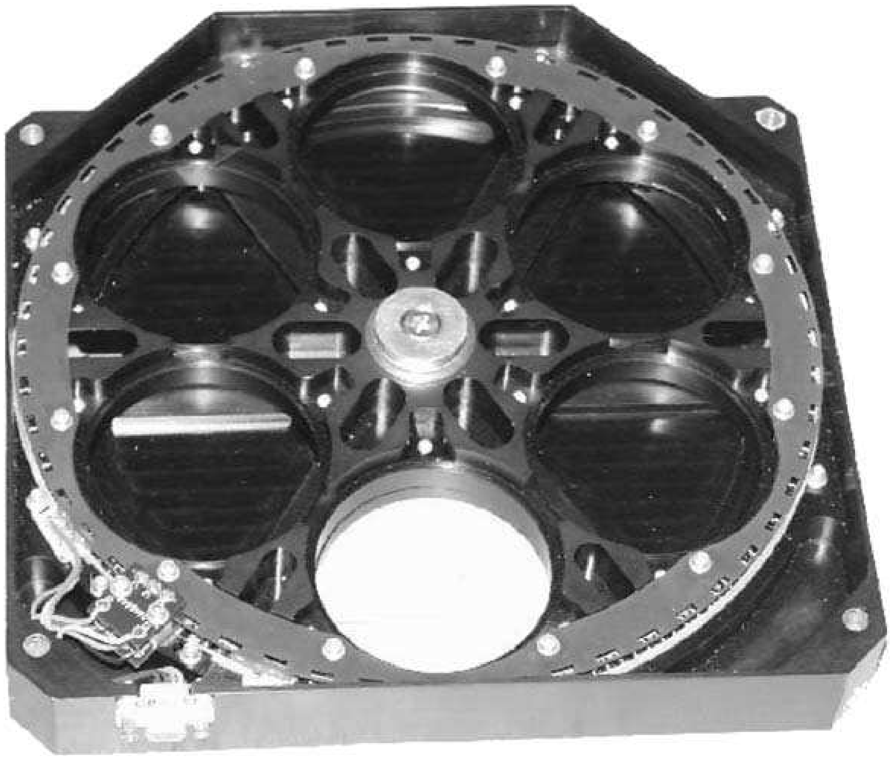

Figure 2.13: One of the two *Hinode*/XRT filter wheels, each holding five filters and one open position. Reproduced from Golub et al. (2007).

2.9.3 | DAXSS (2018–present, INSPIRESat-1)

The Dual Aperture X-ray Solar Spectrometer (DAXSS) is a NASA-funded solar soft X-ray spectrometer. It was originally flown on the International Space Station (ISS) as part of the MinXSS-2 CubeSat mission from December 2018 to May 2019. The second deployment came with the INSPIRESat-1 mission, launched on 14 February 2022, which remains ongoing. This is a collaboration between the University of Colorado Boulder, the Laboratory for Atmospheric and Space Physics (LASP), and the Indian Institute of Space Science and Technology (IIST).

DAXSS addresses a critical observational gap: historically, full-disk solar spectra in the 0.2–10 keV range comparable to those obtained for stars with *XMM-Newton* or eROSITA were unavailable. The earlier MinXSS-1 and MinXSS-2 CubeSats provided the first solar spectra in the approximately 0.5 to 10 keV band, while DAXSS (sounding rocket plus INSPIRESat-1) now delivers continuous soft X-ray solar spectra suitable for Sun-as-a-star analysis and for calibrating SaXS-type methods.

The mission goals are to provide the first continuous full-disk solar soft X-ray spectroscopy in the 0.4 to 12 keV band, enable "Sun-as-a-star" observations directly comparable to stellar X-ray spectroscopy, bridge the gap between spatially-resolved solar observations and unresolved stellar observations, study solar flares, active regions, and quiescent coronal emission via spectroscopy, and validate solar spectral models for application to stellar coronae.

The platform, INSPIRESat-1 (Fig. 2.14), is a 3U CubeSat (10 × 10 × 34 cm) operating in a Sun-synchronous low-Earth orbit at an altitude of approximately 525 km with an inclination of 97.5°. The DAXSS soft X-ray spectrometer serves as the primary payload, supplemented by secondary payloads for radiation dosimetry and technology demonstration experiments (Fig. 2.14).

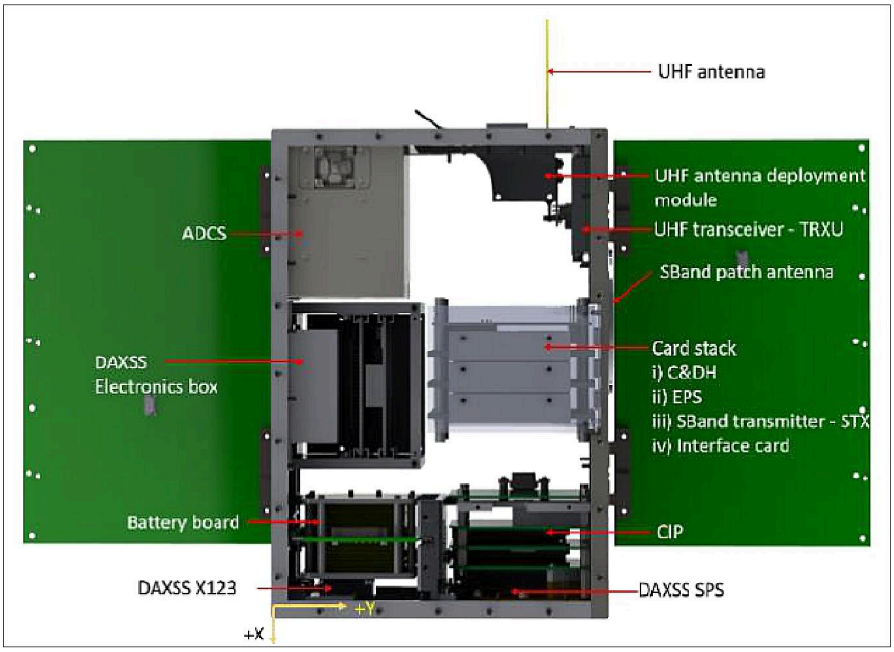

Figure 2.14: INSPIRESat-1 CubeSat with labeled components. The 3U CubeSat (10 × 10 × 34 cm) carries the DAXSS soft X-ray spectrometer as its primary payload along with secondary radiation dosimetry and technology demonstration experiments. (image credit: INSPIRESat-1 Team)

The DAXSS spectrometer (Fig. 2.15) employs a Silicon Drift Detector (SDD), specifically the Amptek X-123 model. It covers an energy range of 0.4 to 12 keV (approximately 1 to 30 Å) with an energy resolution of approximately 150 eV FWHM at 5.9 keV. The field of view is 4° FWHM, which encompasses the entire solar disk from low-Earth orbit (where the Sun subtends approximately 0.5°). Because DAXSS performs full-disk integration with no spatial resolution, it observes the Sun as a single unresolved source. The cadence offers native time resolution of a few minutes, while Level 2 data products provide 1-hour and 1-day averages.

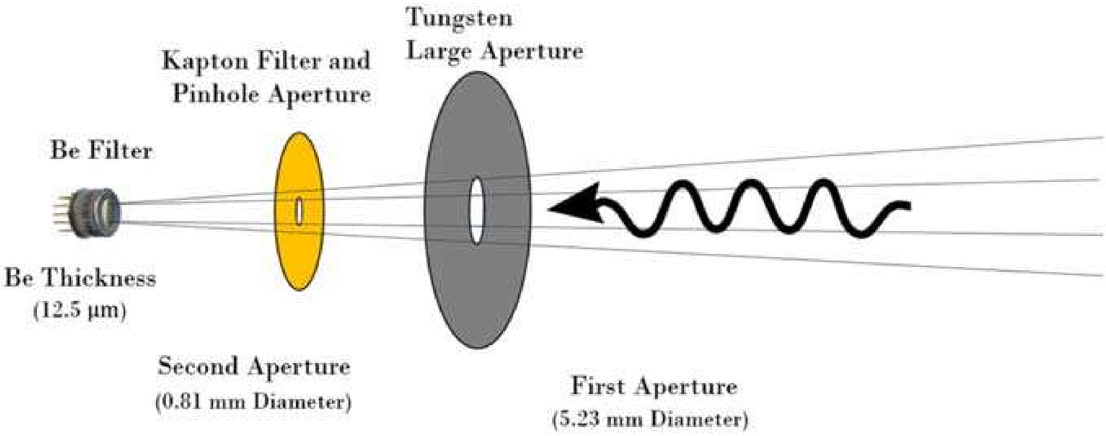

Figure 2.15: Schematic diagram of the DAXSS instrument showing the dual-aperture configuration (Schwab et al., 2020). The Silicon Drift Detector (SDD) receives X-ray photons through the aperture system, enabling full-disk solar soft X-ray spectroscopy in the 0.4–12 keV energy range.

DAXSS conducts continuous observations limited only by Earth occultations and South Atlantic Anomaly passages. As a purely spectroscopic instrument, it has no filter wheels or moving parts. The instrument directly measures photon energy, with counts binned into energy channels, eliminating the need for filter-ratio inversions. Full-disk integration provides high photon statistics, yielding strong signal even during quiet Sun conditions.

Data products are distributed in multiple levels: Level 0 consists of raw telemetry, Level 1 provides calibrated event lists with spacecraft attitude information, Level 2 offers binned spectra (energy versus counts) with 1-hour and 1-day averaged spectra, and Level 3 contains higher-level science products such as flare catalogs and spectral fit parameters. The archive is accessible at `http://lasp.colorado.edu/home/minxss/data/`.

One important limitation concerns DAXSS's low-energy response, which is not well calibrated below 0.7 keV (Schwab et al., 2020, 2023; Woods et al., 2023). The consequence is that DAXSS observations have a blind spot for cooler coronal plasma (T $\leq$ 2 MK), limiting sensitivity to quiet Sun and cool active region components. This work follows standard practice by restricting spectral fitting to the 0.7 to 7.0 keV range.

DAXSS is critical for testing the SaXS methodology on solar data. It provides broad-band spectra without spatial resolution, exactly matching stellar observation conditions. This represents the first opportunity to validate solar spectral models against integrated full-disk X-ray spectra. DAXSS enables direct comparison between solar SaXS decomposition and stellar SaXS application, serving as a bridge between spatially-resolved solar physics and unresolved stellar astrophysics.

2.9.4 | *XMM-Newton* (1999–present)

XMM-Newton is a European Space Agency (ESA) X-ray satellite launched in 1999. The mission has been extended multiple times and remains operational (Fig. 2.16). Key advantages include its highly elliptical orbit offering long continuous target visibility up to 40 hours, three co-aligned Wolter type-1 X-ray telescopes, and the capability for simultaneous multi-instrument operation.

The EPIC (European Photon Imaging Camera), shown in Fig. 2.17, comprises three CCD detectors: EPIC MOS1, EPIC MOS2, and EPIC pn. The energy range of 0.2 to 12 keV is similar to DAXSS, enabling direct method comparison. The moderate spectral resolution of $E/\Delta E \approx 20$ to 50 is sufficient for thermal plasma diagnostics. The field of view is 30 arcmin. For AD Leo observations in this work, I use EPIC pn because it offers higher sensitivity than MOS, as it receives the total incoming X-ray light.

EPIC pn offers several observation modes (Fig. 2.18). In Full Frame mode, all CCDs are read out and the entire field of view is covered. Large Window

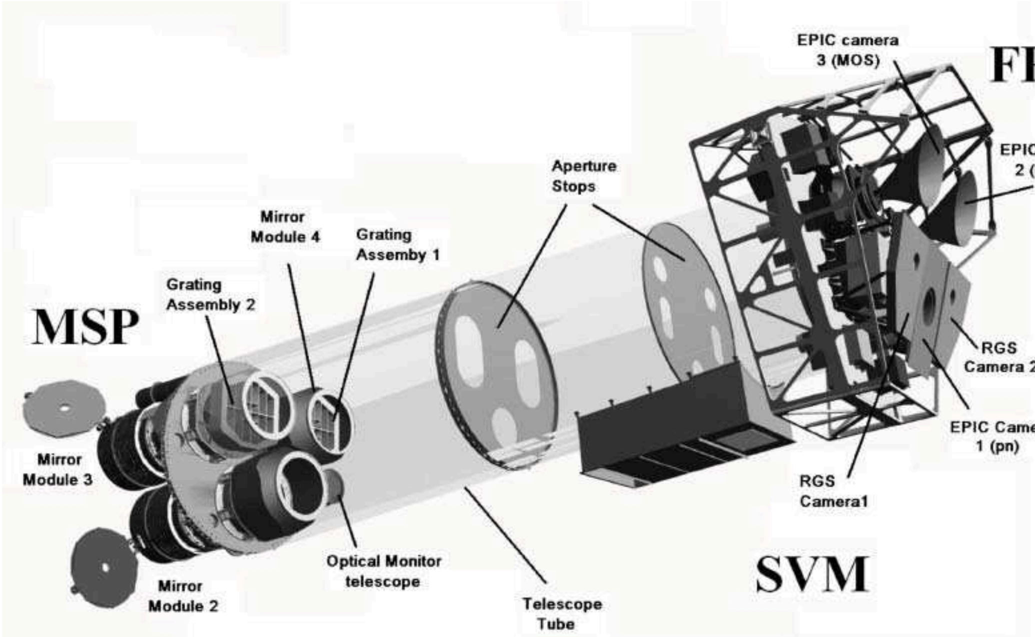

Figure 2.16: Schematic diagram of the *XMM-Newton* observatory showing the three co-aligned Wolter type-1 X-ray telescopes and instrument configuration (Lumb et al., 2012).

mode reads out half of the CCDs. Small Window mode uses part of one CCD; our AD Leo observations were taken in this mode. Each mode is associated with a different fraction of out-of-time (OoT) events—photons detected during CCD readout that are assigned incorrect detector positions, producing a streak along the readout direction in the image. For example, Small Window has 1.1% while Full Frame has 6.3%.

Background considerations are important for *XMM-Newton* observations. The cosmic X-ray background contributes at both soft energies (galactic) and hard energies (extragalactic). Soft protons (below 100 keV) are funneled by the X-ray mirrors and can affect observations depending on the satellite's position relative to Earth's magnetosphere. High-energy particles (above 100 MeV) create fluorescent lines in the background spectrum. Out-of-Time events broaden spectral features, with the fraction depending on the observation mode.

XMM-Newton is particularly suitable for stellar coronal studies. It provides high sensitivity for bright coronal sources, and its long uninterrupted observa-

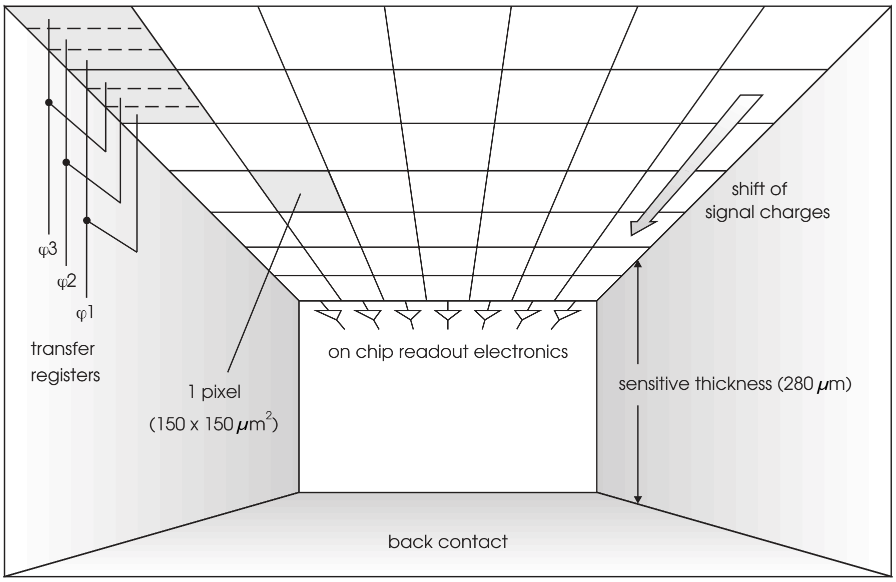

Figure 2.17: Schematic diagram of the EPIC pn detector on *XMM-Newton* (Strüder et al., 2001). The back-illuminated CCD array provides high quantum efficiency across the 0.2–12 keV energy range with moderate spectral resolution suitable for thermal plasma diagnostics.

tions enable study of flare evolution and quiescent states. The spectral capabilities are well-matched to thermal plasma emission from stellar coronae.

For this work specifically, *XMM-Newton* enables application of solar-derived SaXS models to stellar coronae. The energy range overlap with DAXSS allows direct comparison of methodology between solar and stellar applications.

2.10 | Previous SaXS implementations and stellar applications

2.10.1 | Historical development: "The Sun as an X-ray star" study

The foundational "Sun as an X-ray star" studies by Orlando et al. (2000, 2001, 2004), Peres et al. (2000), and Reale et al. (2001) established the methodology for

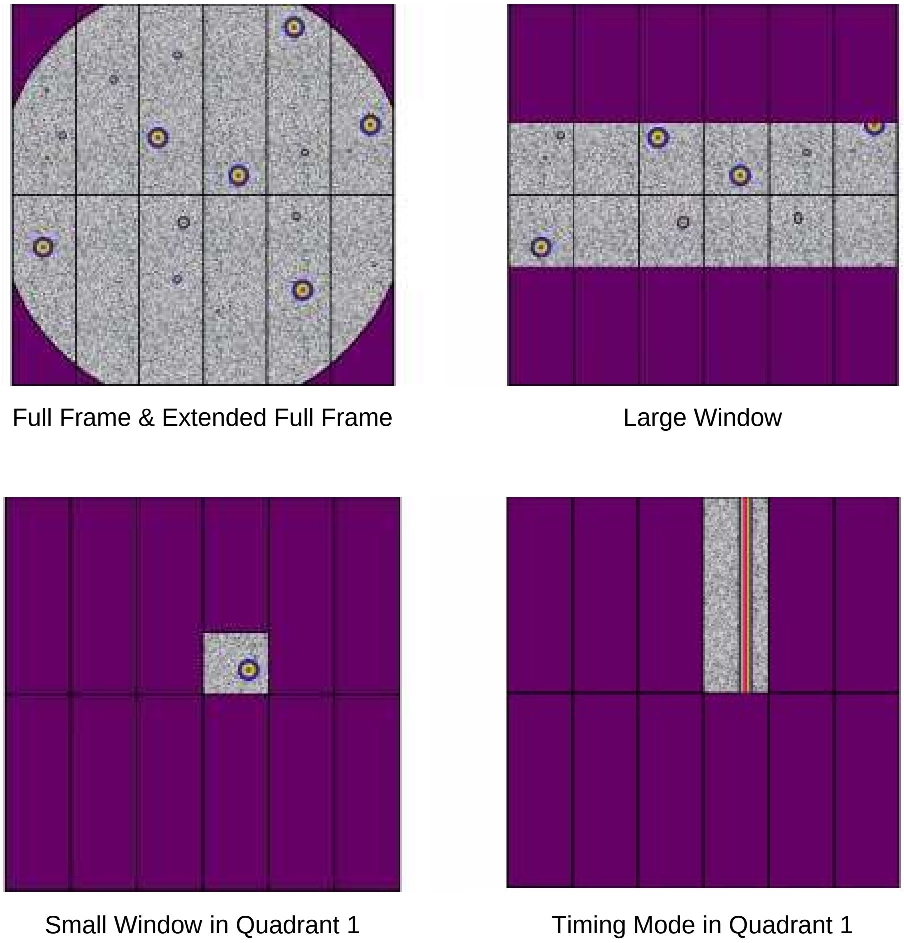

Figure 2.18: EPIC pn observation modes showing different window configurations: Full Frame, Large Window, Small Window, and Timing mode. Each mode trades field of view for reduced readout time and correspondingly lower OoT event fractions.

characterizing solar coronal structures and creating synthetic stellar spectra.

Orlando et al. (2000) derived the first full-disk solar EMD by analyzing a single *Yohkoh*/SXT full-disk image from January 1992 (solar cycle maximum). The authors retrieved an emission measure distribution representative of the whole solar corona ($\mathrm{EMD}_\odot$) by analyzing each image pixel. Their pixel filtering rejected pixels with fewer than 10 photon counts, as these tend to overestimate emission measure at temperatures below 10^6 K (Fig. 2.19). This work produced the first complete emission measure distribution of the solar corona as a function of temperature.

Peres et al. (2000) extended this analysis to multiple solar cycle phases, examining solar maximum (January 1992), intermediate activity (July 1993), and minimum (June 1994).

Their key findings from the cycle-phase EMDs showed that while the overall EMD shape remained similar across cycle phases, the peak temperature and corresponding emission measure decreased from maximum to minimum. Additionally, the high-temperature slope of the EMD was steeper during minimum.

The authors developed a procedure to generate synthetic spectra as if the Sun were observed by other X-ray satellites (ROSAT and ASCA at that time). The synthetic spectrum generation procedure works as follows. Starting with an EMD consisting of N bins, each characterized by temperature T_k and emission measure $EM(T_k)$, the authors computed the emitted spectrum for each bin using the MEKAL code (for optically thin isothermal plasma). They then summed contributions from all bins weighted by the instrumental response:

$$C_j = \frac{t}{4\pi d^2} \int_E A(E) M(j, E) \sum_k P(T_k, E) EM(T_k)\, dE,$$

where t is the exposure time, d is the distance to the star, $A(E)$ is the effective area, $M(j, E)$ is the detector response matrix, and $P(T_k, E)$ is the emitted spectrum.

To validate this approach, the authors fitted synthetic spectra (treating the Sun as if it were at 1 pc) with 1-T or 2-T isothermal MEKAL models. The best-fit parameters tracked trends of the full EMD, demonstrating consistency of

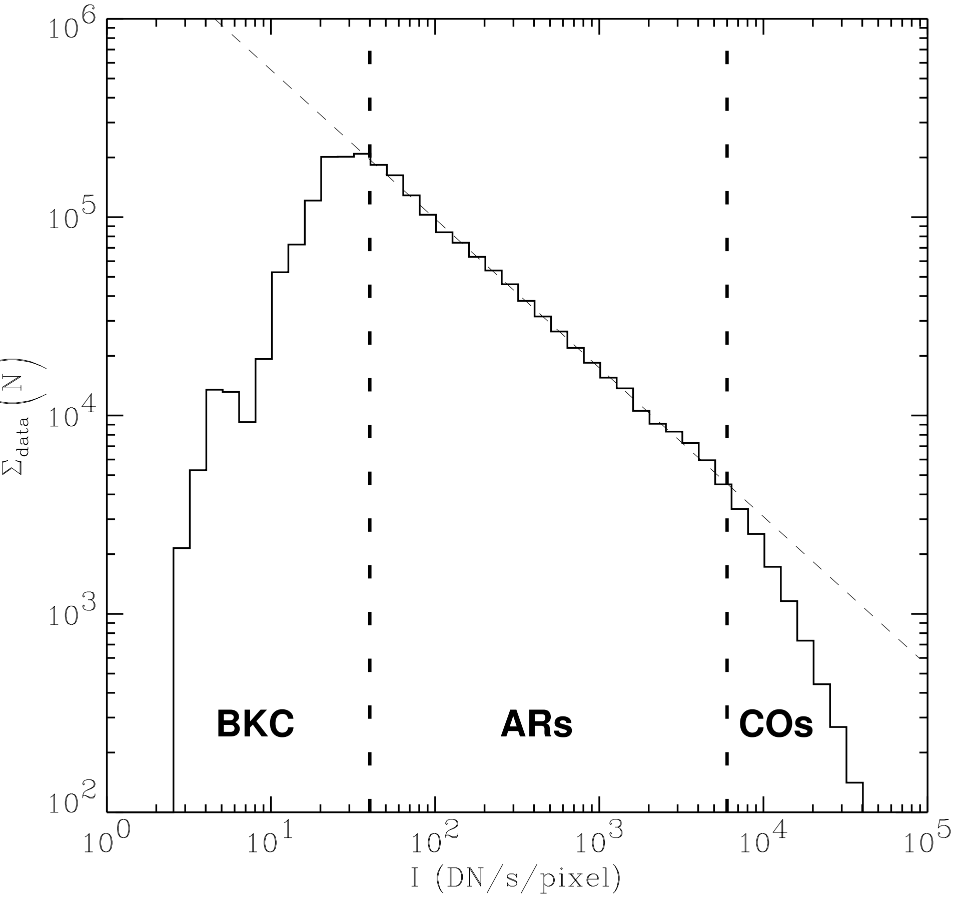

Figure 2.19: Emission measure distribution of the entire solar corona derived by Orlando et al. (2001) from *Yohkoh*/SXT full-disk image. Pixel intensities from the solar image shown in Figure. 2.20 are marked on the corresponding EMD, showing how different intensity thresholds delineate background corona, active regions, and cores. This intensity-based classification scheme forms the foundation for identifying distinct coronal region types in the SaXS method.

synthetic spectra with real observations. The purpose of this procedure was to demonstrate that fitting the multi-temperature solar EMD with simple 1-T or 2-T models (typical of stellar observations) still recovers meaningful trends, even though information is necessarily lost in the reduction from the full EMD to simple thermal models.

Reale et al. (2001) analyzed eight *Yohkoh* flares of different GOES classes (C to X). The observations used hard SXT filters sensitive to plasma at and above 10^7 K. One M-class flare was also observed with soft SXT filters, revealing the contribution from low-temperature plasma. The authors derived flare EMDs ($EMDFL_\odot$) for separate evolution phases, from rise through peak to decay. The result characterized the thermal structure of flares across energy classes and throughout temporal evolution. Note that flares were observed in a separate "flaring mode" because other structures saturate during flares.

Orlando et al. (2001, 2004) classified coronal magnetic structures by image brightness (I) in SXT images. Their intensity threshold scheme, based on histogram analysis (Fig. 2.19, Fig. 2.20), defined three categories: $I < 40$ DN s^{-1} pixel^{-1} for quiet regions or background corona (BKC), $40 \leq I < 6 \times 10^3$ DN s^{-1} pixel^{-1} for active regions (AR), and $I \geq 6 \times 10^3$ DN s^{-1} pixel^{-1} for cores of active regions (CO).

The authors applied these thresholds to all solar cycle observations to identify three classes of magnetic structures, deriving separate EMDs for each structure type: $EMDBKC_\odot$, $EMDAR_\odot$, and $EMDCO_\odot$. The total solar EMD can be described as the sum of individual contributions: $EMD_\odot = EMDBKC_\odot + EMDAR_\odot + EMDCO_\odot + EMDFL_\odot$ (Fig. 2.6).

The key result was that during solar cycle maximum, the EMD is dominated by active regions, while during minimum, it is dominated by background corona.

Orlando et al. (2004) tracked a single active region from emergence in July 1996 to disappearance in October 1996, showing the evolution of $EMDAR_\odot$ and $EMDCO_\odot$ throughout the active region's lifetime.

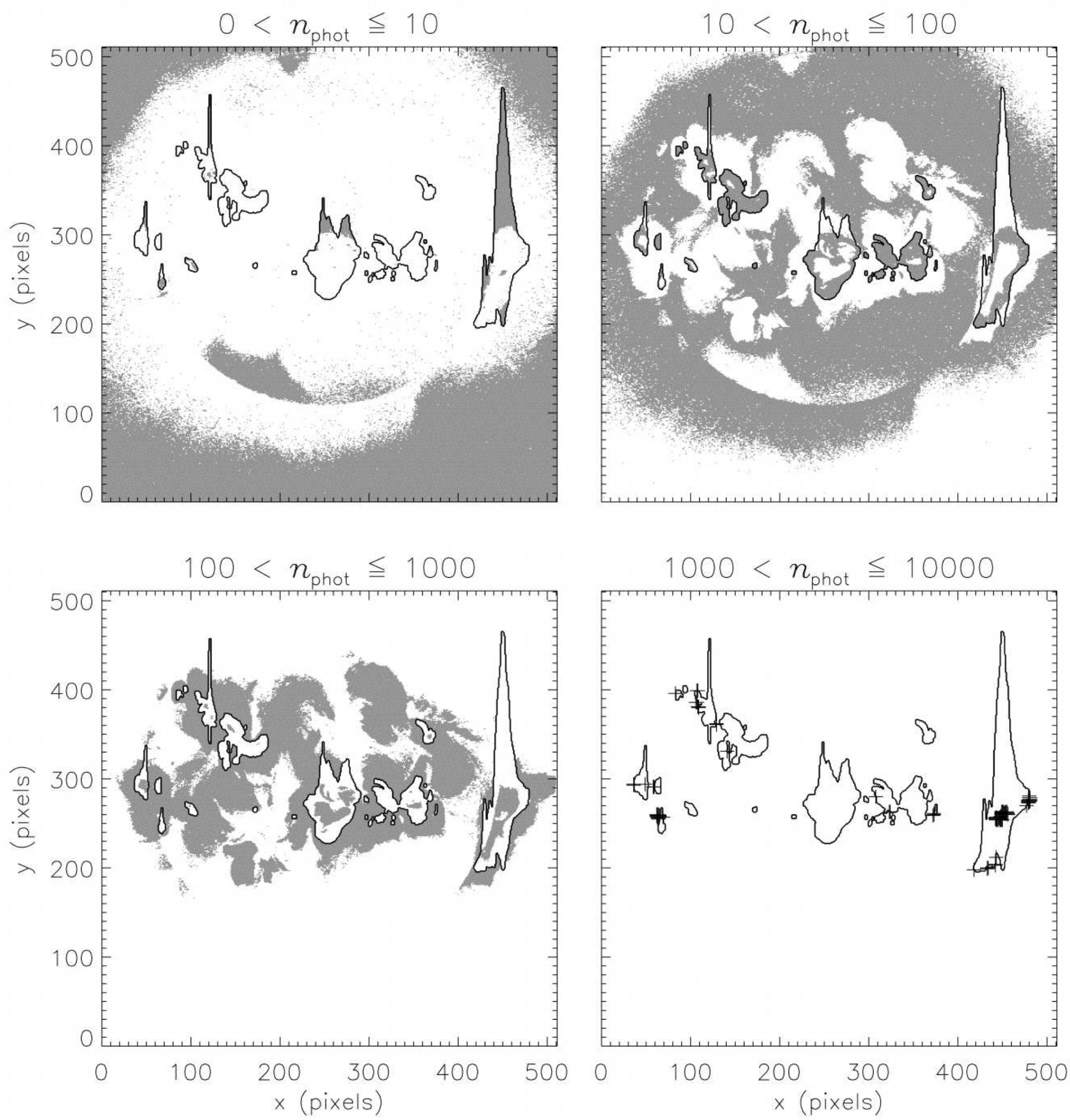

Figure 2.20: *Yohkoh*/SXT solar image demarcated by pixel intensity thresholds from Orlando et al. (2001). Four panels show different intensity cutoffs revealing background corona (lowest intensities), active regions (intermediate), and cores (highest intensities). This pixel-based segmentation enables extraction of region-specific EMDs.

2.10.2 | Key products of original SaXS methodology

The foundational "Sun as an X-ray star" study produced several key outputs. It created a grid of EMDs representative of the whole solar corona ($EMD_\odot$) at different cycle phases. It established a classification scheme for solar magnetic structures (BKC, AR, CO) based on image brightness. It derived structure-specific EMDs ($EMDBKC_\odot$, $EMDAR_\odot$, $EMDCO_\odot$) and identified dominant contributors during different solar cycle phases. It produced flare EMDs ($EMDFL_\odot$) for different flare classes and evolution phases. Finally, it developed a procedure to generate synthetic X-ray spectra representing the Sun as observed by other X-ray satellites.

The synthetic spectra approach has important applications. Synthetic spectra can be generated with characteristics of any star, not just the Sun. I can create "pseudo-solar synthetic spectra" simulating the same solar phenomena occurring on other stars. These serve as benchmarks to test whether stellar behavior is similar to the solar case.

2.10.3 | Stellar applications of original SaXS methodology

The method for stellar application proceeds as follows. The original SaXS approach uses *Yohkoh*/SXT EMDs for BKC, AR, CO and flare EMDs to build total EMDs:

$$EM_{\text{tot}} = \sum_{\text{reg}} ff_{\text{reg}}\, EMD_{\text{reg}},$$

where ff_{reg} are filling factors representing fractional surface coverage. For each combination of filling factors, an X-ray spectrum is synthesized and fit in XSPEC with isothermal APEC models to derive T_{x} and L_{x}. Synthetic $(T_{\text{x}}, L_{\text{x}})$ pairs are then compared with values derived from observed stellar X-ray spectra to infer the combination of filling factors that best matches a given star.

The method has been applied to several stars with varying success. For HD 81809, a G5 subgiant, Favata et al. (2008) and Orlando et al. (2017) synthesized the corona using combinations of AR and CO components, finding that the predicted solar-like ranges of T_X and L_X successfully bracket the observed values—suggesting a corona dominated by hot, active region-like structures. For ϵ Eri (K2V) and Kepler 63 (G0V), Coffaro et al. (2020, 2022) employed full grids of synthetic spectra spanning different combinations of filling factors for each region type. By comparing these synthetic grids to observed spectra, the authors inferred very high surface coverage by magnetic regions (approximately 60 to 90%), far exceeding typical solar values. This extreme coverage appears linked to X-ray saturation, the regime where stellar X-ray luminosity ceases to increase with rotation rate, suggesting the stellar surface becomes fully covered by active magnetic structures.

2.10.4 | Motivation for new SaXS implementation

The original implementation follows an indirect path: synthetic spectra are generated for a grid of filling factor combinations, fitted with simple thermal models to extract T_x and L_x, and then compared against actual stellar observations in parameter space to identify the best-matching combination. This approach is computationally intensive and interposes several steps between the solar EMD templates and the inferred filling factors. The method developed in this work takes a more direct route, implementing the EMD-derived templates as spectral fitting components within XSPEC so that filling factors are retrieved immediately from the model normalizations, without the need for synthetic grids or intermediate parameter-space matching.

3

Definition of XSPEC models for the SaXS method

3.1 | Overview: from EMDs to spectral models

This chapter is based on Joseph et al. (2025) (submitted), 'The Sun as an X-ray star V.: A new method to retrieve coronal filling factors,' submitted to *Astronomy and Astrophysics*. A preprint is available at arXiv:2510.23161 under a Creative Commons CC BY 4.0 license. The goal of this chapter is to convert solar EMDs observed with *Yohkoh*/SXT into empirical spectral models implemented in PyXSPEC (Gordon and Arnaud, 2021). I focus on four region types: background corona (BKC), active regions (AR), cores of active regions (CO), and flares (FL-AVG). The EMDs for these region types, described in Section 2, serve as the foundation for constructing our spectral models. These EMDs are shown in Fig. 3.1.

3.2 | Constructing the average flare EMD (FL-AVG)

Individual flare EMDs are available for eight solar flares spanning GOES classes C5.8, M1.0, M1.1, M2.8, M4.2, M7.6, X1.5, and X9.0, as shown in Fig. 3.2. For

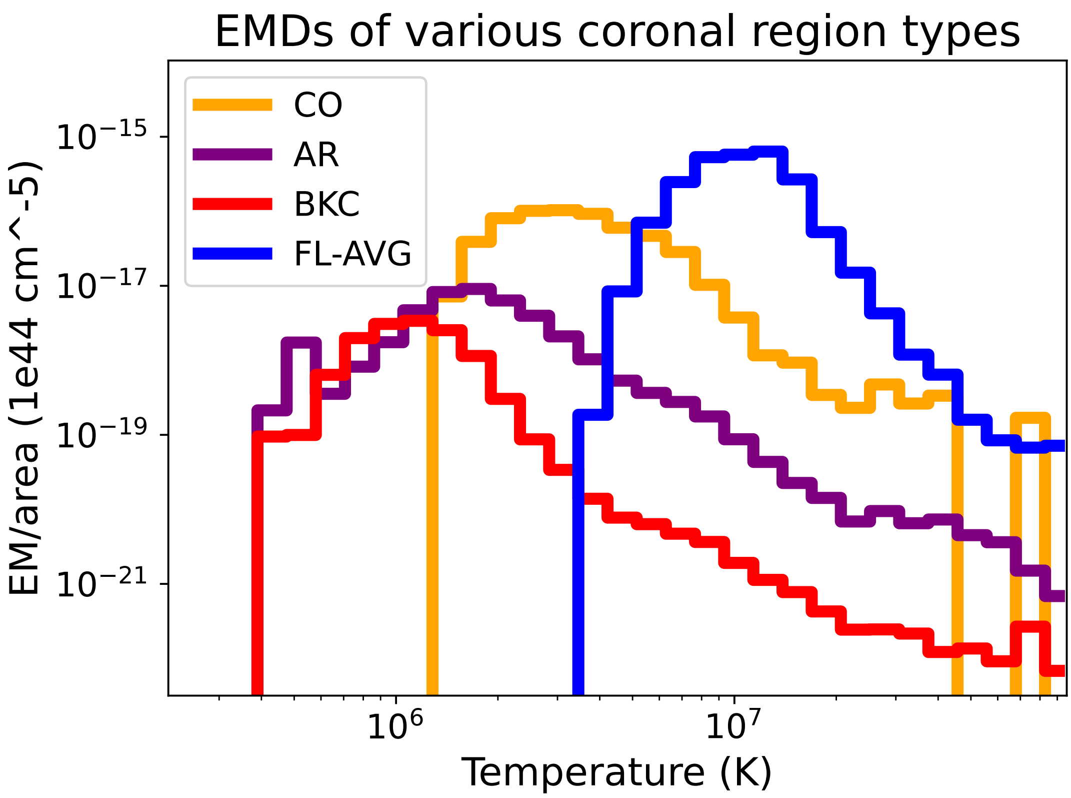

Figure 3.1: EMDs of the BKC, AR, CO and FL-AVG regions as described in Sect. 2 (Joseph et al., 2025). The y-axis shows the emission measure per unit area, in units of 10^{44} cm^{-5}. All EMDs shown here represent time-averaged distributions constructed from multiple snapshots of flares or other types of regions.

simplicity in our analysis, I combine all these flare EMDs into a single representative "average flare" EMD, which I designate FL-AVG, though models for individual flare classes (including FLX9 for the X9.0 flare) remain available for cases requiring specific flare temperatures.

The averaging scheme I employ accounts for the fact that flares with different peak amplitudes occur at different frequencies. I obtain FL-AVG as a weighted average of the individual flare EMDs, where the weights are determined by the slope of the cumulative flare energy frequency distribution (FFD)

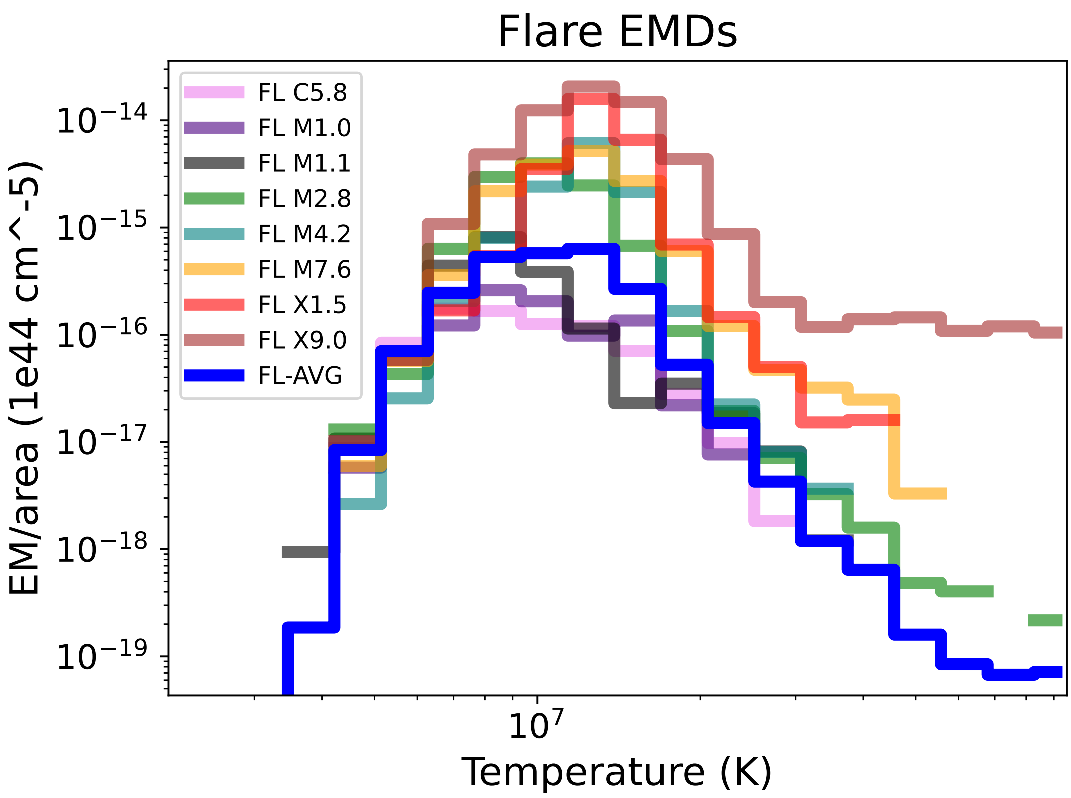

Figure 3.2: EMDs of the C5.8, M1.0, M1.1, M2.8, M4.2, M7.6, X1.5 and X9.0 flares (individual colors) along with their weighted average EMD (FL-AVG, blue) (Joseph et al., 2025). The y-axis shows the emission measure per unit area, in units of 10^{44} cm^{-5}.

in logarithmic space. This distribution follows a power law:

$$N(E) \propto E^{\alpha}, \quad \alpha = -1.54,$$

where E is the flare energy and $\alpha = -1.54$ is the FFD slope derived for solar X-ray flares from *Yohkoh* observations (Aschwanden and Parnell, 2002).

I estimate flare energies from the GOES peak flux F_{GOES} (which defines the GOES class) using an empirical relation from Namekata et al. (2017) between GOES peak flux and white-light flare (WLF) energy E_{WLF}:

$$\log(E_{\mathrm{WLF}}) = a + b \cdot \log(F_{\mathrm{GOES}}),$$

with coefficients $a = 33.67$ and $b = 0.87$ for the solar case. (White-light flares are characterized by sudden enhancement of optical continuum emission (Neidig, 1989; Song et al., 2018; Švestka, 1970).) For AD Leo, I use a modified version of this relation with updated coefficients $a = 34.71$ and $b = 1.15$ from Stelzer et al. (2022) when constructing the flare template for the stellar analysis.

The weights are normalized such that $\sum_i w_i = 1$. The resulting FL-AVG EMD, shown in blue in Figs. 3.1 and 3.2, represents a typical flare weighted by occurrence frequency and energy, incorporating all eight flares. This single flare-region EMD proves suitable for both solar validation and AD Leo stellar application.

3.3 | Converting EMDs to multi-temperature spectral models

I treat each bin i in the EMD of a given coronal region type, characterized by $(T_{\mathrm{i,reg}}, EM_{\mathrm{i,reg}})$, as representing emission from an isothermal plasma. The total EMD of that region type is then described by a distribution of several isothermal plasmas, effectively constituting a multi-temperature plasma.

In XSPEC (Arnaud et al., 1999), I construct this multi-temperature plasma model as a sum of i APEC (or VAPEC for variable abundances) components (Smith et al., 2001). Each APEC component is characterized by $(T_{\mathrm{i,reg}}, Norm_{\mathrm{i,reg}})$, plus coronal abundances as input parameters. I use PyXspec (Gordon and Arnaud, 2021) to interface with XSPEC. I assume abundances to be the same throughout the whole corona, independent of magnetic structure type.

Each coronal region model M_{reg} is defined as:

$$M_{\mathrm{reg}} = \sum_i \mathrm{APEC}(T_{\mathrm{i,reg}}, Norm_{\mathrm{i,reg}}, Abund_{\mathrm{star}}), \tag{3.1}$$

where M_{reg} can be M_{BKC}, M_{AR}, M_{CO}, or $M_{\mathrm{FL-AVG}}$. The spectral models for all four region types and their individual APEC components are visualized in Fig. 3.3.

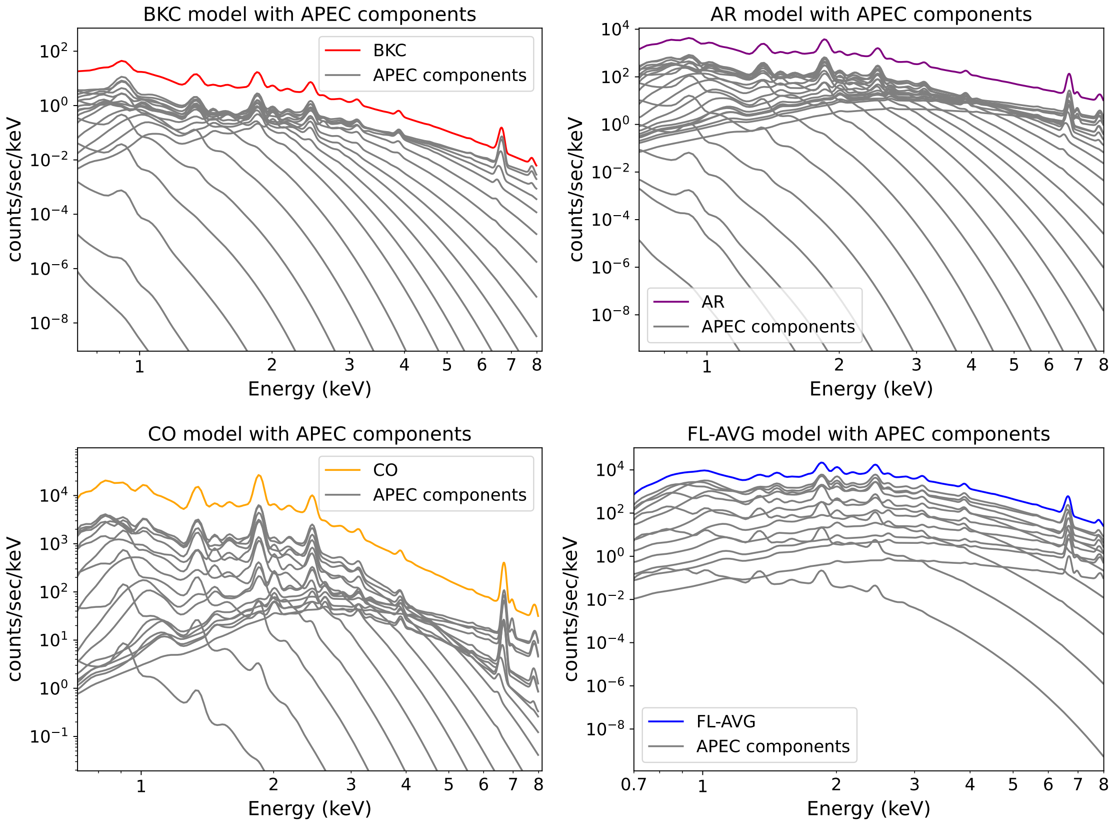

Figure 3.3: Composite SaXS spectral models made with XSPEC (colored) and their individual APEC components (grey) for the main solar coronal region types used in the SaXS method (Joseph et al., 2025). Colors indicate the coronal region type: red for the background corona (BKC), purple for the active regions (AR), yellow for the cores (CO), and blue for the averaged flares (FL-AVG).

3.4 | Normalization of spectral components

The normalizations $Norm_{i,reg}$ are fixed values obtained from the $EM_{i,reg}$ values of the region type's EMD using:

$$Norm_{i,reg} = 10^{-14} \times \frac{EM_{i,reg}}{4\pi D^2}, \tag{3.2}$$

where D is the distance to the star in cm.

3.5 | Abundance choices: APEC vs. VAPEC

Elemental abundances can be set as a global value (using the APEC model, expressed in units of solar abundances), or customized for each element individually (using the VAPEC and VAPEC variants available in XSPEC). The VAPEC models would be more appropriate when elemental abundances are already known for different temperatures on the Sun, or when applying models to stars with non-solar coronal abundances.

3.5.1 | The FIP effect

An important consideration for abundance modeling is the First Ionization Potential (FIP) effect, which describes systematic abundance variations between the photosphere and corona. Elements are categorized by their first ionization potential: low-FIP elements (FIP $<$ 10 eV, including Fe, Mg, Si, Ca, Ni, Cr) and high-FIP elements (FIP $>$ 10 eV, including O, Ne, Ar, C, N). In the solar corona, low-FIP elements are typically enhanced by factors of 3–4 relative to photospheric abundances, while high-FIP elements remain approximately at photospheric values. The physical mechanism driving this fractionation involves preferential ionization and transport of low-FIP elements from the chromosphere into the corona.

For stellar coronae, an inverse FIP (IFIP) effect is sometimes observed, where low-FIP elements are depleted relative to high-FIP elements compared to photospheric abundances. The presence and strength of FIP or IFIP effects can vary with stellar activity level and spectral type. When applying solar-derived abundance patterns to stellar spectra, these potential differences must be considered, particularly for active stars like M dwarfs where coronal conditions may differ substantially from solar values. The FIP and IFIP effects manifest as deviations of elemental abundances from those in standard coronal abundance libraries.

3.6 | Fitting spectra with multi-region models

Solar and stellar broad-band soft X-ray spectra are fit with a spectral model $M_{\rm spec}$, which is an additive combination of spectral models for various region types. The contribution from a given region $M_{\rm reg}$ can be scaled up or down during spectral fitting, with the scaling measured as the total normalization of the coronal region $Norm_{\rm reg}$. The spectral model to be fitted is:

$$M_{\rm spec} = \sum_{\rm reg} (Norm_{\rm reg} \cdot M_{\rm reg}). \tag{3.3}$$

3.7 | Deriving total emission measures and filling factors

The total emission measure per unit area of a region type on the Sun, $EM_{\rm reg,\odot}$, is:

$$EM_{\rm reg,\odot} = \sum_{i} EM_{i,reg}. \tag{3.4}$$

The total emission measure of that region type on the star, $EM_{\rm reg,tot}$, is $EM_{\rm reg,\odot}$ scaled by $Norm_{\rm reg}$ obtained from the spectral fit:

$$EM_{\rm reg,tot} = EM_{\rm reg,\odot} \cdot Norm_{\rm reg}. \tag{3.5}$$

The filling factor, $ff_{\rm reg}$, is then

$$ff_{\rm reg} = \frac{A_{\rm reg}}{A_{\rm proj,\odot}}, \tag{3.6}$$

Since on the Sun, $Norm_{\rm reg}$ is simply the projected area of that coronal region in cm^2, $ff_{\rm reg}$ on the Sun is:

$$ff_{\rm reg} = \frac{Norm_{\rm reg}}{A_{\rm proj,\odot}}, \tag{3.7}$$

where $A_{\rm proj,\odot}$ is the projected area of the solar disk.

3.8 | Accounting for coronal scale height in projected area

When observing a star in X-rays, detected emission originates not only from the visible photospheric disk but also from the extended corona above the limb. This is also true for broad-band solar X-ray spectra from DAXSS. To account for this, I include the vertical extension of the corona in the total projected area $A_{\mathrm{proj},\odot}$.

I approximate the extent of the solar corona by its scale height:

$$S_{\mathrm{BKC}} = \frac{2kT_{\mathrm{BKC}}}{\mu m_{\mathrm{H}} g_{\odot}}, \tag{3.8}$$

where $\mu = 0.6$ is the mean molecular weight of the fully ionized coronal plasma, and T_{BKC} is the emission-measure-weighted average temperature of the background corona.

The corresponding effective projected area is:

$$A_{\mathrm{proj},\odot} \simeq \pi (R_{\odot} + S_{\mathrm{BKC}})^2, \tag{3.9}$$

where $R_{\odot}$ is the solar radius. This formulation includes both the photospheric disk and the coronal layer extending approximately one scale height beyond the solar limb. The total area is approximately $A_{\mathrm{proj},\odot} \approx 1.7 \times 10^{22}\ \mathrm{cm}^2$.

4

Solar Validation Using DAXSS and *Hinode*

4.1 | Motivation and SaXS validation strategy

This chapter is based on Joseph et al. (2025) (submitted), 'The Sun as an X-ray star V.: A new method to retrieve coronal filling factors,' submitted to *Astronomy and Astrophysics*. A preprint is available at arXiv:2510.23161 under a Creative Commons CC BY 4.0 license. The SaXS method introduced here represents a new approach: defining XSPEC spectral models for different coronal region types and fitting them to observed spectra with the goal of retrieving filling factors for different types of magnetic structures from spectra alone. Before applying this method to stellar X-ray spectra, I first test it on the Sun itself.

The advantage of using the Sun is our ability to verify results using actual images. I can check two critical aspects: first, whether the method can correctly retrieve the appropriate coronal region types from spectral fitting alone, and second, whether the filling factors of those region types derived spectrally match what I observe in corresponding contemporaneous images.

Our validation approach proceeds as follows. I apply the SaXS methodology to DAXSS soft X-ray spectra, obtain the best-fitting combination of coronal region models, and derive corresponding filling factors. I then validate these spectral fit results using *Hinode*/XRT images taken closest in time.

4.2 | DAXSS observations and selection of representative spectra

I use DAXSS Level 2 data stored as mission-length NCDF files at `lasp.colorado.edu/home/minxss/data/`. Specifically, I use version 2.1.0, which covers February 28, 2022 to October 24, 2023 (the middle of the rise phase of Solar Cycle 25). DAXSS provides light curves and spectra in the 0.4 to 12.0 keV band with several spectral cadence options: native (a few minutes), one-hour, and one-day averages.

I chose to use one-hour averaged spectra, matching typical stellar spectral averaging timescales needed for sufficient photon statistics. To select representative observations, I identified two observations from the DAXSS/INSPIRESat-1 light curve with the lowest and highest count rates, aiming to capture two distinct states of solar activity. I selected the lowest count rate observation on June 29, 2022 at 12:44, which I subsequently confirmed from the GOES light curve to represent a truly quiescent state. I selected the highest count rate observation on April 25, 2022 at 02:18, which I confirmed from the GOES light curve corresponds to an ongoing M-class flare. I refer to these as our Quiescent Sun and Flaring Sun spectra, respectively.

GOES light curves acquired simultaneously show clearly different activity levels (Fig. 4.1). On April 25, an M-class flare occurred (visible in the 1 to 8 Å band), whereas June 29 showed minimal activity with only a small B-class flare barely rising above the quiescent background. For spectral fitting, I restrict the quiescent Sun spectrum to 0.7 to 3.0 keV, using a low-energy cutoff of 0.7 keV because DAXSS is not well calibrated below this threshold (Schwab et al., 2020, 2023), and an upper limit of 3.0 keV because there is minimal signal above this energy during quiet solar conditions. For the flaring Sun spectrum, I use the range 0.7 to 8.0 keV to capture the enhanced high-energy emission from the flare.

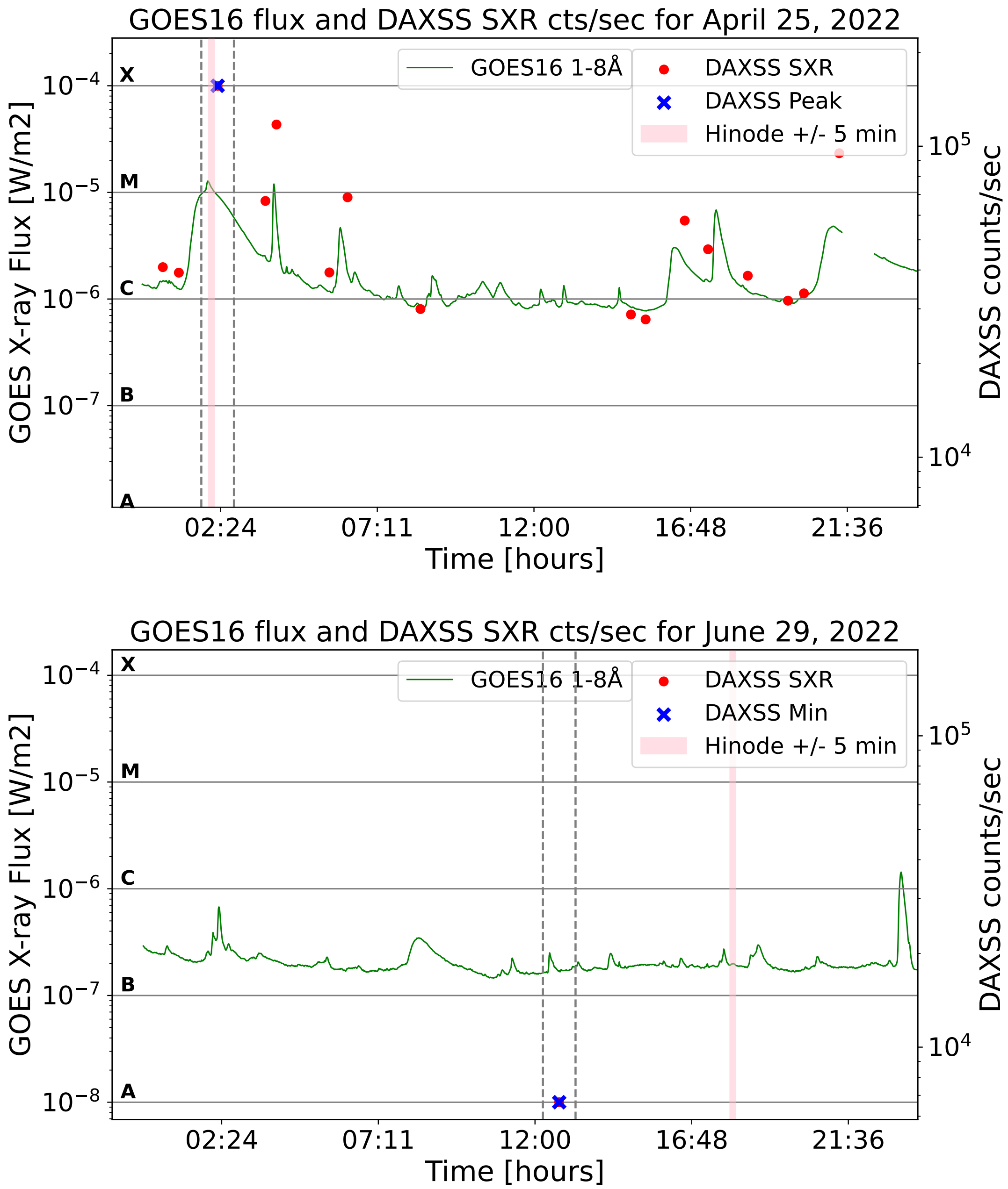

Figure 4.1: GOES X-ray flux in the 1-8 Å band (green) and DAXSS count rates for April 25, 2022 and June 29, 2022 (Joseph et al., 2025). Horizontal grey lines demarcate the GOES flare classes A, B, C, M and X. The epochs of the DAXSS spectra selected for analysis in this paper are marked in the DAXSS light curve as blue crosses and dashed vertical lines indicate the one-hour exposure time of the spectra. The *Hinode* synoptic images used to verify the SaXS method correspond to the time period indicated by the pink vertical band.

4.3 | *Hinode*/XRT observations and image preparation

I obtained *Hinode* Level 2 synoptic composite images from `http://solar.physics.montana.edu/HINODE/XRT/SCIA/latest_month.html` (Takeda et al., 2016). These synoptic composite images, which have already been sufficiently preprocessed for use in this work through the following process (Takeda et al., 2016). Full-disk images are taken 2 to 4 times daily when *Hinode* points at Sun center. Each observation consists of long and short exposure pairs in one or more X-ray filters. The pairs are used to capture the dynamic range of coronal X-ray emission: saturated pixels from the long exposure are replaced with corresponding pixels from the short exposure. The composite images combine both exposures into a single high-dynamic-range image. Additional processing includes dark current subtraction, CCD bias removal, vignetting correction, cosmic ray removal, and contamination spot correction. Images are normalized to DN s^{-1} pixel^{-1} and coaligned to heliographic coordinates.

Level 2 processing eliminates the need for most standard XRT calibrations, though light leak correction is still required for certain filters and epochs.

For this work, I use images taken closest in time to our DAXSS observations (indicated by pink vertical bands in Fig. 4.1). The April 25, 2022 image was taken at 02:06 (Flaring Sun), and the June 29, 2022 image was taken at 18:03 (Quiescent Sun).

Light leak correction deserves special attention. The light leak originated from a pinhole that developed in the XRT entrance filter on 9 May 2012, with subsequent enlargements occurring in 2015, 2017, and 2018. The effect is that visible stray light contaminates X-ray images, particularly affecting thinner filters. Ti_poly and C_poly are affected most severely, while Al_mesh and Al_poly experience moderate contamination. Correction is necessary because this contaminating visible light must be removed to obtain accurate X-ray flux measurements.

The correction method (Takeda et al., 2016; Velasquez et al., 2024) proceeds as follows. The light leak component is measured during *Hinode* eclipse seasons when visible light dominates the X-ray signal. The stray light pattern and intensity vary with filter and satellite pointing but remain roughly constant during each stray light phase. Correction involves subtracting a scaled light leak template appropriate for the observation date, filter, and pointing. Template selection accounts for CCD contamination layer thickness at the observation time.

All of these corrections are readily implemented using the XRTpy Python library (Velasquez et al., 2024), which provides standardized functions for *Hinode*/XRT data processing. The image processing I applied differs for the two dates. The April 25, 2022 image was taken with the Be_thin filter which blocks stray light, so no light leak correction was required and I used the image as-is. The June 29, 2022 image was taken with the Al_mesh filter, which experiences moderate stray light contamination. I applied light leak correction using the XRTpy function ‘remove_lightleak‘ (Velasquez et al., 2024).

The resulting images are shown in Fig. 4.2. Since fainter features are obscured due to the ongoing flare, a version of the April 25, 2022 Flaring Sun image with adjusted colorbar limits to enhance fainter features is provided in Appendix A, Fig. A.1.

4.4 | Refinement of EMDs

Initial fits using spectral models derived from the full EMDs revealed systematic discrepancies with the observed spectral shape. Specifically, observed spectra exhibit steeper high-energy drop-offs than predicted by any SaXS models in the 0.7 to 3.0 keV range (Fig. 4.3).

I attribute these discrepancies to EMD tail bins, particularly the high-temperature tails of CO, AR, and BKC, which have low emission measure values but overcontribute to the spectral models. To address this, I implement a fix based on the assumption that low-signal bins are unreliable. I restrict each EMD to bins within one order of magnitude of the peak (i.e., only high-signal bins where $EM_{i,reg} \geq EM_{\mathrm{peak}}/10$). While this empirical adjustment improves spectral fits, I emphasize that it is not a definitive solution. The restricted EMDs are shown in Fig. 4.4.

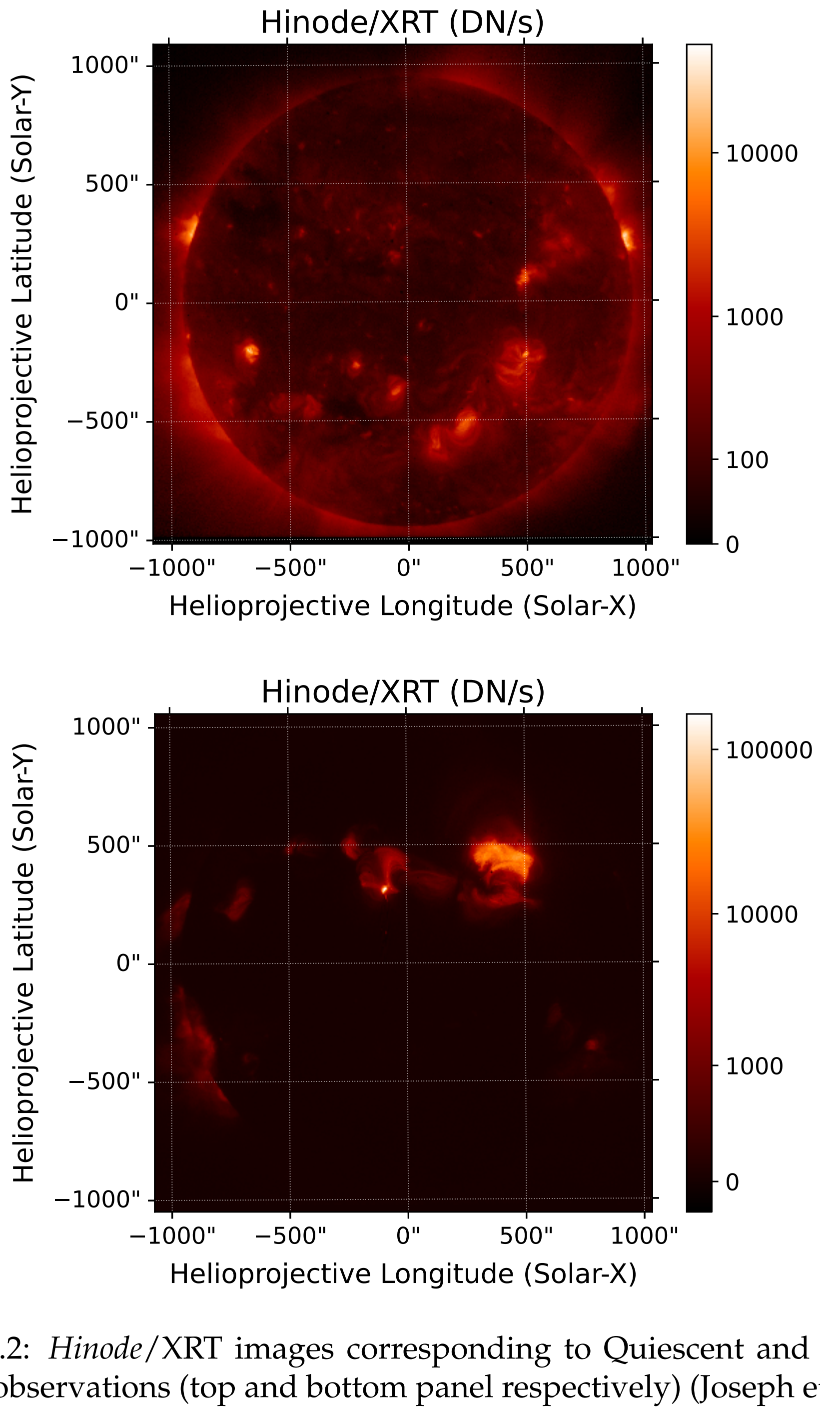

Figure 4.2: *Hinode*/XRT images corresponding to Quiescent and Flaring Sun DAXSS observations (top and bottom panel respectively) (Joseph et al., 2025).

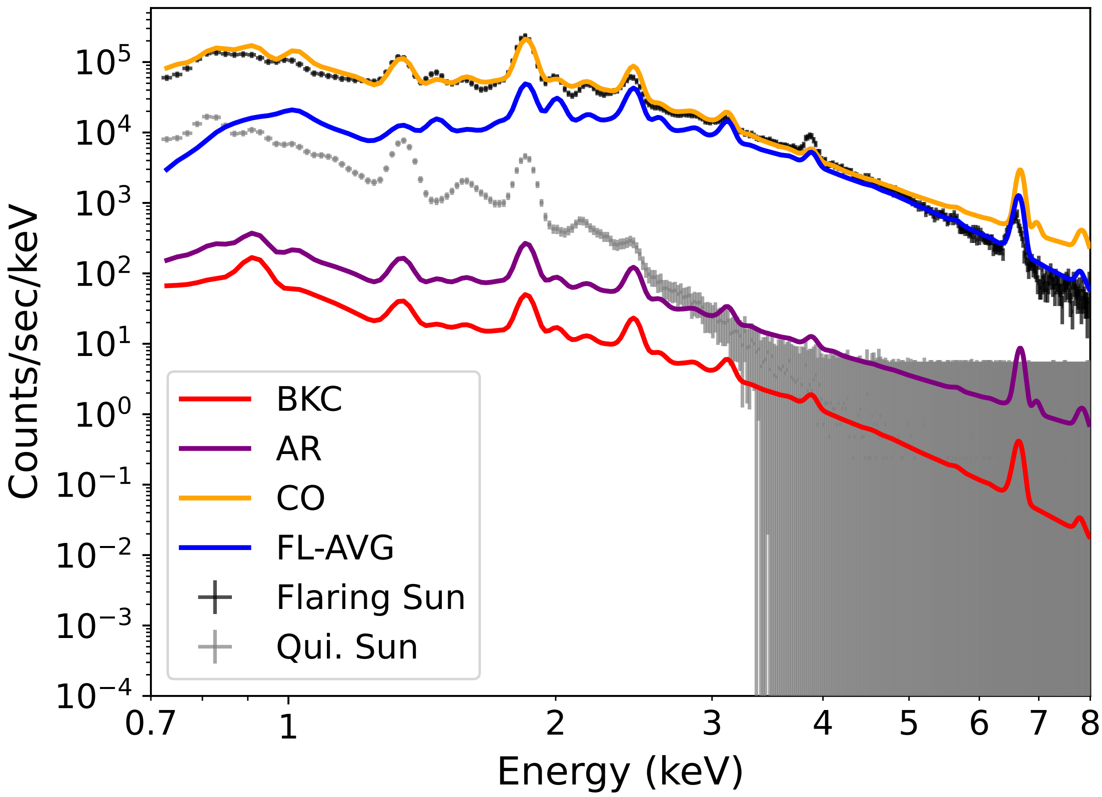

Figure 4.3: DAXSS spectra corresponding to the lowest and highest count rates in the DAXSS light curve along with arbitrarily scaled SaXS models of the various types of coronal regions (Joseph et al., 2025). This demonstrates the steeper slope of the solar spectra compared with the spectrum of all types of coronal region which indicates an over-contribution of low-signal EM bins.

I regenerated new spectral models from the restricted EMDs. Fig. 4.5 shows how the models change with this restriction.

The removed EMD bins had drastically increased flux in the high-energy portion of spectra. The restriction eliminates this inconsistency with observed DAXSS spectra. I note that the need for this ad hoc adjustment indicates that the original EMDs may not be fully representative for the region types. This is likely related to the time-evolution of magnetic structures and their associated EMDs, which I discuss further in Section 4.12.

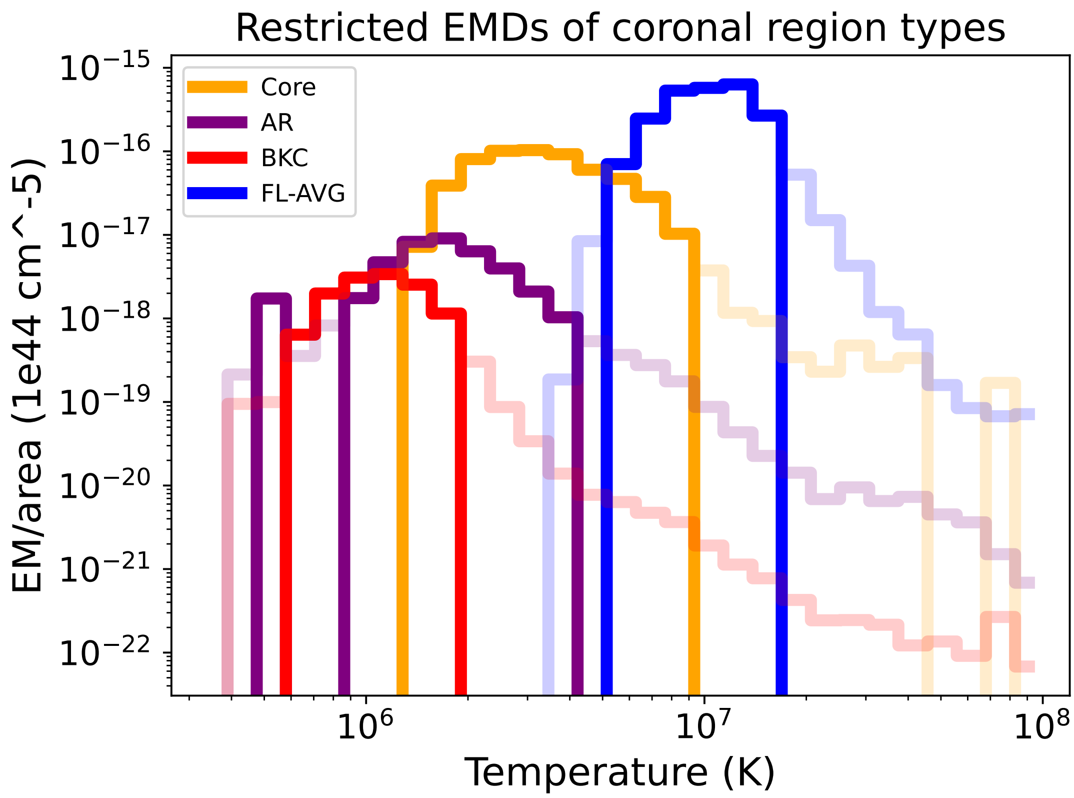

Figure 4.4: EMDs of the BKC, AR, CO and FL-AVG regions (Joseph et al., 2025). The opaque lines are the restricted distributions used in this work, and the opque and transparent lines together depict the original distributions.

4.5 | Spectral fitting methodology and constraints

I applied the SaXS XSPEC models (from Section 3) separately to the two DAXSS spectra using the restricted EMDs. Initial fits fixed elemental abundances to quiescent solar values (Feldman Standard Extended Coronal abundances; feld in XSPEC) (Feldman, 1992), with the XSPEC abundance parameter set to unity. I imposed upper limits requiring that the total filling factor be less than or equal to 100% to ensure derived projected areas do not exceed the solar corona's total projected area (as defined in Section 3).

The primary output is the filling factors ff_{reg} (Equation 3.6) for all region types in the best-fitting model. I employed a systematic testing approach, test-

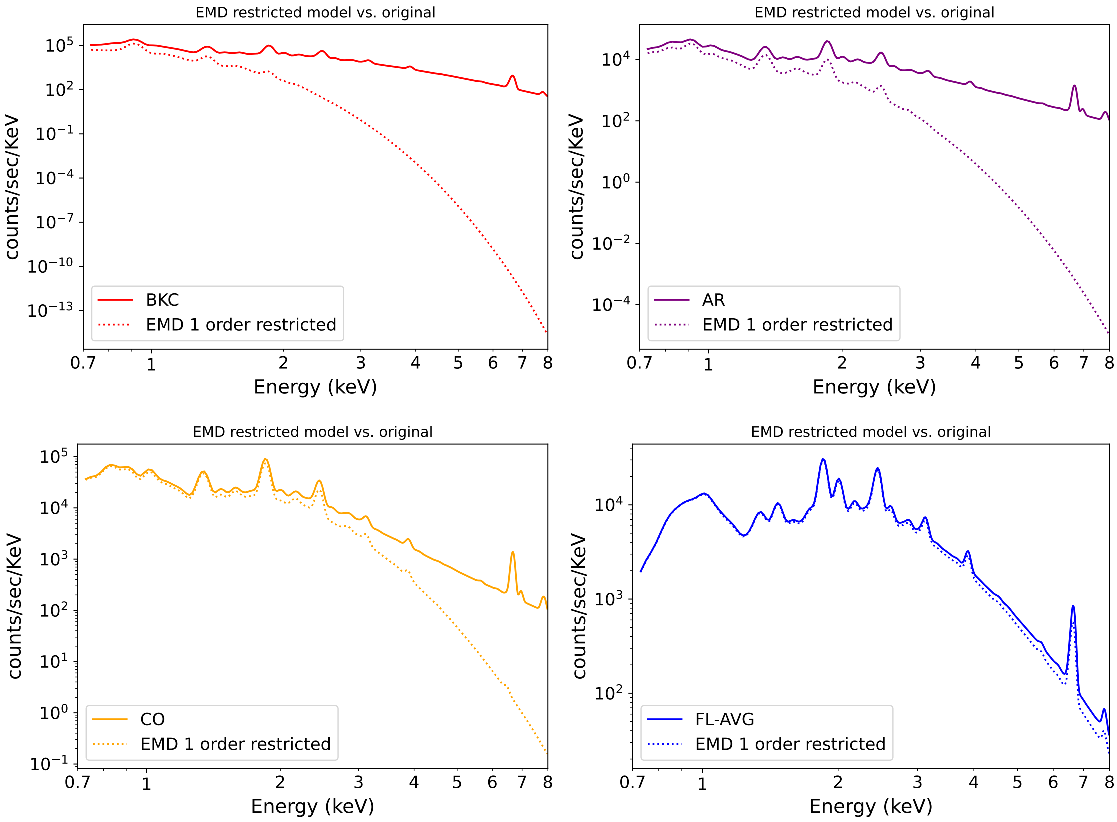

Figure 4.5: Comparison between composite SaXS spectral models in XSPEC derived from the full (solid lines) and restricted (dashed lines) EMDs for the main coronal region types (Joseph et al., 2025). Colors indicate the region type: red for the background corona (BKC), purple for active regions (AR), yellow for cores (CO), and blue for the averaged flares (FL-AVG).

ing individual components and adding components as needed based on residuals.

Because region EMDs and spectral models are defined per unit projected area, the best-fit normalization of each region template, $Norm_{\text{reg}}$, directly corresponds to the projected area (in cm^2) covered by that coronal region. As established in Equation 3.7, the filling factor is computed as:

$$ff_{\text{reg}} = \frac{Norm_{\text{reg}}}{A_{\text{proj},\odot}},$$

where $A_{\text{proj},\odot}$ is the projected area of the solar disk.

While initial fits used fixed solar abundances, significant line residuals motivated additional analysis with variable abundances and non-equilibrium ionization models (Section 4.8), which provided our best-fitting models for both observations.

4.6 | Spectral fitting results: Quiescent Sun

For single-component fits, the AR model provides the best fit with $ff_{\mathrm{AR}} = 23.54 \pm 0.31\%$ (Fig. 4.6, left panel). However, low-energy residuals suggest the need for an additional lower-temperature component.

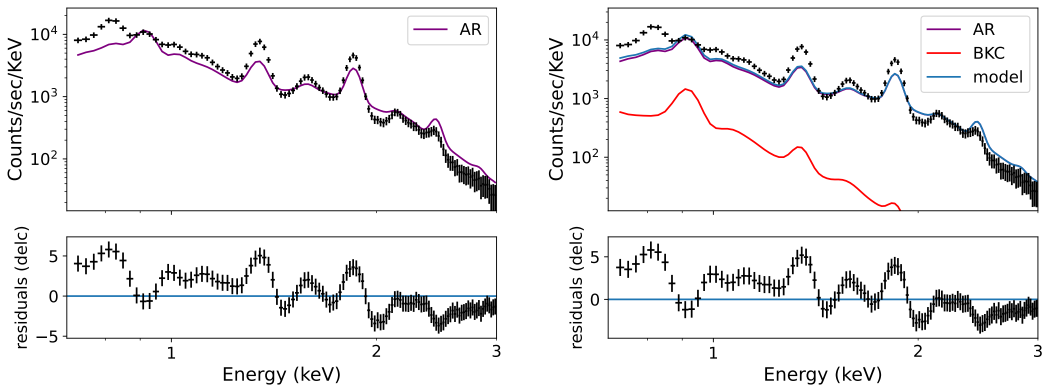

Figure 4.6: DAXSS spectrum from 29 June 2022 representing the Quiescent Sun fitted with AR model alone (left) and with added BKC component (right) (Joseph et al., 2025).

Adding a background corona component yields a two-component fit (AR plus BKC) with improved reduced chi-squared: $\chi^2_{\mathrm{red}} = 5.33$ compared to 5.78 previously. The filling factors are $ff_{\mathrm{BKC}} = 94.12 \pm 65.85\%$ and $ff_{\mathrm{AR}} = 21.83 \pm 0.4\%$. The BKC component contributes minimally to the overall spectrum, and its filling factor is poorly constrained. The AR filling factor changes only marginally with the addition of BKC. The explanation is straightforward: emission from the much brighter AR dominates the spectrum despite its smaller filling factor. The remaining residuals appear predominantly at specific emission lines, suggesting the need for region-specific abundance adjustments rather than fixed solar abundances. This motivates the refined analysis with variable abundances presented in Section 4.8.

4.7 | Spectral fitting results: Flaring Sun

Given the enhanced high-energy emission compared to the Quiescent Sun, I start with the FL-AVG model for single-component fits. This model fits the high-energy portion well but significant low-energy residuals remain, yielding $\chi^2_{\rm red} = 13.64$ (Fig. 4.7, top left panel).

A two-component fit using FL-AVG plus CO successfully fits the low-energy spectrum with strongly reduced residuals. The reduced chi-squared improves dramatically to $\chi^2_{\rm red} = 2.29$ (Fig. 4.7, top right panel). The filling factors are $ff_{\rm CO} = 4.47 \pm 0.069\%$ and $ff_{\rm FL-AVG} = 0.06 \pm 0.00068\%$.

Since cores typically accompany active regions, I tested a three-component fit adding the AR model. This yields marginal improvement with $\chi^2_{\rm red} = 2.26$. However, the AR filling factor is poorly constrained at $ff_{\rm AR} = 47.51 \pm 13.97\%$. The spectrum is dominated by core and flare emission except in the softest part. The final filling factors are $ff_{\rm CO} = 4.07 \pm 0.14\%$ and $ff_{\rm FL-AVG} = 0.062 \pm 0.00077\%$ (Fig. 4.7, bottom panel).

I also tested a four-component fit adding BKC (FL-AVG + CO + AR + BKC), but this does not further improve the fit, yielding $\chi^2_{\rm red} = 2.27$. Emission is dominated by the other regions with higher emission per unit area. The BKC component is very poorly constrained: $ff_{\rm BKC} = (5.4 \pm 1102) \times 10^{-3}\%$.

4.8 | Refining spectral fits with variable abundances and non-equilibrium ionization

Despite the improvements achieved by restricting the EMDs, significant residuals remained in both the Quiescent and Flaring Sun fits. To investigate whether these could be attributed to coronal abundance variations or departures from ionization equilibrium, I performed additional fits using variable-abundance

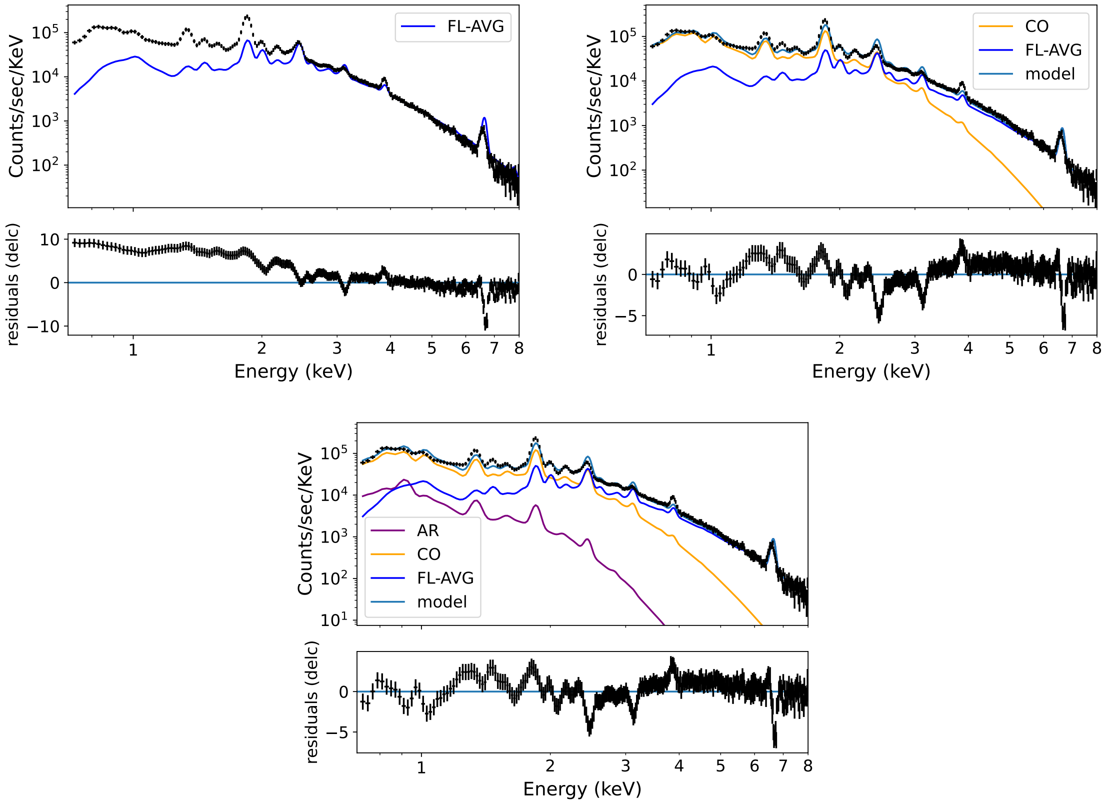

Figure 4.7: DAXSS spectrum of 25 Apr 2022, representing a flare fitted with FL-AVG alone (top left), FL-AVG + CO (top right), and FL-AVG + CO + AR (bottom) (Joseph et al., 2025).

models (VAPEC) and, for the flare component, non-equilibrium ionization models (VNEI).

Following the recommendations of Woods et al. (2023), I varied the abundances of specific elements according to the dominant region type. To reduce the number of free parameters, I tied the abundances of each element across all region types in a given fit. I allowed a 20% variation in the abundances by constraining all abundance factors to lie between 0.8 and 1.2. The derived abundance factors are listed in Table B.1 (Appendix B).

For the Quiescent Sun spectrum, incorporating variable abundances improved the fit to $\chi^2_{\text{red}} = 4.68$ (Fig. 4.8), with filling factors $ff_{\text{BKC}} = 45.20 \pm 149.53\%$ and $ff_{\text{AR}} = 21.31 \pm 5.76\%$. While this represents our best fit to the Quiescent

Sun observation, significant line residuals remain visible, and the reduced chi-squared value indicates that simultaneous constraints on both abundances and filling factors remain challenging. This suggests that, ideally, coronal abundances should be independently constrained before being applied within the SaXS framework.

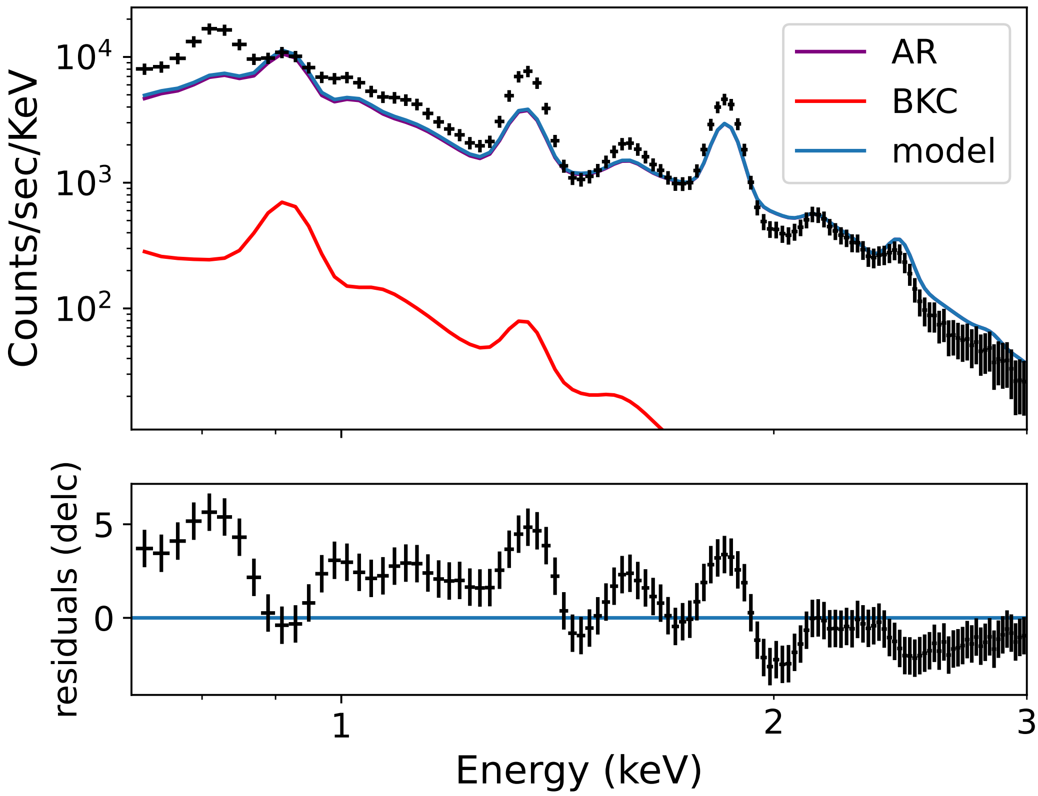

Figure 4.8: DAXSS spectrum from 29 June 2022 representing the Quiescent Sun fitted with BKC and AR models with variable abundances. This represents the best-fit model for the Quiescent Sun observation.

For the Flaring Sun spectrum, I additionally employed the VNEI model for the flare component, as flares can exhibit departures from ionization equilibrium. This introduces an additional parameter, τ, representing the ionization timescale. The resulting fit shows substantial improvement, with $\chi^2_{\mathrm{red}} = 1.16$ (Fig. 4.9) and filling factors $ff_{\mathrm{AR}} = 14.72 \pm 23.67\%$, $ff_{\mathrm{CO}} = 3.37 \pm 0.22\%$, and $ff_{\mathrm{FL}} = 0.07 \pm 0.0014\%$. The derived ionization timescale is $\tau = (2.29 \pm$

$0.21) \times 10^{11}$ s cm^{-3}. The inclusion of non-equilibrium ionization removes high-energy residuals where the equilibrium model previously overestimated line emission, demonstrating the importance of accounting for ionization state in flaring plasma.

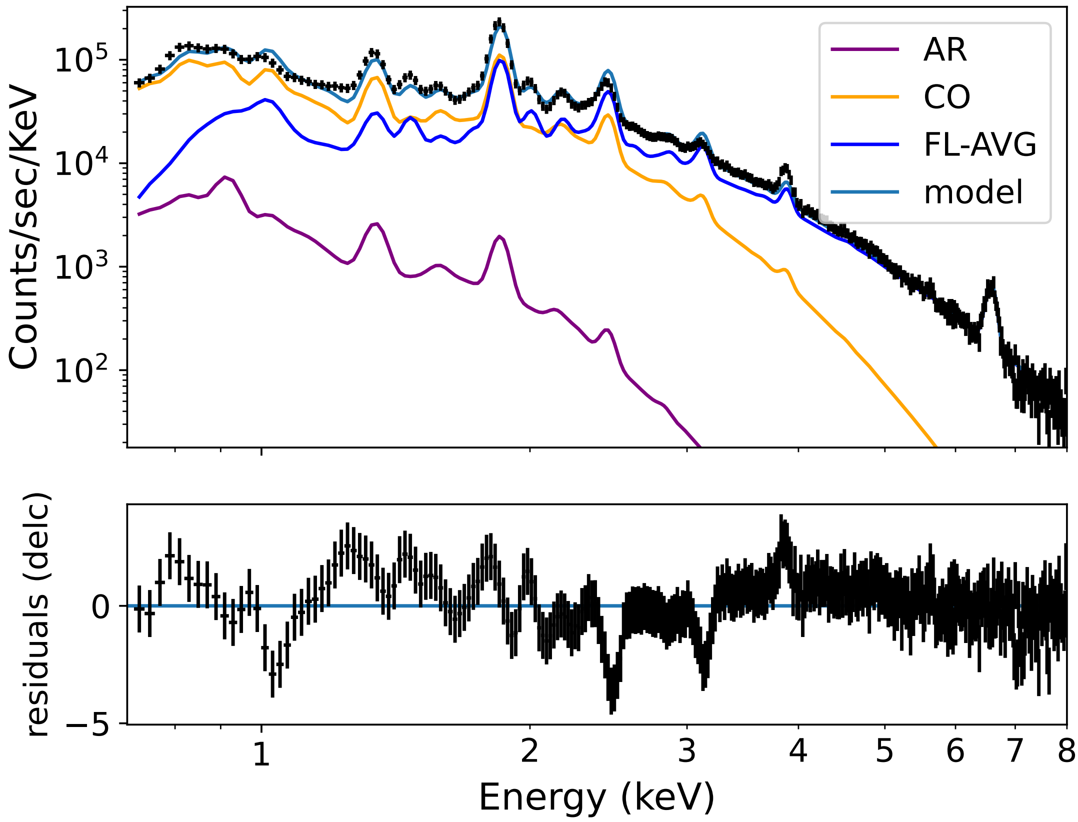

Figure 4.9: DAXSS spectrum of 25 Apr 2022, representing the Flaring Sun fitted with AR, CO, and FL-AVG models with variable abundances and non-equilibrium ionization (VNEI) for the flare component. This represents the best-fit model for the Flaring Sun observation.

4.9 | Validation with *Hinode*: image decomposition methodology

Our verification goal is to check whether filling factors inferred from spectral analysis are consistent with structures seen in contemporaneous images. The image decomposition approach proceeds as follows. Since coronal region types are defined based on *Yohkoh* pixel intensities ($I_{\mathrm{BKC}} < I_{\mathrm{AR}} < I_{\mathrm{CO}} < I_{\mathrm{FL}}$), I identify corresponding regions in *Hinode* images by progressively masking pixels based on the spectral-fit-derived filling factors.

The masking procedure works from brightest to dimmest pixels. First, I designate the brightest X% of pixels to the hottest component (e.g., FL). Then I exclude these pixels and designate the next brightest Y% as the next hottest component (e.g., CO). I continue progressively for the remaining components.

For example, in the Flaring Sun observation, the brightest 0.07% of pixels are designated as flares, the next brightest 3.37% of remaining pixels are designated as cores, and the next brightest 14.72% of remaining pixels are designated as active regions. The remaining pixels are assumed to come from regions we can't constrain well, like BKC, or not at al, like Coronal Holes.

The decomposed regions are visualized in Figs. 4.10 (Quiescent Sun) and 4.11 (Flaring Sun).

A zoom-in to the flaring region is shown in Appendix A, Fig. A.2.

Different regions are marked with different colorbars, with each region type distinguished by color. The rest of the solar corona (shown in white) is assumed to be covered by the faint background corona (BKC) or coronal holes. These fainter structures do not contribute significantly to the integrated spectrum due to their low emission per unit area.

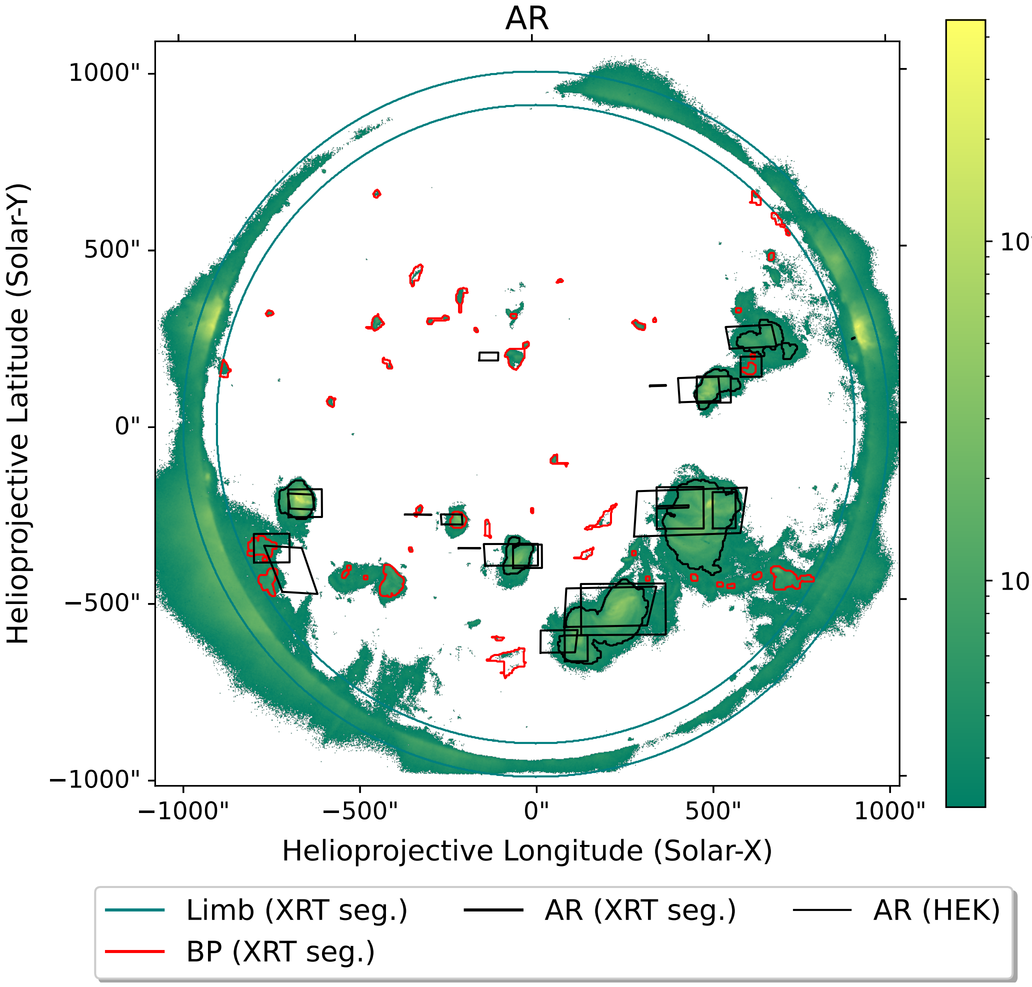

Figure 4.10: *Hinode*/XRT image during Quiescent Sun observation with highlighted pixels showing the AR component (green) identified from spectral fitting with variable abundances (see Section 4.8). The filling factors shown correspond to the refined fits using VAPEC models. The solar limb boundaries, defined by the green circles, are taken from the *Hinode* segmentation maps. The inner boundary defines the reference area used in the filling factor calculations. The black and red contours correspond to active regions and bright points, respectively, as identified in the *Hinode*/XRT segmentation database. The active regions simultaneously detected by various solar instruments and registered in the public Heliophysics Event Knowledgebase (HEK) are shown as black bounding boxes.

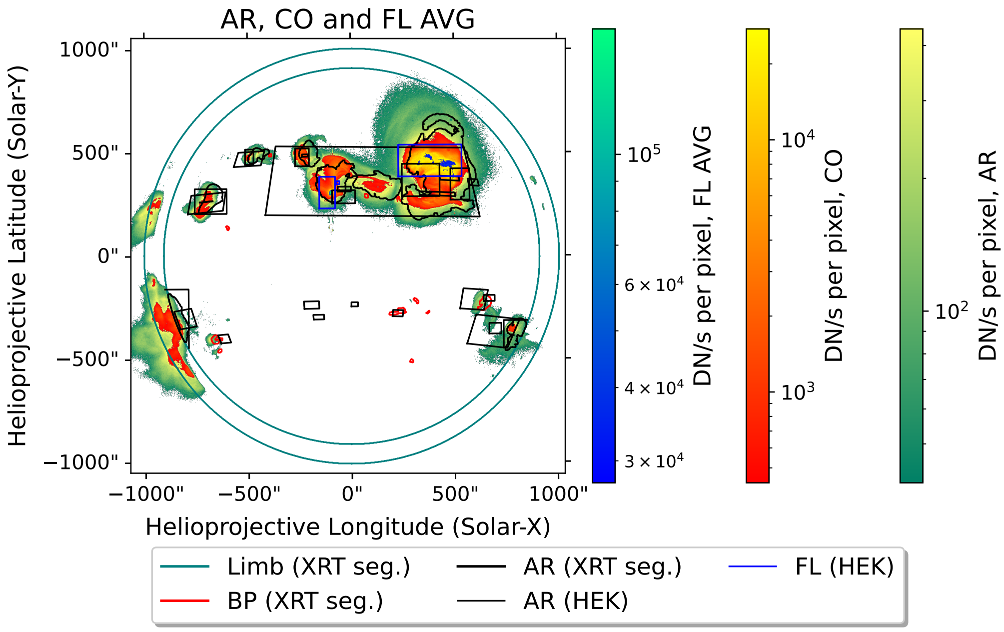

Figure 4.11: *Hinode*/XRT image taken during the Flaring Sun observation, showing pixels color-coded by coronal regions whose filling factors were determined from spectral fitting with variable abundances and non-equilibrium ionization for flares (see Section 4.8): AR (green), CO (orange), and FL (blue). The filling factors shown correspond to the refined fits using VAPEC and VNEI models. The solar limb boundaries (Limb (XRT seg.)), defined by the green circles, are taken from the *Hinode* segmentation maps. The inner boundary defines the reference area used in the filling factor calculations. The black and red contours correspond to active regions (AR (XRT seg.)) and bright points (BP (XRT seg.)), respectively, as identified in the *Hinode*/XRT segmentation database. The flares (FL (HEK)) and active regions (AR (HEK)) simultaneously detected by various solar instruments and registered in the public Heliophysics Event Knowledgebase (HEK) are shown as black and blue bounding boxes, respectively.

4.10 | Validation with independent solar catalogs

I use two independent sources for comparison. The Heliophysics Event Knowledgebase (HEK) (Hurlburt et al., 2012) aggregates active region and flare identifications from multiple solar observatories (not necessarily limited to X-ray observations or *Hinode* data). It provides rough bounding boxes for active regions (AR) and flares (FL), shown as black and blue boxes in Figs. 4.10 and 4.11. I use HEK despite the rough nature of these bounding boxes because it is the only catalog that includes flare regions. The *Hinode*/XRT segmentation database (Adithya et al., 2021) provides more precise segmentation maps for active regions (AR) and bright points (BP), shown as colored contours, and also provides inner and outer solar limb boundaries.

An important note about these catalogs: while the acronyms (AR, FL, BP) match SaXS region types, both the definitions and segmentation methods differ. Catalog features are identified morphologically in images, whereas SaXS components are defined by characteristic thermal structure. In addition, the segmentation methods themselves vary: HEK uses rough bounding boxes from multiple instruments, while the *Hinode*/XRT database uses detailed morphological segmentation. The reference area for catalog filling factors is the inner solar limb boundary, as features in the databases are restricted to within this boundary.

4.11 | Comparison of filling factors

Table 4.1 summarizes the filling factors from SaXS spectral analysis versus those from the databases.

For the Flaring Sun observation (2022 April 25), HEK bounding boxes yield an AR filling factor higher than XRT segmentation. Several factors contribute to this discrepancy. First, different instruments and observatories contribute to HEK, each using different region-identification methods that may not be based

Table 4.1: Comparison of coronal-region filling factors (%) derived from SaXS spectral analysis and from image-based catalogs. The SaXS filling factors presented here are derived from spectral fits with variable abundances (Quiescent Sun) and variable abundances plus non-equilibrium ionization for the flare component (Flaring Sun), as described in Sect. 4.8.

Observation Date	**Region Type**	**SaXS (this work)**	**HEK**[a]	***Hinode*/XRT**[b]	**Notes**
2022 Apr 25 (Flaring Sun)	AR	14.72 ± 23.67	19.91	7.66 (7.93 AR+BP)	Flaring Sun DAXSS spectrum
	CO	3.37 ± 0.22	—	—	Not segmented in image databases
	FL-AVG	0.07 ± 0.0014	2.25	—	Only from HEK bounding boxes
2022 Jun 29 (Quiescent Sun)	AR	21.31 ± 5.76	8.06	4.02	Quiescent Sun DAXSS spectrum
	BKC	45.20 ± 149.53	—	—	Not segmented in image databases

Notes. Filling factors (FF) represent the fractional area of the solar disk within the solar limb (as defined by the *Hinode* /XRT segmentation maps) occupied by each coronal region.

[a]HEK: bounding boxes of active regions and flares from multiple solar missions (Hurlburt et al., 2012).

[b]*Hinode* /XRT: segmentation maps of active regions and bright points from Adithya et al. (2021).

on X-ray observations. Second, HEK bounding boxes are inherently rough approximations compared to the detailed morphological segmentation in the *Hinode*/XRT database. Third, there is a temporal mismatch: the XRT segmentation was performed at 05:48 UT (approximately 3 hours after the *Hinode* composite at 02:06 UT). This time offset explains the slight spatial displacement between XRT contours and the visible regions in our analysis.

For the Quiescent Sun observation (2022 June 29), HEK bounding boxes again yield higher AR filling factors than *Hinode* segmentation. In this case, temporal effects are negligible since the Sun was in a quiet phase with no major activity changes. The discrepancy instead reflects the different instruments, observatories, and classification techniques contributing to HEK versus the uniform methodology of the *Hinode*/XRT segmentation database. Absolute agreement is not expected due to these intrinsic methodological and instrumental differences.

The key finding is that the same dominant coronal structures (active regions and flaring sites) are consistently identified across all approaches.

4.12 | Interpretation of Filling Factor Discrepancies

SaXS spectral filling factors differ from database-derived values for systematic reasons. HEK data and XRT segmentations are restricted to features within the solar limb, whereas SaXS-derived maps include emission extending up to one solar scale height above the limb. The rationale is to better capture total coronal output as is observed by DAXSS. This difference in spatial coverage contributes to the offset between our spectral filling factors and those from morphological catalogs.

Additional emission captured by SaXS is clearly visible in Figs. 4.10 and 4.11 as colored areas outside the inner circle (solar limb), and a substantial fraction of AR emission originates from beyond the limb.

An important consideration is that the EMDs of coronal regions vary with time as magnetic structures evolve (Orlando et al., 2004; Reale et al., 2001), as discussed in Section 2.7. The EMDs I use here are time-averaged representations derived from multiple observations. Perfect agreement between our results and instantaneous images is therefore not expected, as the time-averaged templates may not precisely match the thermal structure at any single moment.

The strengths of this validation include successful identification of dominant region types and good consistency with imaging for region locations and relative contributions. The limitations include the need for empirical EMD restriction (one order of magnitude from peak), testing on only two representative observations, some components being poorly constrained (particularly BKC in both cases), and the use of time-averaged EMDs that may not capture instantaneous variations. The refined analysis with variable abundances (Section 4.8) addresses some spectral residuals and provides improved filling factor constraints, particularly for the Flaring Sun observation. Future work should pursue systematic validation across various activity levels using a larger sample of solar data to better characterize the method's performance under diverse conditions.

4.13 | Discussion of Solar Validation

4.13.1 | Summary of validation results

The primary achievement is that the SaXS method successfully retrieves filling factors of coronal regions from spectral fits alone, reproducing the spatial distribution observed in contemporaneous *Hinode*/XRT images. Table 4.1 summarizes the filling factors obtained from SaXS spectral fits compared to image-based catalogs, demonstrating the method's ability to identify the correct dominant coronal region types and their approximate spatial coverage. This represents the first direct comparison between spectral-fit-derived filling factors and spatially resolved imaging, validating the method's core approach.

4.13.2 | Residuals and abundance uncertainties

Despite successful filling factor retrieval with fixed solar abundances, residuals remained visible at specific emission lines in the initial spectral fits. The likely cause is that I assumed uniform standard solar coronal abundances for all regions, but actual abundances may vary between region types.

To address this, I performed refined fits using variable-abundance models (VAPEC) and non-equilibrium ionization models (VNEI) for flares, as described in Section 4.8. Following Woods et al. (2023), I varied abundances within a 20% range (0.8–1.2) and tied them across all region types to limit free parameters. This substantially improved spectral fits, particularly for the Flaring Sun observation where the inclusion of non-equilibrium ionization reduced χ^2_{red} from 2.26 to 1.16.

However, even with variable abundances, the Quiescent Sun fit achieved only $\chi^2_{\text{red}} = 4.68$, indicating that simultaneous constraints on both abundances and filling factors remain challenging. This demonstrates that while the SaXS method successfully retrieves filling factors that match spatial observations, optimal spectral fits require careful treatment of coronal abundances.

For future solar validation work, the recommended approach is to constrain abundances independently from preliminary 2-T VAPEC fits to representative spectra, then incorporate these as fixed parameters in the multi-component SaXS models. This approach would account for deviations from standard Feldman coronal abundances while avoiding parameter explosion during SaXS fitting.

4.13.3 | EMD restriction methodology

Our current approach to EMD restriction is based on two complementary considerations. First, I observed that low-signal emission measure bins (those far from the peak) likely contain unreliable measurements and contribute disproportionately to high-energy spectral flux without accurately representing the characteristic thermal structure of each region type. Second, I restricted EMDs based on how the spectral model shape changes when bins are added or removed, keeping only those bins within one order of magnitude of the peak emission measure. This ensures that the high-signal bins, which capture the essence of each coronal region's plasma distribution, dominate the spectral models while removing potentially unreliable low-signal tails.

However, this restriction methodology has important limitations. The empirical test was performed on only two DAXSS spectra (quiescent and flaring), which is not robust across the full range of solar activity conditions. The *Yohkoh*/SXT EMDs themselves were derived from a limited number of observations spanning specific solar cycle phases, and may not capture the full range of coronal variability.

To establish more reliable EMD restrictions, future work requires systematic testing using a large volume of DAXSS spectra spanning different activity levels. This would determine statistically which EMD bins are essential for reproducing observed spectra and whether the one-order-of-magnitude restriction generalizes beyond our initial two test cases.

4.13.4 | Soft X-ray energy coverage limitation

An important caveat to our solar validation is that DAXSS spectra are limited to energies above approximately 0.7 keV due to instrumental constraints. This means our validation does not fully test the soft X-ray regime below 0.7 keV, where cooler coronal plasma (particularly the background corona) produces significant emission. The BKC component, which is already poorly constrained due to its weak emission relative to hotter components, may be additionally affected by this energy cutoff since BKC emission peaks at lower energies than AR, CO, or FL components.

For stellar applications like AD Leo where *XMM-Newton* provides coverage down to 0.2 keV, the SaXS models are applied across a broader energy range than was validated with solar data. While the hotter components (CO, FL) that dominate stellar emission are well-tested by DAXSS, the cooler, dimmer BKC component could not be reliably constrained. Future solar validation should incorporate instruments with lower energy coverage (such as soft X-ray telescopes on sounding rockets or future missions) to fully validate the SaXS method across the complete soft X-ray band.

5

Application to AD Leo

AD Leo (spectral type M3.5V) is a nearby, highly active M dwarf known for frequent and energetic flaring activity. Its fully convective interior and high coronal activity make it an ideal target for testing whether solar-derived SaXS models can describe stellar coronae.

5.1 | AD Leo observations and data processing

5.1.1 | *XMM-Newton* observations

I analyze a continuous X-ray observation of AD Leo taken with the *XMM-Newton* EPIC/pn camera. Observation 0891801301 was conducted on Nov 18/19, 2021, with a duration of 85 ksec and contains "The Nov 2021 November 2021 Great Flare of AD Leo," a superflare analyzed in detail by Stelzer et al. (2022). The observation was taken with SMALL WINDOW MODE pointing.

5.1.2 | Data reduction

I extracted X-ray light curves and spectra using *XMM-Newton* Science Analysis Software (SAS) version 21.0.0, which is the standard pipeline for processing *XMM-Newton* data. For event list filtering, I removed time intervals of high background activity. I accepted pixel patterns satisfying $0 \leq \text{pattern} \leq 4$, quality flags equal to 0, and event channels in the range $200 \leq \text{PI} \leq 12000$.

Source detection was performed in five standard *XMM-Newton* energy bands: 0.2 to 0.5 keV, 0.5 to 1.0 keV, 1.0 to 2.0 keV, 2.0 to 4.5 keV, and 4.5 to 12.0 keV. For region selection, I used a circular source extraction region centered on the source position with radius 35 arcsec. The background region was an adjacent circular region with the same radius.

5.1.3 | Light curve extraction and characteristics

I extracted the light curve from EPIC/pn with the following processing. The light curve was binned at 100 s, background-subtracted using the SAS task EPICLCCORR, and barycentric correction was applied using the SAS tool BARYCEN. The full light curve is shown in Fig. 5.1.

The observation reveals complex behavior. Three distinct flares are identified: Flare 1 and Flare 2 (smaller events, early in observation), and the November 2021 Great Flare (Fig. 5.1). Long intervals between flares show apparent quiescent periods with fluctuations in count rate and small-amplitude variability, but no large, clearly identifiable flares except the three main events. However, closer inspection reveals hidden variability: smaller flares and continuous low-level activity are embedded in the nominal quiescent phase (Fig. 5.2).

The November 2021 Great Flare exhibits distinct phases as described in detail by Stelzer et al. (2022). The temporal evolution of the November 2021 Great Flare is shown in detail in Fig. 5.3. The fast rise phase shows a rapid increase to the peak (marked by squares in Fig. 5.3). This is followed by a plateau with sustained high count rate at peak (marked by stars). The exponential decay phase shows an initial decay following an exponential profile (marked by plus signs). Finally, the linear decay phase exhibits later gradual decay with approximately linear profile (marked by crosses). The count rate did not return to the pre-flare quiescence by the end of the observation.

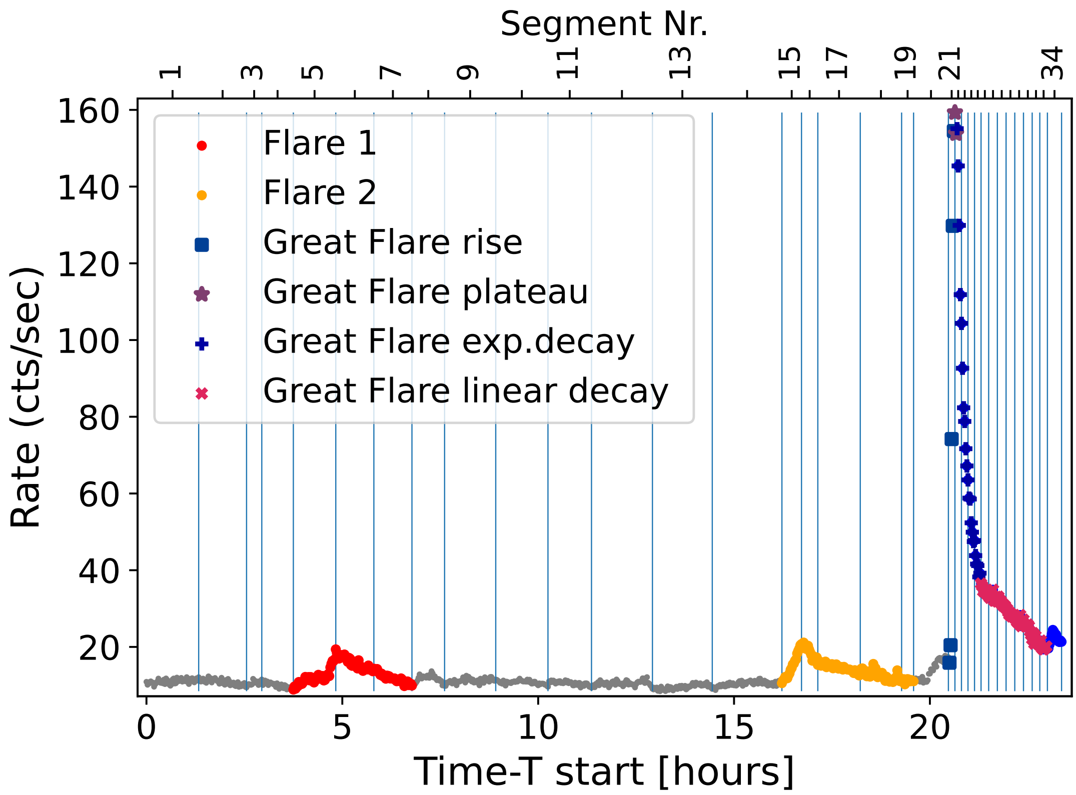

Figure 5.1: *XMM-Newton* EPIC/pn light curve for AD Leo observation 0891801301 (Nov 18/19, 2021), showing three distinct flaring episodes: Flare 1 and Flare 2 (smaller events occurring early in the observation) and the November 2021 Great Flare, which dominates the latter portion of the observation. Different colors mark the temporal phases of each flare, and the light curve reveals significant variability even during nominally quiescent periods between flaring events. Figure 5.2 shows the same light curve zoomed in to the smaller flares.

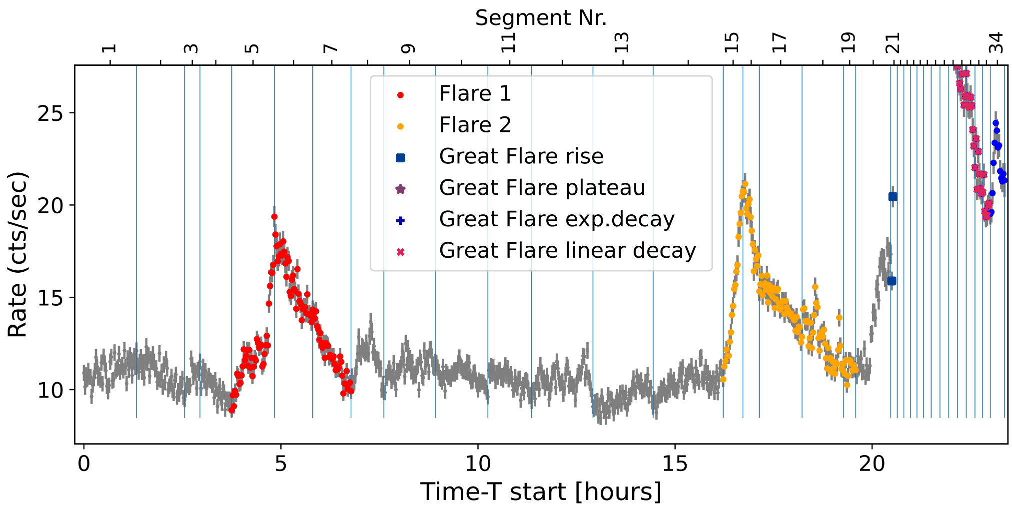

Figure 5.2: Zoomed-in view of the Flare 1 and Flare 2 region of the AD Leo *XMM-Newton* EPIC/pn light curve (observation 0891801301; see Figure 5.1 for the full light curve). This expanded view reveals smaller-amplitude variability that is hidden when viewing the full observation, including minor flares and continuous low-level activity between the major flaring episodes. The persistent activity during these nominally quiescent intervals illustrates that even "quiescent" periods on active M dwarfs may contain significant magnetic activity.

5.1.4 | Spectral extraction and segmentation

Time segments for time-resolved spectroscopy were determined by eye based on relatively little variability in count rate (marked by blue lines in Fig. 5.1, Fig. 5.2 and Fig. 5.3). Spectra were extracted for each identified interval. The observation was divided into 34 intervals, with the November 2021 Great Flare portion divided into 5 intervals (instead of the 17 used by Stelzer et al. (2022), since complex SaXS spectral models require higher signal spectra).

I applied spectral corrections to account for Out-of-Time (OoT) events, which constitute 1.1% of events in Small Window mode (Strüder et al., 2001; XMM-Newton Science Operations Centre, 2025). These are photons registered during CCD readout rather than integration time. I subtracted background spectra using the background region described above. All spectra were binned with a

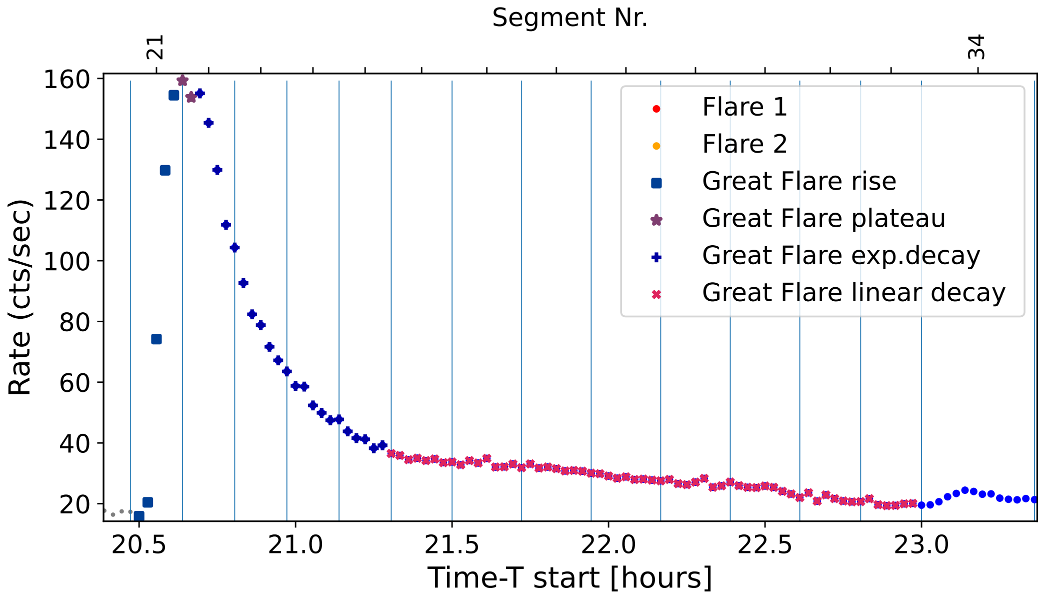

Figure 5.3: Zoomed-in view of the November 2021 Great Flare from AD Leo *XMM-Newton* EPIC/pn light curve (observation 0891801301; see Figure 5.1 for the full light curve). Four distinct evolutionary phases are marked: the rise phase (squares), plateau (stars), exponential decay (plus signs), and linear decay (crosses). The count rate remains elevated above the quiescent level even at the end of the observation, indicating an extended post-flare cooling timescale. This temporal structure informs the spectral segmentation strategy described in Section 5.1.4.

minimum of 80 counts after applying the above corrections.

5.2 | Spectral modeling approach for AD Leo

I use VAPEC components instead of APEC to allow non-solar abundance adjustments, setting coronal abundances of individual elements to values measured by Stelzer et al. (2022) on the XMM-Newton/RGS spectrum of AD Leo from the same observation. I leave the Fe abundance free to vary between 0 and 1.5 as conservative limits. Fe is left free because it produces the strongest and most numerous X-ray lines, so it largely controls the fit and is well constrained by the data. Fixing it to a solar value would bias the derived temperatures and emission measures, especially since stellar coronal Fe abundances are often non-solar.

I tie Fe abundances together across all region types, such that the only free parameters during spectral fits are (1) the same Fe abundance for all coronal regions, and (2) individual normalizations of each region type, $Norm_{\text{reg}}$. For example, a model composed of M_{BKC} plus M_{CO} has one Fe abundance and two normalizations ($Norm_{\text{BKC}}$ and $Norm_{\text{CO}}$), yielding three free parameters total. For each time segment, I fit SaXS spectral models to the data, and the fits yield total emission measures (Eq. 3.5) for each region type.

With five types of coronal regions (BKC, AR, CO, FL-AVG, FLX9), there are $2^5 - 1 = 31$ possible model combinations, each of which could describe AD Leo's corona at a given time. I systematically test different model combinations for each time segment to identify the best-fitting combination.

5.3 | Modified filling-factor derivation for AD Leo

To derive filling factors for AD Leo, I must first determine the projected area occupied by each coronal region type. For the Sun, the spectral fit normalization $Norm_{\text{reg}}$ maps directly to the projected area of the corresponding coronal region (see Sect. 3.7). For stars with coronal electron densities that differ significantly from the Sun, however, this direct correspondence no longer holds. AD Leo, as a highly active M dwarf, harbors coronal electron densities substantially higher than those of the Sun, likely due to enhanced chromospheric evaporation driven by its elevated flare activity (Maggio et al., 2004; Ness et al., 2004). As a result, $Norm_{\text{reg}}$ cannot be used directly as a proxy for projected area as in the solar case.

Instead, I use the normalization as a scaling factor to recover the total emission measure of each coronal region. Combined with electron densities measured independently for AD Leo, this emission measure can then be used to derive the physical volume of the coronal region, from which the projected area and ultimately the filling factor are obtained. This procedure differs for loop-based regions (AR, CO, FL) versus the diffuse background corona (BKC), as I describe in the following subsections.

5.3.1 | Total emitting volume

I use the definition of volume emission measure: $EM = \int_V n_e n_H dV$, where V, n_e, and n_H are the volume, electron density, and hydrogen ion density of the plasma respectively. For fully ionized plasma with solar composition, $n_H \approx 0.8 n_e$ (due to electrons from ionized metals), so this is often approximated as $EM \approx \int_V n_e^2 dV$.

I derive the total line-of-sight volume occupied by each coronal region type, V_{reg}:

$$V_{\text{reg}} = \frac{EM_{\text{reg,tot}}}{n_{e,\text{reg}}^2}. \tag{5.1}$$

Electron densities $n_{e,reg}$ are obtained from literature values derived from high resolution X-ray spectra using density-sensitive line ratios. The density diagnostic method works as follows. Coronal densities are measured using ratios of density-sensitive emission lines (e.g., Fe XXI, Si XIII) where the line intensity ratio depends on collisional de-excitation rates, which are density-dependent. At low densities, collisional de-excitation is negligible and the line ratio is constant. At high densities, collisional de-excitation competes with radiative decay and the line ratio becomes density-sensitive (Porquet et al., 2001, 2010). This method provides a direct constraint on the electron density n_e for plasma near the peak formation temperature of the ion from which the line ratio is measured.

Table 5.1 summarizes electron densities measured for AD Leo from published X-ray spectroscopic studies using density-sensitive line ratios, along with measurements for EV Lac (another M dwarf) for comparison.

I establish a density-temperature relationship by fitting literature measurements of n_e versus T from Table 5.1 in log-log space. The fitting procedure plots literature measurements as $\log(n_e)$ versus $\log(T)$ and performs a linear fit: $\log(n_e) = a + b \cdot \log(T)$, finding $a = 3.99$ and $b = -14.8$. The fit is shown in Fig. 5.4 as a green line with a 1σ uncertainty band (grey shaded region). Literature measurements are shown as filled black circles. Crosses mark upper-limit flare densities re-estimated from the constraint that filling factors must be greater than or equal to the projected area of a single coronal loop (discussed in Section 5.8).

Table 5.1: Electron densities for AD Leo coronal plasma measured from density-sensitive X-ray line ratios reported in the literature. Columns show: reference (Paper), electron density with lower and upper uncertainties ($\log(n_\mathrm{e})$, $\log(n_\mathrm{e})_\mathrm{low}$, $\log(n_\mathrm{e})_\mathrm{up}$), ion triplet used for the diagnostic (Lines; e.g., O VII, Ne IX, Si XIII, Fe XXI), plasma temperature with upper uncertainty ($\log(T\,[\mathrm{K}])$, $\log(T\,[\mathrm{K}])_\mathrm{up}$), and X-ray instrument. Measurements for EV Lac, a similar M3.5V star, from Osten et al. (2006) are included to expand the available data. The density diagnostic method, which uses collisionally excited line ratios that become density-sensitive at high densities, is described in the text. These literature measurements establish the density-temperature relationship (shown in Fig. 5.4) used to derive electron densities for each SaXS coronal region type.

Paper	$\log(n_\mathrm{e})$	$\log(n_\mathrm{e})_\mathrm{low}$	$\log(n_\mathrm{e})_\mathrm{up}$	**Lines**	$\log(T\,[\mathrm{K}])$	$\log(T\,[\mathrm{K}])_\mathrm{up}$	**Instrument**
Maggio et al. (2004)	9.85	9.041	10.185	O VII	6.29	–	LETG
Maggio et al. (2004)	11.59	11.362	11.881	Ne IX	6.44	6.44	LETG
Maggio et al. (2004)	13.99	13.568	14.279	Si XIII	6.9	6.9	LETG
Maggio et al. (2004)	12.26	11.477	12.613	Fe XXI	7.02	–	LETG
Ness et al. (2004)	10.40	10.28	10.52	O VII	6.3	–	RGS1
Ness et al. (2004)	9.92	9.18	10.66	O VII	6.3	–	LETG
Ness et al. (2004)	10.50	10.25	10.75	O VII	6.3	–	MEG
Ness et al. (2004)	–	–	12.0	Ne IX	6.6	–	MEG
Ness et al. (2004)	11.5	11.0	12.0	Ne IX	6.6	–	HEG
Stelzer et al. (2022)	10.69	10.477	10.903	O VII	6.3	–	RGS
Stelzer et al. (2022)	11.9	11.0	12.26	Ne IX	6.6	–	RGS
Osten et al. (2006) (EV Lac)	–	–	13.0	Fe XVII	7.0	–	MEG+HEG
Osten et al. (2006) (EV Lac)	–	–	13.26	Si XIII	6.9	–	MEG+HEG
Osten et al. (2006) (EV Lac)	13.0	12.63	13.42	Mg XI	6.9	–	MEG+HEG
Osten et al. (2006) (EV Lac)	–	–	11.23	Ne IX	6.7	–	MEG+HEG
Osten et al. (2006) (EV Lac)	10.48	9.94	10.98	O VII	6.4	–	MEG+HEG
Sanz-Forcada and Micela (2002)	12.9	12.7	–	Fe XIX–XXII	7.0	–	EUVE

LETG: Low Energy Transmission Grating (Brinkman et al., 2000) aboard the *Chandra* X-ray Observatory (Weisskopf et al., 2000).

RGS / **RGS1**: Reflection Grating Spectrometer (den Herder et al., 2001) aboard *XMM-Newton* (Jansen et al., 2001).

MEG / **HEG**: Medium Energy Grating and High Energy Grating of the High Energy Transmission Grating Spectrometer (HETGS; Canizares et al., 2005) aboard the *Chandra* X-ray Observatory (Weisskopf et al., 2000).

EUVE: Extreme Ultraviolet Explorer (Bowyer and Malina, 1991), a NASA mission operating in the 70–760 Å bandpass, decommissioned in 2001.

To obtain the electron density $n_{e,\mathrm{reg}}$ for each SaXS region type, I evaluate this fit at a characteristic temperature T_{reg} representative of that region. I define T_{reg} as the emission-measure-weighted average temperature over the region's EMD,

$$T_{\mathrm{reg}} = \frac{\sum_i T_{i,\mathrm{reg}}\, EM_{i,\mathrm{reg}}}{\sum_i EM_{i,\mathrm{reg}}}, \tag{5.2}$$

where the index i runs over each temperature-emission measure bin in the region's EMD. Evaluating the density-temperature fit at T_{reg} then yields the corresponding electron density $n_{e,\mathrm{reg}}$ for each region. The resulting values for each SaXS region type (BKC, AR, CO, FL-AVG) are shown as open colored circles in Fig. 5.4.

I then extract the corresponding $n_{e,reg}(T_{\mathrm{reg}})$ from the density-temperature fit function evaluated at the characteristic temperature. For each SaXS region type (BKC, AR, CO, FL-AVG), I evaluate the fit at the characteristic temperature to obtain $n_{e,reg}$, shown as open colored circles in Fig. 5.4.

For flare regions, initial application of literature-derived densities to FL-AVG and FLX9 yielded filling factors smaller than the projected area of a single coronal loop, which is unphysical. I therefore re-estimated the flare densities by enforcing the constraint that the filling factor of the flare regions must be no smaller than that of a single flaring loop, $f_{\mathrm{flare}} \geq f_{1\,\mathrm{loop}}$; the iterative refinement procedure is described in Sect. 5.6.2. These re-estimated values are shown as crosses in Fig. 5.4.

5.3.2 | Projected area for background regions

I treat the background corona (BKC) as an unstructured half shell-like component, corresponding to the stellar hemisphere facing the observer, not composed of individual loops. I calculate the projected area as:

$$A_{\mathrm{BKC}} = \frac{V_{\mathrm{BKC}}}{S_{\mathrm{BKC}}}, \tag{5.3}$$

where S_{BKC} is the pressure scale height of the corona:

$$S_{\mathrm{BKC}} = \frac{2kT_{\mathrm{BKC}}}{\mu m_H g_{\mathrm{star}}}, \tag{5.4}$$

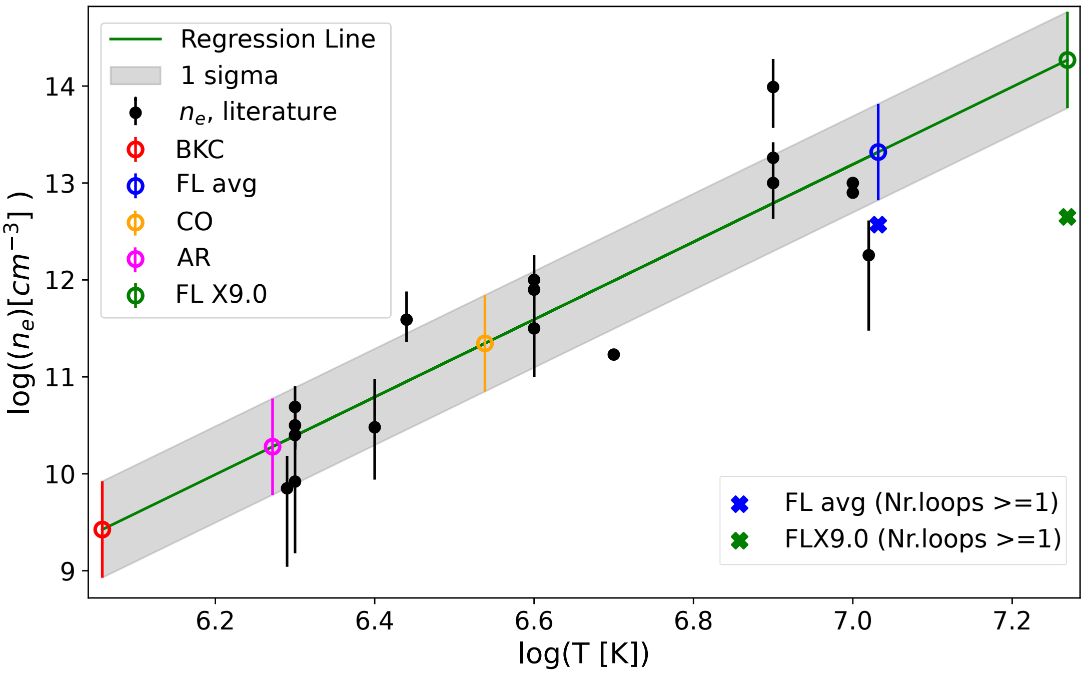

Figure 5.4: Electron density as a function of temperature for AD Leo coronal plasma. Literature measurements obtained from density-sensitive X-ray line ratios are shown as filled black circles, with sources listed in Table 5.1.The green line shows a linear fit in log-log space, with the 1σ uncertainty band indicated by the grey shaded region. Open colored circles show the electron densities derived for each SaXS coronal region type (BKC, AR, CO, FL-AVG) by evaluating the fit at the emission-measure-weighted characteristic temperature of each region (Eq. 5.2). Crosses mark the re-estimated upper-limit flare densities for FL-AVG and FLX9, obtained by enforcing the physical constraint that the flare filling factors must satisfy $f_{\text{flare}} \geq f_{1\,\text{loop}}$, i.e., the filling factor must be no smaller than that of a single coronal loop (see Sect. 5.6.2).

where k is the Boltzmann constant, $T_{\rm BKC}$ is the emission-measure-weighted average temperature of the background corona (from Equation 5.2), $\mu = 0.6$ is the mean molecular weight for fully-ionized coronal plasma, m_H is the hydrogen mass, and $g_{\rm star}$ is the surface gravity of AD Leo.

5.3.3 | Calculating Filling Factors for Loop-based regions

The AR, CO, and FL regions are composed of individual plasma-trapping magnetic loops. I approximate loops geometrically as half-toruses with loop semi-lengths L (see Fig. 5.5). The half-torus geometry is defined by inner radius r and outer radius R. Following common practice (Golub et al., 1980; Reale, 2014), I assume $r = 0.1L$. From the half-torus geometry, $R = \frac{2L}{\pi} - r$. Therefore, the geometric properties are determined solely by L.

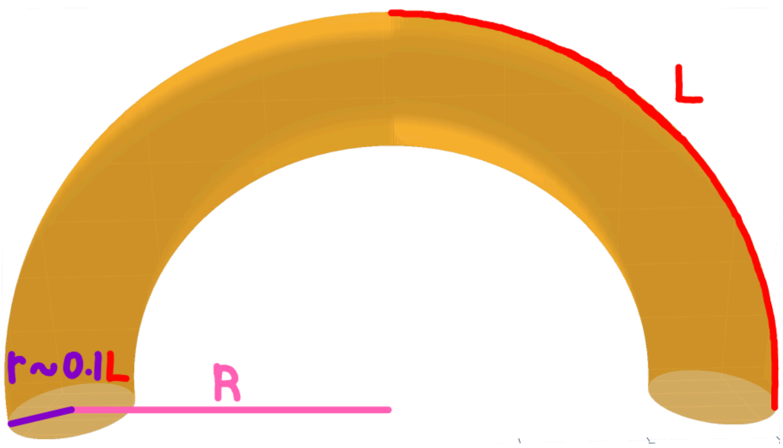

Figure 5.5: Geometric representation of coronal loop approximated as half-torus. The loop is characterized by semi-length L, inner radius $r = 0.1L$, and outer radius $R = \frac{2L}{\pi} - r$.

The volume of a single loop is $V_{1\,\rm loop} = \pi^2 r^2 R$. The number of loops in a region is:

$$N_{\rm loops,reg} = \frac{V_{\rm reg}}{V_{1\,\rm loop}}. \tag{5.5}$$

where $V_{\rm reg}$ is the total volume occupied by loop-based coronal region types, i.e., AR, CO and FL.

For determining loop semi-length, I use different approaches depending on the region type. For static loops in local thermodynamic equilibrium (typical of AR and CO), I use the Rosner-Tucker-Vaiana (RTV) scaling law (Rosner et al., 1978):

$$L_{\mathrm{reg}} = \frac{1.3 \times 10^6 T_{\mathrm{reg}}^2}{n_{e,reg}}, \tag{5.6}$$

where 'reg' stands for AR or CO. For dynamic loops of FL regions, I use a lower estimate of loop semi-lengths measured on AD Leo and other M dwarfs using the method by Reale et al. (1997), which estimates loop semi-lengths from X-ray light curve decay:

$$L_{\mathrm{FL}} = 10^9\,\mathrm{cm}. \tag{5.7}$$

Calculating projected area requires special attention because projected areas of coronal loops depend heavily on loop orientation with respect to the observer's line of sight. Analytical closed-form solutions for the projected area of non-convex bodies like half-toruses do not exist for arbitrary orientations. Therefore, I numerically estimate the average projected area along the line of sight for a single loop. I rotate a torus of loop semi-length L through a 2D grid of angles corresponding to possible longitudinal and latitudinal angles on AD Leo (0 to 180°, corresponding to the visible hemisphere). I numerically calculate the projected area of the loop for each pair of angles, then average over the grid of projected areas to obtain $\langle A_{\mathrm{projected,1\,loop}} \rangle$. I find $\langle A_{\mathrm{projected,1\,loop}} \rangle$ to be $\approx 2.8e18\,\mathrm{cm}^2, 1.28e15\,\mathrm{cm}^2$ and $2.6e17\,\mathrm{cm}^2$ for AR, CO and FL respectively. The total projected area of a region is:

$$A_{\mathrm{reg}} = N_{\mathrm{loops,reg}} \cdot \langle A_{\mathrm{projected,1\,loop}} \rangle. \tag{5.8}$$

Finally, I find the filling factors ff_{reg} using Equation 3.6.

5.4 | Initial spectral fitting: first iteration of SaXS method

I applied every possible combination of SaXS models (BKC, AR, CO, FL-AVG, FLX9) to each spectrum in the observation. Since any combination of coronal region types could plausibly describe the corona at a givenn time, I systematically tested all 31 possible combinations ($2^5 - 1$) across all 34 time segments spanning approximately 24 to 25 hours.

Our model selection criterion was based on reduced χ^2: for each spectrum, I selected the combination yielding the lowest χ^2_{red} (closest to 1) as the best fit, considering fits with $\chi^2_{\mathrm{red}} < 2$ as statistically acceptable. This approach allowed us to track how filling factors evolved throughout the observation using the best-fit model combinations. The resulting filling factor evolution from this initial fitting approach is shown in Fig. 5.6, with a zoom-in to the November 2021 Great Flare in Appendix A.3. The complete set of spectral fits for all segments is presented in Appendix D.

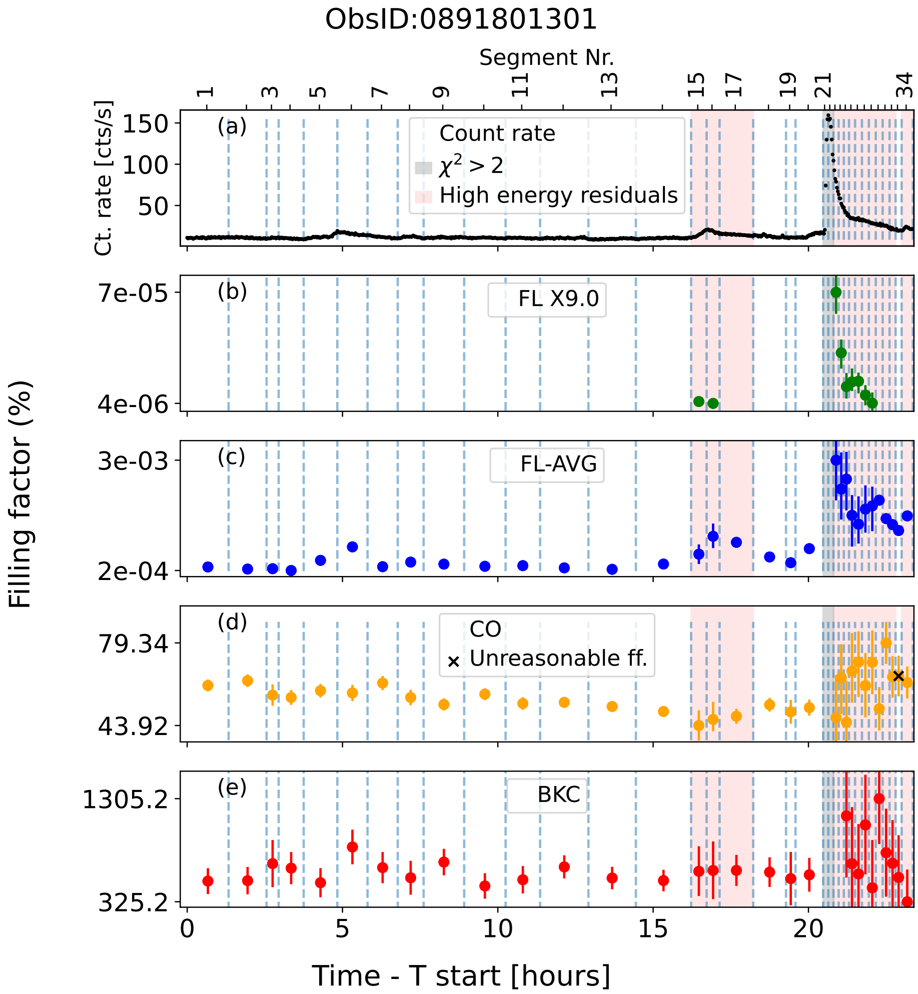

Figure 5.6: Filling factor evolution for AD Leo observation 0891801301 using the first iteration of the SaXS method. The top panel shows the X-ray count rate light curve. The bottom four panels show the filling factor evolution for the FLX9.0, FL-AVG, CO, and BKC coronal region types, respectively. Several segments are flagged for further scrutiny: grey-shaded segments (21–22) correspond to spectral fits with $\chi^2_{\mathrm{red}} > 2$, indicating poor fit quality, while pink-shaded segments (15–17, 23–32, 34) have formally acceptable reduced chi-squared values ($\chi^2_{\mathrm{red}} < 2$) but exhibit systematic residuals at high energies. Segment 33, marked with a black cross, has a good spectral fit but yields an unreasonably large CO filling factor, making it suspect. The nature of these flagged segments and the general interpretation of the filling factor evolution are discussed in Sect. 5.5. A zoomed-in view of the November 2021 Great Flare region is provided in Fig. A.3 in Appendix A, and the complete set of spectral fits for all segments is presented in Appendix D.

5.5 | Identification of problematic segments

5.5.1 | Poor fits during flare rise and peak

Segments 21 and 22 correspond to the rise and peak phases of the November 2021 Great Flare, representing the most energetic phases of the flaring event. Even the best-fit model combinations yield poor reduced chi-squares ($\chi^2_{\text{red}} \approx 3$ to 4), indicating that SaXS models are inadequate to describe the extreme emission during these phases. These segments are marked with gray shading in Fig. 5.6.

5.5.2 | Systematic high-energy residuals

I identified segments 15, 16, 17 (during a small flare), and 23 to 32, 34 (November 2021 Great Flare decay and aftermath, excluding segment 33) as problematic, marked with pink bands in Fig. 5.6. Although these segments achieve $\chi^2_{\text{red}} < 2$ (statistically acceptable), visual inspection of the spectral fits reveal systematic high-energy residuals. The models fit the low-energy portion well but fail to capture high-energy emission.

In attempting to compensate for the missing high-energy component, the fitting algorithm appears to artificially scale up normalizations of cooler components. This is suggested by the observation that filling factors of cores and flares are comparatively high during these segments. The physical implication is likely the presence of plasma hotter than any component in the solar-derived models, though I cannot rule out other interpretations without additional diagnostics.

5.5.3 | Unrealistic filling factors: segment 33

Segment 33 shows a reasonable fit ($\chi^2_{\text{red}} < 2$) with no obvious systematic residuals. However, the core region filling factor jumps dramatically from approximately 43% before the Great Flare to 62%, which is unrealistic for the static CO region. I interpret this as a coincidental good fit with a physically unrealistic filling factor, suggesting the model combination is inappropriate. I therefore identify segment 33 as problematic despite acceptable statistics. Segment 33 is marked with a cross in Fig. 5.6.

5.5.4 | Poorly constrained background corona filling factors

Across all segments, the background corona (BKC) filling factors are severely overestimated, ranging from 300% to 1300%, which is physically impossible since filling factors must be below 100%. Additionally, the uncertainties on BKC filling factors are extremely large, indicating that this component is poorly constrained by the spectral fits. This problem was already encountered during the solar validation with DAXSS spectra (Section 4): because emission from the background corona is comparatively weak, the much brighter emission from other coronal regions dominates the spectral fits, leaving the BKC component essentially unconstrained.

The solution to this problem is described in Section 5.6, where BKC is defined as the residual coverage after accounting for all other components.

5.5.5 | Unphysically low flare filling factors

Initial spectral fits yield flare filling factors smaller than the projected area of a single coronal loop ($f_{\text{flare}} < f_{1\,\text{loop}}$), which is physically impossible. This violates the basic geometric constraint that a flare region must occupy at least the area of one magnetic loop structure. The root cause is likely overestimated electron densities: since $f \propto EM/n_e^2$, systematically high densities produce artificially low filling factors. The densities used for flares come from extrapolation of literature measurements from M dwarf flares, which have large uncertainties and were measured at lower temperatures than the super-hot plasma observed here.

5.5.6 | Sudden jumps in filling factors after flare peak

Segments 23-34, which follow immediately after the peak of the November 2021 Great Flare (segment 22), exhibit a striking pattern: the filling factors of all coronal regions—including BKC, CO, and flare components—suddenly jump to higher values (Fig. 5.6). This is particularly puzzling for static coronal structures like the background corona and active region cores, which evolve on timescales of hours to days, not minutes. Such rapid increases across all components are physically implausible and suggest either: (1) a systematic fitting artifact due to missing high-temperature components, or (2) a real physical phenomenon such as post-flare coronal restructuring involving arcade flares and mass injection into existing loops.

I designate all segments 15 to 17 and 21 to 34 as "problematic segments" requiring refined analysis to address these problems.

5.6 | General solutions applied to all segments

Before presenting the two alternative approaches, which I term as Solution 1 and Solution 2, for handling the problematic segments, I first describe two general solutions that apply to all time segments throughout the observation.

5.6.1 | BKC filling factor from residual coverage

As identified in Section 5.5.4, the BKC filling factor cannot be reliably constrained from spectral fit normalizations alone because BKC emits comparatively little relative to brighter coronal components. I therefore adopt a complementary approach for all segments:

$$ff_{\text{BKC}} = 100\% - \sum_{\text{other regions}} ff_{\text{reg}},$$

where the sum runs over all non-BKC components (CO, FL-AVG, FLX9, and VAPEC components where applicable). This ensures physically realistic filling factors while acknowledging that weak BKC emission cannot be reliably constrained through direct spectral fitting alone.

5.6.2 | Flare density refinement

Initial spectral fits yield flare filling factors smaller than the projected area of a single coronal loop ($f_{\text{flare}} < f_{1\,\text{loop}}$), which is physically impossible. This occurs in both non-problematic and problematic segments, indicating systematically overestimated flare densities from literature extrapolations.

To enforce the physical constraint, I identify the segment with the lowest flare filling factor and recompute the flare density such that this minimum filling factor equals exactly $f_{1\,\text{loop}}$. This establishes a lower limit: when I apply this recomputed density to all other segments, their filling factors necessarily correspond to at least one or more loops.

Using the relation $V_{\text{reg}} = EM_{\text{reg,tot}}/n_{e,reg}^2$ and geometric constraints, I solve for $n_{e,\text{flare}}$ that yields $f_{\text{flare}} = f_{1\,\text{loop}}$ for the minimum segment. The result is density-consistent flare filling factors throughout the entire observation.

This density refinement is applied universally in both Solution 1 and Solution 2 described below.

5.6.3 | Special treatment for segments 21-22

Segments 21 and 22 (rise and peak of the November 2021 Great Flare) are handled identically in both Solution 1 and Solution 2. These segments yield unacceptably poor fits with SaXS models alone ($\chi^2_{\text{red}} \approx 3$–$4$), indicating that the solar EMD library cannot describe the most extreme phases of the superflare. For these segments, both solutions freeze the baseline coronal components (BKC, CO, FL-AVG) to their mean values from non-problematic segments and add two VAPEC components to capture the super-hot emission.

The two solutions differ only in their treatment of the remaining problematic segments (15-17, 23-34), as described in the following subsections.

5.7 | Solution 1: VAPEC Components for High-Temperature Emission

5.7.1 | Physical interpretation: super-solar flares on AD Leo

I hypothesize that flares occurring during segments 15-17 and 20-34 on AD Leo are far more energetic than any observed on the Sun, exceeding even the X9.0 solar flare used in the SaXS model library. This leads to two main consequences. First, solar-derived flare models cannot capture the extreme high-energy emission from these super-flares, resulting in systematic high-energy residuals because no available model component can reproduce the hottest plasma. Second, in the absence of an appropriate high-temperature component, the fitting algorithm compensates by artificially inflating normalizations (and hence filling factors) of cooler components (AR, CO, FL-AVG).

An additional observation supports the super-solar flare hypothesis: the FLX9 (X9.0 solar flare) component appears only in the problematic segments, never in the non-problematic segments. This pattern suggests that FLX9 is not representing an actual X9-class flare on AD Leo, but rather is being artificially selected by the fitting algorithm to partially compensate for emission from plasma far hotter than even the hottest solar flare in our model library. This reinforces the need for additional high-temperature components beyond the solar-derived models.

Solution 1 addresses these problems by adding high-temperature VAPEC components to capture super-hot plasma beyond the solar temperature regime.

This solution uses the general procedures described in Section 5.6 for BKC definition and flare density refinement, which are applied to all segments. The difference lies in how the problematic segments are treated: baseline components are frozen and VAPEC components are added.

5.7.2 | Methodology

As the first step, I establish a baseline corona by computing mean filling factors for BKC, CO, and FL-AVG in non-problematic segments (segments not in the suspect list: 1 to 14, 18 to 20). I assume that the background corona, core regions, and typical flare activity remain relatively stable, with deviations in problematic segments driven by an additional super-hot flare component.

In the second step, I freeze the normalizations of BKC, CO, and FL-AVG to their mean values from non-problematic segments when fitting the problematic segments (15 to 17, 21 to 34). This constrains the baseline coronal structure to remain constant throughout the observation.

In the third step, I fit two additional VAPEC components on top of the frozen baseline models to capture the additional high-temperature emission. Our hypothesis is that at least one VAPEC component will have a temperature exceeding 1 keV, hotter than any solar component. The free parameters are the temperature and emission measure of the additional VAPEC component(s).

5.7.3 | Results of refined analysis

The refined analysis yields a dramatic improvement in fit quality. High-energy residuals disappear, and all refined fits achieve good χ^2_{red} values. Individual spectral fits showing the refined SaXS plus VAPEC models for all problematic segments are presented in Appendix D. The results confirm our hypothesis. Additional VAPEC components fit to temperatures significantly exceeding solar flare models, with some reaching several keV. Table C.1 (Appendix C) summarizes the temperatures and emission measures of the VAPEC components for each segment, comparing the refined fits to the initial SaXS-only results. The emission measure evolution of the hot VAPEC components traces the shape of the X-ray light curve during flare rise, peak, and decay. This yields physically motivated filling factors: baseline corona filling factors remain stable, and temporal variability is captured by the high-temperature flare component rather than artificial inflation of cooler components.

Notably, the FLX9 component is not required in any of the refined fits once the high-temperature VAPEC components are included. This confirms that FLX9 was artificially selected in the initial SaXS-only fits to partially compensate for the missing super-hot emission, rather than representing a true X9-class flare.

After all refinements—frozen baseline components, additional VAPEC components, and the density adjustments described in Section 5.6.2—the final filling factors from this solution are as follows: background corona $ff_{\mathrm{BKC}} = 36$–52%, core regions $ff_{\mathrm{CO}} = 50$–66%, and flares $ff_{\mathrm{FL-AVG}} \sim 7 \times 10^{-3}$–$2 \times 10^{-2}\%$.

Constraining the filling factor of the super-hot VAPEC flare component requires additional information beyond the spectral fits. Stelzer et al. (2022) derived a loop semi-length of 4×10^{9} cm from emission measure decay analysis during the November 2021 Great Flare. From this loop size, I estimated the average projected area and filling factor of a single loop (0.12%) using the methodology described in Section 5.3.3. The emission measure decay method used by Stelzer et al. (2022) differs fundamentally from the SaXS approach, which derives filling factors directly from the normalized spectral models and assumes characteristic EMDs for each coronal region type. The filling factor evolution with the refined approach is shown in Fig. 5.7.

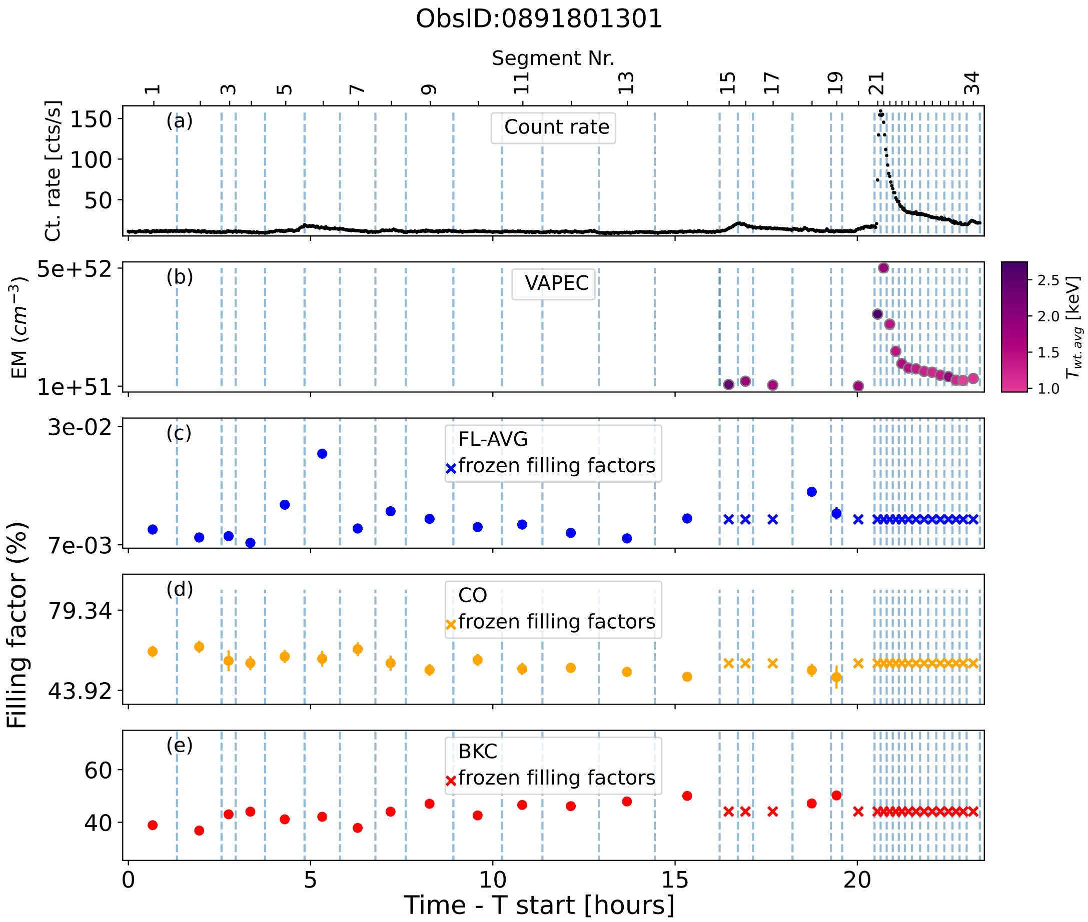

Figure 5.7: Refined filling factor evolution for AD Leo observation 0891801301 using Solution 1. Top panel: X-ray count rate (light curve). Second panel (purple scatter points with color gradient): Emission measure evolution of the additional high-temperature VAPEC components, with color indicating temperature (pink = cooler, dark purple = hottest, reaching several tens of MK). The emission measure traces the flare light curve shape. Bottom three panels: Filling factor evolution for baseline coronal components FL-AVG, CO, and BKC, which are frozen to mean values from non-problematic segments (indicated by crosses). Zoom-in view of the November 2021 Great Flare region is shown in Fig. A.4 in Appendix A.

5.8 | Solution 2: Physical restructuring interpretation

5.8.1 | Physical interpretation: post-flare coronal restructuring on AD Leo

I hypothesize that the observed patterns in problematic segments (15-17, 23-34)—sudden jumps in filling factors and systematic high-energy residuals—may represent real physical phenomena rather than purely fitting artifacts. This leads to two main physical processes. First, the November 2021 Great Flare triggers sympathetic flaring and post-flare arcade formation (see Sect. 2.4.1), causing genuine increases in emission from multiple coronal regions simultaneously. Second, the flare drives mass injection through chromospheric evaporation, filling pre-existing coronal loops with denser plasma and elevating electron densities in core regions.

For context, segments 15 to 17 contain a small flare, while segments 21 to 34 contain the Nov 2021 November 2021 Great Flare of AD Leo (Stelzer et al., 2022).

Several observations support this physical restructuring interpretation. The FLX9 (X9.0 solar flare) component appears throughout problematic segments, potentially representing actual elevated flare activity rather than an artificial fitting artifact. The filling factors of cores and flares increase during and after the November 2021 Great Flare (segments 23-34), consistent with post-flare arcade formation and enhanced magnetic activity. For post-flare segments specifically, I find that freezing core filling factors to pre-flare values while allowing densities to vary yields elevated core densities —consistent with mass injection filling loops without changing their geometric coverage.

Additionally, high-energy residuals in this solution are interpreted as arising from missing high-energy bins in our restricted EMDs rather than requiring temperatures beyond the solar regime. The solar EMDs were restricted to one order of magnitude in emission measure based on limited testing. If the full

EMD tails extending to higher temperatures and emission measures are real but were excluded by our restriction criteria, they would manifest as systematic high-energy residuals even when the underlying SaXS framework remains appropriate.

Solution 2 addresses these problems by allowing SaXS models to capture temporal evolution, interpreting observed changes as potentially real post-flare dynamics including arcade flares, mass injection, and density enhancement.

This solution uses the general procedures described in Section 5.6 for BKC definition and flare density refinement, which are applied to all segments. The difference lies in how the problematic segments are treated: SaXS models are fitted without freezing components, allowing for temporal evolution and post-flare density adjustments.

5.8.2 | Methodology

As in the first SaXS iteration described in Section 5.4, $Norm_{\mathrm{reg}}$ is allowed to vary freely for all regions throughout the observation. The key distinction is how filling factors are derived from these fitted norms.

For flare components (FL-AVG and FLX9), filling factors are derived using the refined loop densities from Section 5.6.2, using the same procedure.

For CO, post-Great Flare increases in $Norm_{\mathrm{CO}}$ (segments 23–34) are interpreted as density enhancements rather than geometric expansion of the emitting volume. The core filling factor is therefore held fixed at the mean pre-flare value (averaged over segments prior to segment 21). With the filling factor (and therefore emitting volume V_{reg}) and $EM_{\mathrm{reg,tot}}$ fixed, variations in $Norm_{\mathrm{CO}}$ are converted to variations in electron density $n_{e,\mathrm{CO}}$ via Eq. 5.1.

5.8.3 | Results

In this approach high-energy residuals in spectra remain but are interpreted as products of missing EMD bins in the parent EMD libraries rather than requiring temperatures beyond the solar regime.

The final filling factors are: $ff_{\mathrm{BKC}} = 36$–52%, $ff_{\mathrm{CO}} = 50$–66% (held fixed post-flare, with density allowed to vary), FL-AVG $\sim 7 \times 10^{-3}$ to 9×10^{-2}%, and FLX9 $\sim 7 \times 10^{-3}$ to 1×10^{-1}%. The FLX9 component, present throughout problematic segments, is interpreted as potentially real elevated flare activity rather than an artifact.

For post-flare segments (23–34), freezing the core filling factor and allowing density to vary yields $n_{e,\mathrm{CO}}$ increasing from 2.2×10^{11} to 2.8×10^{11} cm^{-3}, consistent with chromospheric evaporation filling pre-existing loop structures with denser plasma following the November 2021 Great Flare.

The filling factor and density evolution for this solution is shown in Fig. 5.8, with a zoom-in to the problematic segments in Appendix A (Fig. A.5). A comparison of the goodness of spectral fits from Solution 1 and Solution 2 are provided in Table C.1 (Appendix C).

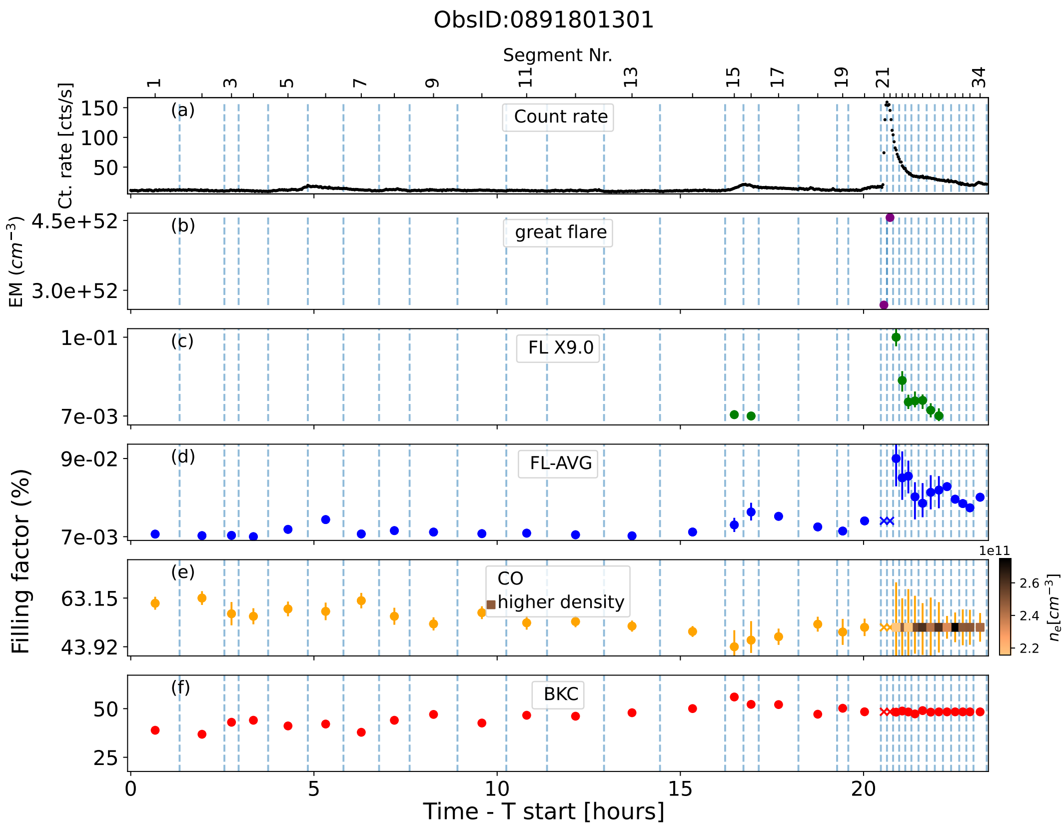

Figure 5.8: Filling factor and density evolution for AD Leo observation 0891801301 using Solution 2. Top panel: X-ray count rate (light curve). Second panel (purple scatter points): Emission measure evolution of VAPEC components demonstrating the need for super-hot components during flaring. Bottom four panels show filling factor evolution (top to bottom): FLX9, FL-AVG, CO, and BKC. Unlike Solution 1, this solution allows $Norm_{\text{reg}}$ to evolve freely throughout the observation. Flare filling factors are derived using refined loop densities. Core filling factors are fixed to the pre-flare mean for post-flare segments (23–34), with the observed norm increase attributed instead to elevated core electron density ($n_{e,\text{CO}}$ increasing from 2.2×10^{11} to 2.8×10^{11} cm^{-3}), consistent with mass injection from the November 2021 Great Flare. High-energy residuals remain and are interpreted as missing EMD bins. A zoom-in view of problematic segments is shown in Fig. A.5.

5.9 | Comparison of solutions

Both solutions successfully address the problems identified in the initial SaXS-only analysis—poor fits during the November 2021 Great Flare peak, systematic high-energy residuals, and sudden jumps in filling factors—but differ in their physical interpretation and modeling approach.

5.9.1 | Common features

Several results are consistent across both solutions:

The background corona (BKC) shows filling factors of 25–50%, derived as the residual coverage after accounting for all other coronal components. This component is not directly constrained by spectral fits due to its weak emission but is essential for ensuring complete spatial coverage.

Core regions (CO) exhibit filling factors of 40–80%, typically around 60% during non-problematic segments. Cores dominate the X-ray emission throughout the observation, consistent with AD Leo's high magnetic activity level.

Active regions (AR) are systematically not selected in the best fits. This suggests either AD Leo's corona was dominated by very hot core structures with few intermediate-temperature active regions, or the solar AR template does not adequately represent stellar active regions on M dwarfs.

After density refinement to enforce physical constraints, baseline flare filling factors (FL-AVG) are approximately 7×10^{-3}%.

Both solutions handle segments 21-22 (November 2021 Great Flare peak) identically, requiring frozen baseline components plus VAPEC models reaching several keV to capture the extreme emission.

5.9.2 | Key differences

Solution 1 (Frozen baseline + VAPEC) treats problematic segments by freezing baseline components (BKC, CO, FL-AVG) and adding high-temperature VAPEC components. This provides a conservative estimate of stable coronal structure by isolating transient super-hot emission. The FLX9 component is not required once VAPEC components are added, confirming it was artificially selected to compensate for missing high-temperature emission.

Solution 2 (Physical restructuring) allows SaXS models to capture temporal evolution, interpreting observed changes as potentially real physical phenomena including post-flare arcade flares and mass injection. Core densities show post-flare elevation. The presence of FLX9 and elevated filling factors may represent real physical changes rather than purely fitting artifacts.

5.9.3 | Implications

The model frameworks differ substantially: Solution 1 acknowledges that solar EMDs do not extend to AD Leo's temperature regime and supplements with VAPEC, whereas Solution 2 suggests the SaXS framework may remain valid if EMD restrictions are relaxed or the library is extended.

The physical processes emphasized also diverge: Solution 1 emphasizes missing super-solar temperatures, while Solution 2 emphasizes post-flare dynamics including arcade flares, mass injection, and density enhancement.

Distinguishing between solutions requires independent constraints: spatially resolved observations (currently impossible for AD Leo), density diagnostics from emission line ratios in high-resolution spectra, or multi-wavelength observations during flare evolution.

Both solutions remain physically plausible given current observational constraints. The choice between them depends on whether one prioritizes conservative interpretation (Solution 1) or exploration of post-flare coronal dynamics (Solution 2).

5.10 | Discussion: AD Leo Results

Having presented two alternative solutions for characterizing AD Leo's corona during the November 2021 Great Flare observation, I now discuss several methodological issues and physical insights that emerged from this analysis. These considerations are important for interpreting the results and for applying the SaXS method to other active stars.

5.10.1 | Absence of AR model in fits

AD Leo spectral fits are dominated by core (CO) and flare region emission throughout the observation, with AR model never being required. The BKC component is required for complete spatial coverage but, as discussed below, is poorly constrained and does not dominate the emission. Several explanations for the AR absence are possible. Physically, AD Leo may have been covered primarily by very hot, bright active region cores at the time of observation, with few intermediate-temperature AR structures. Alternatively, this could reflect a model limitation where the AR EMD does not accurately represent active regions on AD Leo, meaning the solar AR template may be inadequate. A third possibility is a compensation effect where the BKC plus CO combination artificially compensates for emission from a "true" stellar AR component not yet properly constrained.

The solar validation provides an instructive lesson. It showed that low-emitting regions (BKC) are poorly constrained while high-emitting regions (AR, CO, FL) are well constrained. For AD Leo, I find a different pattern: BKC is always present but still poorly constrained (as discussed below), while the higher-emitting AR is systematically absent. This is not a contradiction—BKC improves fits marginally (as seen in the solar validation where one DAXSS observation benefited from BKC inclusion), but remains poorly constrained in both solar and stellar applications. The systematic absence of AR, however, suggests model inadequacy rather than mere constraint issues. This raises the possibility that stellar active regions on M dwarfs may have fundamentally different thermal structure (hotter, denser, different emission measure distribution) than solar analogs.

5.10.2 | Density constraints and degeneracies

Electron density is a critical parameter that is highly degenerate with filling factor for fixed emission measure: $\mathrm{EM} = n_e^2 V \propto n_e^2 f$. Literature-derived densities, extrapolated from measurements at lower temperatures, yielded unphysically small flare filling factors that were smaller than the projected area of a single coronal loop. The problems with these flare densities are twofold. First, initial estimates ($n_e \sim 10^{12}$ to 10^{13} cm^{-3}) lie outside the temperature range where densities were actually measured, making extrapolation to super-solar temperatures unreliable. Second, the measured densities themselves have large uncertainties, sometimes spanning two orders of magnitude, which propagate into highly uncertain filling factor estimates.

Our density refinement approach enforced the physical constraint $f_{\text{flare}} \geq f_{1,\text{loop}}$ (filling factor must exceed the single-loop lower limit) and adjusted densities downward until the constraint was satisfied. I acknowledge a circular reasoning caveat: this assumes SaXS models correctly predict flare emission, assumes flares exist on AD Leo at the time of observation, and derives density by requiring physically sensible filling factors. Our conservative interpretation is that refined densities provide a lower limit on flare filling factors but rely on multiple assumptions about model validity and stellar coronal structure. Future work should prioritize independent density measurements from density-sensitive line ratios in high-resolution spectra, which are critical for breaking the degeneracy and validating filling factor estimates.

5.10.3 | Background corona filling factor

The BKC filling factor is not reliably constrained from spectral fit normalizations alone. The reason is that BKC emits comparatively little relative to other regions, so the spectral fit is primarily sensitive to brighter components (AR, CO, FL). The same problem occurred in solar validation, where the BKC model was present but its normalization was poorly constrained.

Our deductive approach infers the BKC filling factor from other regions assuming total coverage: $f_{\text{BKC}} = 1 - (f_{\text{AR}} + f_{\text{CO}} + f_{\text{FL}})$. The limitation is that this method confirms the presence of BKC-like emission but cannot independently determine its spatial extent from the spectral fit alone.

Improved low-temperature X-ray coverage (below 0.3 keV, where BKC dominates) would improve BKC constraints, but this is difficult for faint stellar sources where emission is dominated by energetic events.

5.10.4 | Super-solar temperatures and model limitations

The AD Leo November 2021 Great Flare exhibits systematic high-energy residuals that require temperatures significantly exceeding any solar analog (several keV versus approximately 2.6 keV for the solar X9.0 flare). This represents a fundamental challenge: the solar EMD library does not extend to the temperature regimes observed on highly active M dwarfs. The addition of high-temperature VAPEC components successfully captures this super-hot emission, but this represents a departure from the pure SaXS approach and introduces additional assumptions about the thermal structure of stellar superflares.

6

Discussion, Conclusions, and Future Directions

6.1 | Summary of contributions

This work advances the SaXS methodology through three main contributions. First, I constructed a new spectral model library by creating XSPEC spectral models directly from solar EMDs (*Yohkoh*/SXT EMDs) for four coronal region types: background corona (BKC), active regions (AR), cores of active regions (CO), and flares (FL). The methodological innovation is that these models retrieve filling factors directly from spectral fit normalizations, eliminating the indirect synthetic parameter-space matching used in previous SaXS implementations.

Second, I conducted the first validation of SaXS-derived filling factors against spatially resolved imaging. By comparing filling factors from DAXSS full-disk solar soft X-ray spectra against contemporaneous *Hinode*/XRT images, I demonstrated that spectral fits successfully reproduce the observed spatial distribution of coronal structures on the Sun. This validation at two solar activity levels (quiescent and flaring) establishes the method's reliability for the first time through direct comparison with imaging.

Third, I applied the validated methodology to *XMM-Newton* EPIC/pn observations of AD Leo, extending SaXS beyond the Sun to characterize an active M dwarf's corona. The analysis revealed persistent flaring activity throughout the observation, with core regions (CO) dominating emission at filling factors of 40–80%. Active regions (AR) were systematically not selected, suggesting AD Leo's corona differs fundamentally from solar structure. Systematic high-energy residuals above 2–3 keV indicated plasma hotter than the most energetic solar flare in our library (X9.0 class flares). To address unphysically low filling factors resulting from uncertain density extrapolations, I developed an iterative density refinement methodology that enforces the geometric constraint that flare filling factors must exceed the projected area of a single coronal loop. I explored two interpretations of the problematic segments: Solution 1 adds high-temperature VAPEC components to capture super-solar flare temperatures, eliminating residuals; Solution 2 interprets temporal variations as real post-flare coronal restructuring, with residuals attributed to overly restricted EMDs rather than fundamentally different physics.

6.2 | Lessons learned and methodological improvements

6.2.1 | EMD restrictions and binning

Our empirical EMD restriction approach—retaining only bins within one order of magnitude of peak emission measure—was validated using only two DAXSS spectra (quiescent and flaring Sun). While this provided initial proof-of-concept, the limited sample size means the restriction criteria may not be robust across the full range of solar conditions, much less stellar environments.

What is required is systematic validation using a large DAXSS spectral archive spanning diverse activity levels. Such a study would determine statistically which EMD bins are essential for accurately reproducing observed spectra and which contribute primarily noise or unreliable measurements. The goal is to establish validated EMD binning and restriction criteria that can be applied confidently across different observational conditions, moving from our current ad hoc approach based on two spectra to statistically grounded methodology based on hundreds of solar observations.

6.2.2 | Limitations of the current EMD library

The current SaXS model library relies on EMDs derived from *Yohkoh*/SXT observations spanning September 1991 through December 2001. While groundbreaking for their time, these observations were limited by spatial resolution (2.5 arcsec per pixel) and a restricted set of filter combinations (5 analysis filters). The EMD library itself, derived by Orlando et al. (2001, 2004) and Reale et al. (2001), draws from a relatively small sample: 23 synoptic images, 78 single-AR observations, and 8 flares. Because these observations represent specific solar cycle phases rather than comprehensive sampling across all kinds of solar conditions and throughout the solar cycle, the resulting EMDs do not capture the full range of coronal variability, particularly for extreme or rare events.

These shortcomings—limited spatial resolution, restricted filter combinations, small sample size, and incomplete solar cycle coverage—motivate the need for an updated EMD library. The limitations encountered in this work, particularly the need for ad hoc EMD restriction and the challenges with AD Leo's super-solar temperatures, further highlight this necessity.

6.3 | Future directions for SaXS development

6.3.1 | Comprehensive solar validation and EMD library expansion

6.3.1.1 | Advantages of *Hinode*/XRT for EMD derivation

Hinode/XRT offers substantial improvements over *Yohkoh*/SXT that directly address the limitations of the current library. The superior spatial resolution (1–2 arcsec compared to *Yohkoh*'s 2.5 arcsec) is valuable because it enables better identification and characterization of small-scale coronal structures, which may have distinct thermal properties from larger features. The expanded filter set (9 analysis filter pairs versus 5) is useful because it provides enhanced temperature diagnostics, allowing more accurate EMD reconstruction across a wider temperature range. Most importantly, the mission's extended operational lifetime—ongoing since 2006 and spanning multiple solar cycles—offers opportunities for comprehensive sampling of solar variability that was not possible with *Yohkoh*'s limited operational period.

The availability of Level 2 synoptic composites 2–4 times daily (when *Hinode* points at Sun center) provides a large data volume for statistical analysis, enabling robust characterization of typical EMD properties and their variability. Critically, the INSPIRESat-1 mission carrying DAXSS has operated contemporaneously with *Hinode* from February 2022 to the present, enabling direct comparison between full-disk soft X-ray spectra and spatially resolved images—the validation approach employed in this work but now scalable to hundreds of observations rather than just two.

6.3.1.2 | Proposed systematic validation workflow

I propose a comprehensive validation approach that would leverage the *Hinode*/DAXSS synergy to systematically refine and validate the SaXS methodology. The workflow consists of interconnected steps:

First, I would derive a large library of *Hinode*/XRT EMDs by extracting EMDs for each coronal region type (BKC, AR, CO, FL) from hundreds of *Hinode* images spanning different activity levels and evolutionary phases. This provides the empirical foundation for understanding EMD variability.

Second, I would match these *Hinode* observations with contemporaneous DAXSS spectra (within minutes to hours), creating paired datasets where the true spatial coronal structure is known from imaging.

Third, I would test the EMD-to-spectrum mapping and refine EMD restrictions simultaneously by systematically evaluating how well each *Hinode*-derived EMD reproduces its corresponding DAXSS spectrum. This would identify which EMD temperature bins and emission measure ranges are essential for accurate spectral reproduction and which can be safely excluded, determining optimal temperature binning based on this large statistical sample rather than the two spectra tested in this work.

Fourth, closely related to the first step, I would characterize EMD variability by quantifying how EMDs for each region type vary with activity level, flare state, and solar cycle phase, establishing the intrinsic range of coronal structure diversity within each region classification.

This systematic validation directly addresses the methodological improvements identified in Section 6, providing statistically robust EMD restrictions and a comprehensive library spanning the full range of solar conditions.

6.3.2 | Applicability to different stellar types

6.3.2.1 | Conditions favoring SaXS application

The SaXS method is likely to be most reliable when applied to stellar targets that closely resemble the Sun, minimizing uncertainties in the assumptions underlying the solar-derived EMD templates. Solar analogs might provide the closest match to solar EMD templates and allow us to reasonably assume solar-like abundances and densities, though this remains to be empirically tested. For stars with independently measured abundances and densities from high-resolution spectroscopy (Chandra HETGS, *XMM-Newton* RGS), the SaXS method can incorporate these as fixed inputs, eliminating major sources of uncertainty. Bright X-ray sources are particularly favorable because their high count rates enable precise spectral fitting with sufficient signal-to-noise ratio to reliably distinguish between multiple coronal region components.

6.3.2.2 | Challenges for specific stellar types

While solar-like targets offer the most promising applications, the method faces significant challenges for certain stellar types. Very active stars such as M dwarfs present multiple difficulties: their coronal structures may be fundamentally different from solar analogs (as demonstrated by AD Leo's absence of AR components), and their super-solar temperatures require extrapolation beyond the available EMD library into untested parameter space. Faint sources present a different challenge—low count rates limit spectral diagnostics, making it difficult to constrain multiple region components simultaneously when signals are weak. Stars with unknown coronal abundances are also problematic, creating a dilemma: free abundances introduce too many parameters for robust fitting, while fixed solar abundances may be physically inappropriate for stars with different chemical compositions or FIP effects.

6.3.2.3 | Systematic failures as diagnostics

Rather than viewing systematic failures as simply limitations, I recognize their diagnostic value for understanding stellar coronal diversity. High-energy failures, such as those observed in the AD Leo November 2021 Great Flare where SaXS models systematically fail above approximately 2–3 keV, directly indicate plasma hotter than any solar analog. These residuals reveal precisely where solar templates are inadequate, identifying either the need for an extended EMD library covering higher temperature regimes or fundamentally different coronal structures that cannot be described by solar analogs.

This diagnostic capability enables population-level studies by applying the method systematically to large stellar samples. For example, applying SaXS to existing stellar spectra from *XMM-Newton* and Chandra, as well as the eROSITA all-sky survey, would map where solar-derived models succeed versus fail across the HR diagram. This mapping enables characterization by coronal region types, creating a coronal HR diagram where stars are characterized not only by traditional parameters (T_{eff}, L) but also by their filling factors $(f_{\mathrm{BKC}}, f_{\mathrm{AR}}, f_{\mathrm{CO}}, f_{\mathrm{FL}})$. The resulting patterns would reveal how magnetic activity manifests differently across stellar populations and guide development of extended model libraries tailored to different stellar types.

6.3.3 | Extending SaXS to stellar populations

6.3.3.1 | Initial applications to solar-type stars

I recommend prioritizing solar analogs for initial stellar applications—stars with similar T_{eff}, $\log g$, and rotation periods to the Sun. This approach minimizes uncertainties from abundances and densities while providing the clearest test of whether the SaXS framework extends beyond the Sun itself. By comparing derived filling factors to solar observations at similar activity levels, I can quantify whether other solar-type stars exhibit similar coronal structure distributions or show systematic deviations that reveal physically interesting differences. Deviations would be scientifically valuable, revealing either interesting physical differences or identifying where our assumptions break down.

Repeated observations over years to decades offer additional scientific value by tracing filling factor evolution through stellar activity cycles. This would provide a stellar analog to the well-studied solar cycle, but characterized in terms of physical coronal structure changes (varying coverage of BKC, AR, CO, FL) rather than purely phenomenological metrics like X-ray luminosity.

6.3.3.2 | Density-constrained targets

Electron density and filling factor are fundamentally degenerate for fixed emission measure, as demonstrated by the AD Leo analysis. I should prioritize bright X-ray sources where high-resolution spectroscopy has measured electron densities from density-sensitive emission line ratios. For these density-constrained targets, fixing n_e eliminates the degeneracy and enables unambiguous filling factor determination. This staged approach builds confidence systematically: first validate with well-constrained systems, then carefully extend to less constrained cases.

6.3.3.3 | Rotation period from filling factor modulation

Coronal active regions should produce X-ray rotational modulation analogous to optical rotational modulation from starspots. If active regions are concentrated in longitude rather than uniformly distributed, filling factors (especially AR and CO) should vary periodically as the star rotates, with maximum X-ray emission when the active longitude faces the observer. Monitoring filling factor variability over time periods longer than the expected rotation period would reveal this periodicity, enabling rotation period determination from X-ray data alone.

This approach offers advantages over simple L_X monitoring because filling factors reveal which coronal components modulate, providing physical insight into magnetic region distribution on the stellar surface. Correlating X-ray filling factor modulation with optical starspot amplitude would create a comprehensive picture of how magnetic activity manifests from the photosphere through the corona. The combined measurements distinguish between stars with localized active regions (strong modulation in both optical and X-ray) versus stars with more uniform magnetic field distributions (weak modulation despite high activity levels).

6.3.3.4 | Multi-wavelength synergy

Complementary observations can combine X-ray filling factors with optical photometry (starspots), chromospheric emission (Hα, Ca II), and photospheric magnetograms (when available) for a comprehensive activity portrait. In the exoplanet context, filling factors for stars with known exoplanets constrain the magnetic environment and potential for atmospheric erosion via CMEs and high-energy radiation.

6.3.4 | Theoretical extensions and model development

6.3.4.1 | Empirical extrapolation to super-solar temperatures

The EMDs of successive coronal region types (BKC, AR, CO, FL) show systematic progression toward higher temperatures and emission measures, suggesting an underlying physical continuity in heating mechanisms. The same fundamental processes—magnetic reconnection and chromospheric evaporation—operate across all region types, with differences in intensity and frequency producing the observed EMD shape evolution.

This systematic progression motivates an empirical extrapolation approach: fitting functional forms to EMD shape evolution across the existing solar region types, then extrapolating these functions to higher temperatures to create synthetic "super-flare" EMDs representing structures not observed on the Sun but potentially existing on highly active stars. This extrapolation would extend the SaXS model library to cover temperature regimes up to approximately 100 MK, bridging the gap between solar flares (10 MK) and stellar superflares. Such an extended library would enable SaXS modeling of highly active stars (young

M dwarfs, RS CVn binaries) that exhibit temperatures well beyond the solar regime.

6.3.4.2 | Physical origin of EMD shapes

A fundamental question motivates deeper theoretical development: why do coronal regions produce EMDs with these particular shapes, and what physical processes determine the temperature distribution of confined plasma? Currently, I treat EMDs as empirical templates derived from observations, but a complete physical understanding would predict EMD shapes from first principles.

EMD shape reflects the balance between competing physical processes. Heating mechanisms (magnetic reconnection, wave dissipation) inject energy at varying rates along coronal loops. Cooling mechanisms (radiation, thermal conduction) remove energy, with rates depending strongly on density and temperature. The magnetic field geometry and gravitational stratification determine how plasma distributes itself along field lines, creating temperature structure. These processes interact to produce the characteristic EMD for each region type.

Our long-term goal is to derive a mathematical and physical framework that relates fundamental stellar parameters (rotation rate, magnetic flux emergence rate, convection properties) to predicted EMD shapes for coronal regions. The ultimate vision is predictive modeling: given a star's properties alone, I could predict what type of coronal structures should exist on that star, enabling forward modeling of stellar coronae from fundamental stellar physics rather than relying on empirical solar templates.

6.4 | SaXS as a physics-based activity diagnostic

Current stellar activity metrics such as L_X/L_{bol} and rotation period are fundamentally empirical correlations—they quantify activity levels but provide limited physical insight into the underlying magnetic structures. SaXS goes beyond this phenomenology by characterizing activity in terms of actual coronal magnetic regions with distinct physical properties. Filling factors reveal not just "how active" a star is but "what kind of activity" dominates its corona: whether emission comes primarily from steady active regions or transient flares, whether the corona is dominated by hot cores or cooler background plasma.

This physical characterization enables comparative stellar physics through a unified framework connecting solar and stellar observations. For the first time, I can directly compare solar magnetic activity and stellar magnetic activity using the same coronal region classifications, bridging the gap between spatially resolved solar physics and unresolved stellar astrophysics. The predictive power derives from understanding which stars host which types of coronal structures: a star dominated by core emission faces different space weather conditions than one dominated by flare emission, even if both have similar L_X/L_{bol} ratios. This enables physics-based predictions about space weather severity, CME rates, and threats to exoplanetary atmospheres that go beyond what integrated luminosity alone can provide.

6.5 | Concluding remarks

This work demonstrates both the promise and the limitations of applying solar coronal structure as a template for understanding stellar coronae. The successful solar validation shows that filling factors can be reliably derived from spectral fits and independently verified through imaging. The AD Leo application reveals where the solar analogy breaks down—super-solar temperatures, uncertain density extrapolations, and potentially different coronal region distributions—while showing that even these "failures" provide valuable physical insights.

The method's power lies in its physics-based approach. Rather than characterizing activity purely through integrated quantities like L_X/L_{bol}, SaXS describes coronae in terms of actual magnetic structures with distinct temperatures, densities, and spatial coverage. This physical characterization is most reliable for solar-type stars or stars with independently measured abundances and densities, where assumptions underlying the solar-derived templates are most justified.

Looking forward, systematic refinement of the EMD library using *Hinode* observations and validation against the large DAXSS archive will strengthen the method's empirical foundation. Extension to larger stellar samples will map the full range of coronal structure diversity across the HR diagram, revealing where solar templates succeed and where new physical frameworks are needed. Ultimately, SaXS offers a path toward understanding stellar coronae as physical systems rather than phenomenological constructs, bringing stellar X-ray astronomy closer to the physical understanding achieved in spatially resolved solar physics—while maintaining appropriate skepticism about where and when the solar analogy applies.

A

Additional Figures

This appendix contains supplementary figures referenced in the main text.

A.1 | Enhanced view of faint coronal structures

Figure A.1 shows the *Hinode*/XRT image corresponding to the Flaring Sun DAXSS observation with adjusted colorbar limits. This enhanced view improves visibility of faint coronal structures that are subdued by the bright flare emission in the standard display (Fig. 4.2, bottom panel). The colorbar adjustment reveals the underlying coronal structure, including diffuse emission and fainter active region loops, that would otherwise be saturated by the intense flare brightness.

A.2 | Zoom-in to flaring region

Figure A.2 provides a detailed view of the flaring regions from the Flaring Sun observation (2022 April 25), complementing the full-disk image in Section 4.9. Pixels are color-coded by coronal region type (AR: green, CO: orange, FL: blue) with filling factors derived from variable abundance spectral fits (Section 4.8). Overlaid contours show active regions (black) and bright points (red) from the *Hinode*/XRT segmentation database (Adithya et al., 2021), while bounding boxes indicate flares (black) and active regions (blue) cataloged in the Heliophysics Event Knowledgebase (Hurlburt et al., 2012). The zoom en-

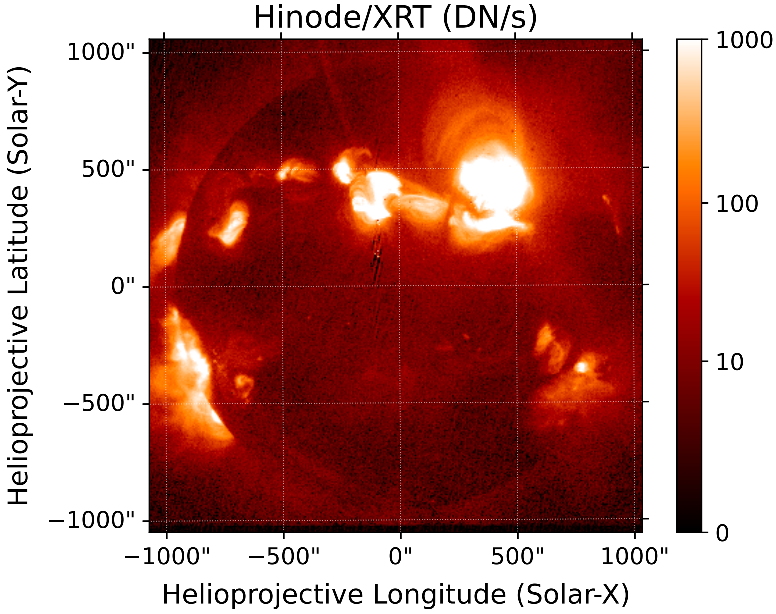

Figure A.1: *Hinode*/XRT image corresponding to the Flaring Sun DAXSS observation. The colorbar limits are adjusted to enhance visibility of coronal structures that are faint relative to the ongoing flares.

ables closer examination of how spectrally derived components correspond to imaging-based identifications.

A.3 | AD Leo filling factor evolution: zoom-in views

This section provides zoomed-in views of the filling factor evolution during problematic segments, corresponding to the full-observation views in the main text. These detailed views focus on the small flare (segments 15-17) and the November 2021 Great Flare region (segments 21-34), where the initial SaXS-only fits exhibited systematic problems and where the two alternative solutions (Solution 1 and Solution 2) differ in their treatment.

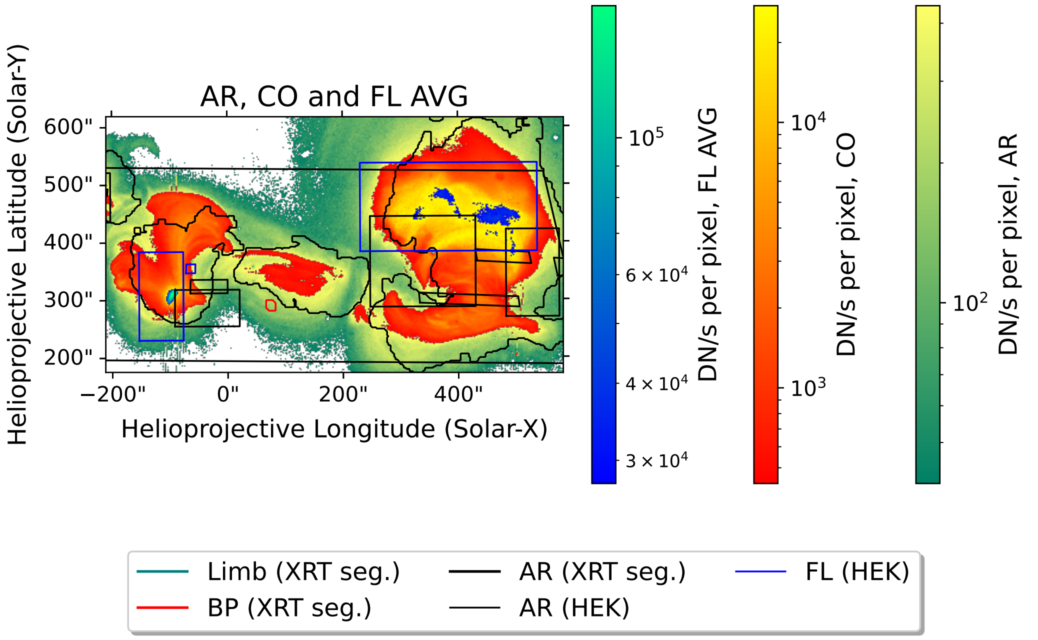

Figure A.2: Zoom-in to flaring regions on the *Hinode*/XRT image taken during the Flaring Sun observation, showing pixels color-coded by coronal regions whose filling factors were determined from spectral fitting with variable abundances and non-equilibrium ionization for flares (see Section 4.8): AR (green), CO (orange), and FL (blue). The filling factors shown correspond to the refined fits using VAPEC and VNEI models. The black and red contours correspond to active regions (AR (XRT seg.)) and bright points (BP (XRT seg.)), respectively, as identified in the *Hinode*/XRT segmentation database. The flares (FL (HEK)) and active regions (AR (HEK)) simultaneously detected by various solar instruments and registered in the public Heliophysics Event Knowledgebase (HEK) are shown as black and blue bounding boxes, respectively.

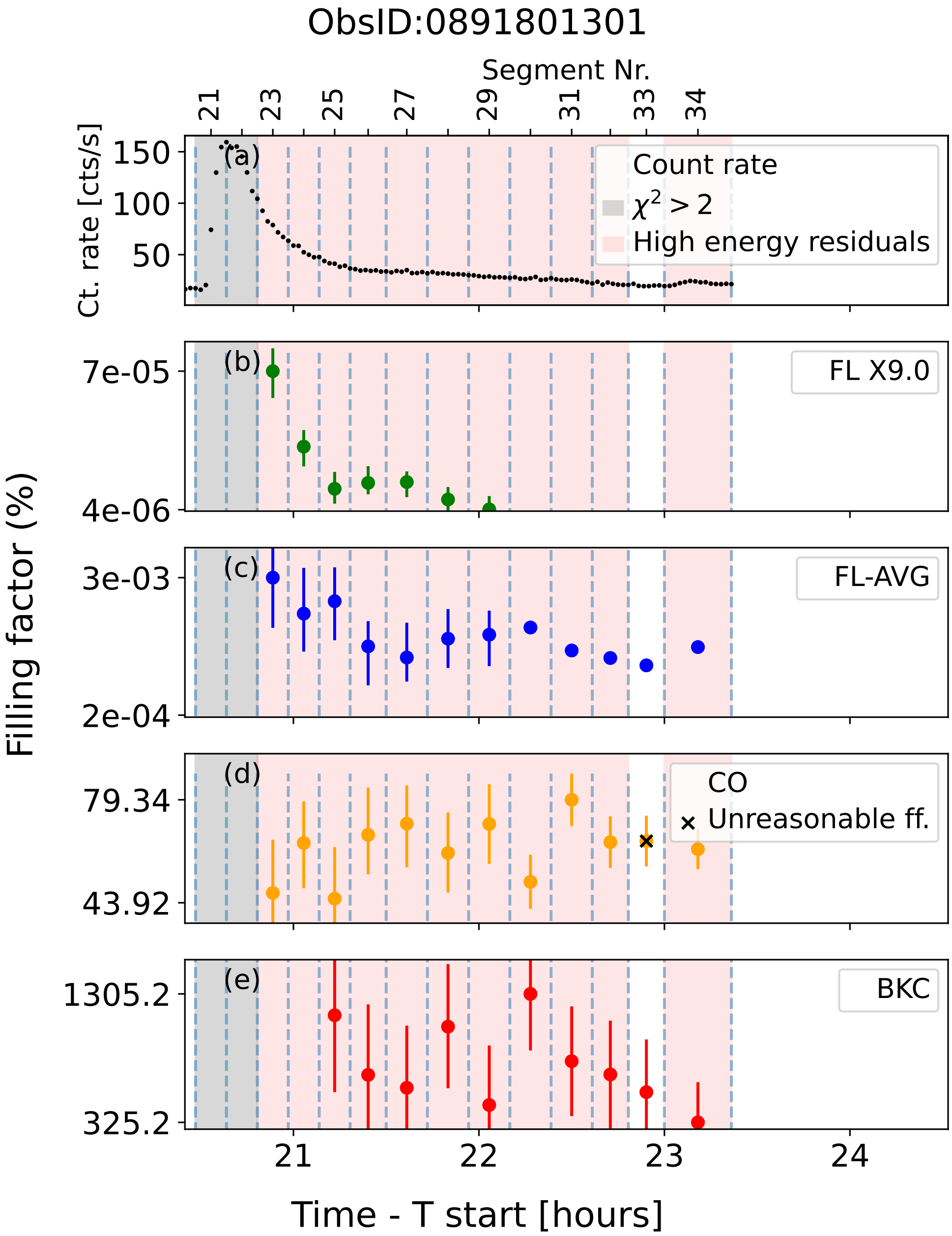

Figure A.3: Zoom-in to November 2021 Great Flare region showing filling factor evolution from initial SaXS-only fits (corresponding to Fig. 5.6). Top panel: X-ray count rate showing flare rise, peak, and decay. Second panel (purple points): Emission measure evolution indicating need for super-hot VAPEC components. Bottom three panels: Filling factor evolution for FL-AVG, CO, and BKC. Gray-shaded segments (21-22, 33) show poor fits or unrealistic filling factors. Pink-shaded segments (23-32, 34) show acceptable χ^2 but systematic high-energy residuals.

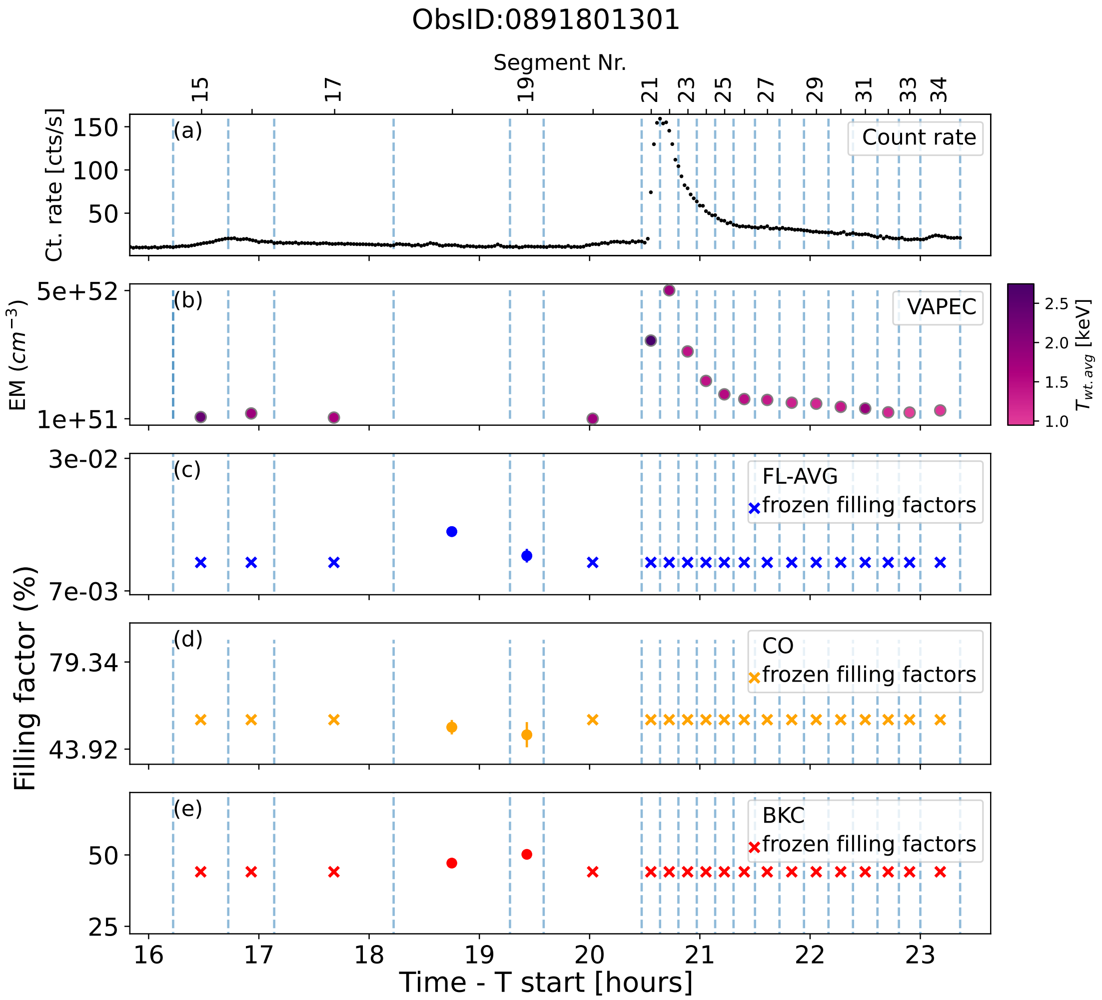

Figure A.4: Zoom-in to November 2021 Great Flare region showing refined filling factor evolution with Solution 1 (corresponding to Fig. 5.7). Top panel: X-ray count rate. Second panel (purple gradient): Emission measure evolution of high-temperature VAPEC components, with color indicating temperature (pink = cooler, dark purple = hottest). The hot component emission measure traces the flare evolution. Bottom three panels: Baseline coronal components (FL-AVG, CO, BKC) frozen to mean values, eliminating artificial inflation of filling factors during flare.

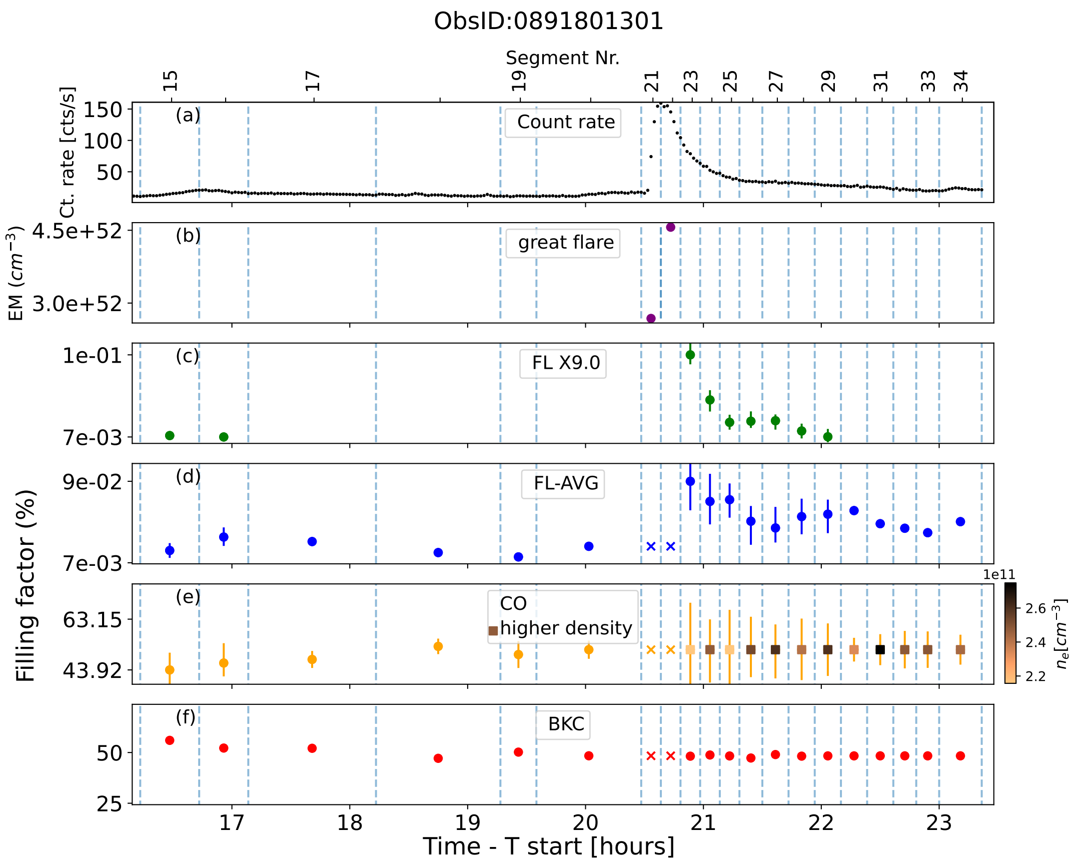

Figure A.5: Zoom-in to problematic segments showing filling factor and density evolution with Solution 2 (corresponding to Fig. 5.8). Top panel: X-ray count rate focusing on the small flares (segments 15-17) and November 2021 Great Flare region (segments 21-34). Second panel (purple scatter points): Emission measure evolution of VAPEC components. Bottom four panels show filling factor evolution (top to bottom): FLX9, FL-AVG, CO, and BKC. For post-flare segments (23-34), core filling factors are frozen while densities vary to capture mass injection effects. The FLX9 component appears throughout problematic segments, potentially representing real physical changes rather than fitting artifacts.

B

Solar Coronal Abundances from DAXSS Spectral Fits

This appendix presents the abundances derived from variable-abundance (VAPEC) fits to the DAXSS solar spectra, as discussed in Section 4.8. The abundances were varied within a 20% range (0.8–1.2) and tied across all region types in each fit to reduce the number of free parameters.

Table B.1: Abundance factors derived from variable-abundance (VAPEC) fits to DAXSS solar spectra, as discussed in Section 4.8. Columns show the element and abundance factors for the Quiescent Sun and Flaring Sun observations. Abundance factors represent multiplicative factors relative to the Feldman Standard Extended Coronal abundances (Feldman, 1992) and were constrained to vary within 20% (0.8–1.2) to reduce free parameters. Abundances were tied across all region types within each fit.

Element	Quiescent Sun Abundance Factors	Flaring Sun Abundance Factors
Mg	1.20 ± 0.55	1.20 ± 0.20
Si	1.20 ± 0.69	1.14 ± 0.07
S	0.80 ± 0.50	0.80 ± 0.10
Ar	1.20 ± 120.57	0.80 ± 0.17
Ca	0.80 ± 365.17	1.20 ± 0.42
Fe	1.20 ± 0.51	1.20 ± 0.17

C

VAPEC Component Parameters for AD Leo

This appendix presents the temperatures and emission measures of the high-temperature VAPEC components added to the SaXS models for problematic segments in AD Leo observation 0891801301, as discussed in Section 5.7. Table C.1 compares the spectral fit quality between the initial SaXS-only fits and the refined VAPEC+SaXS fits for each problematic segment (15–17, 21–34). The dramatic improvement in reduced chi-squared values demonstrates that the addition of super-hot VAPEC components successfully eliminates systematic high-energy residuals.

Table C.1: VAPEC models + SaXS vs. SaXS only fit results for each time segment. kT_1 and kT_2 are the temperatures of the two VAPEC components. EM_1 and EM_2 are the emission measures. T_{avg} is the emission measure-weighted average temperature. χ^2_ν (VAPEC+SaXS) and χ^2_ν (SaXS only) are the reduced chi-squared values for the combined VAPEC+SaXS model and the SaXS-only model, respectively.

Segment	kT_1 [keV]	EM_1 [10^{51} cm^{-3}]	kT_2 [keV]	EM_2 [10^{51} cm^{-3}]	T_{avg} [keV]	χ^2_ν (VAPEC+SaXS)	χ^2_ν (SaXS only)
1							1.84
2							1.63
3							1.31
4							1.27
5							1.88
6							1.82
7							1.36
8							1.50
9							1.43
10							1.50
11							1.50
12							1.59
13							1.83
14							1.53
15	2.40	1.76			2.40	1.12	1.93
16	2.32	2.08	0.73	1.00	1.80	0.95	1.98
17	2.24	0.96	0.72	0.60	1.65	1.12	1.94
18							1.53
19							1.40
20	2.34	0.76	0.68	0.40	1.77	1.16	1.85
21	2.98	26.17	0.94	3.31	2.75	1.08	4.94
22	2.03	37.36	0.81	10.33	1.77	1.20	3.64
23	1.80	16.46	0.76	9.08	1.43	1.06	1.92
24	1.84	9.06	0.78	5.81	1.43	1.19	1.71
25	2.15	5.43	0.80	4.57	1.53	1.00	1.61
26	1.96	4.95	0.76	3.33	1.48	1.00	1.61
27	1.77	4.87	0.70	3.10	1.35	1.19	1.71
28	1.75	3.60	0.75	3.36	1.27	1.15	1.52
29	2.50	1.73	0.75	4.88	1.21	1.03	1.14
30	3.44	1.17	0.78	4.29	1.35	0.99	1.22
31	6.56	1.00	0.66	3.87	1.86	0.99	1.32
32	1.92	1.46	0.70	2.02	1.21	1.12	1.30
33	1.84	0.78	0.68	2.62	0.95	1.03	1.28
34	1.59	1.73	0.68	2.44	1.06	0.93	1.20

D

Spectral Fits for AD Leo Observation 0891801301

This appendix presents spectral fits for AD Leo observation 0891801301 (Nov 18/19, 2021). Section D.1 shows initial fits using solar-derived SaXS models alone for all 34 segments. Section D.2 shows refined fits for problematic segments (15–17, 21–34) that add high-temperature VAPEC components to eliminate systematic high-energy residuals, as discussed in Section 5.7.

D.1 | Initial SaXS-only fits

Spectral fits for all 34 segments using solar-derived SaXS models (BKC, AR, CO, FL-AVG, FLX9). For each segment, the best-fit model combination was selected based on lowest reduced χ^2. Segments 1–14 and 18–20 achieve acceptable fits with SaXS models alone. Segments 15–17 and 21–34 exhibit systematic high-energy residuals above 2–3 keV, motivating the refined analysis in the following section.

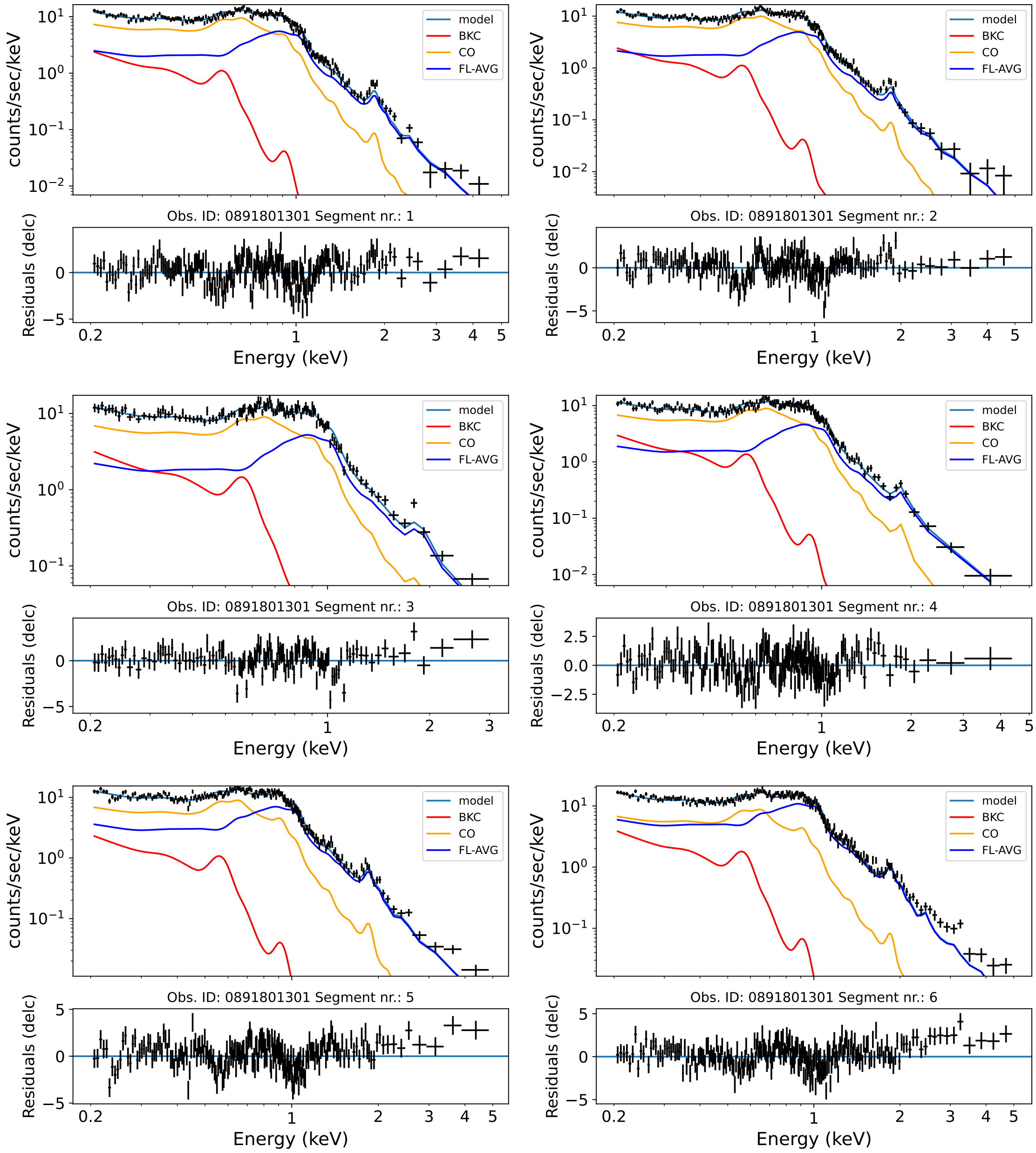

Figure D.1: Initial SaXS-only spectral fits for all 34 segments of AD Leo observation 0891801301. Each panel shows the observed *XMM-Newton* EPIC/pn spectrum (black points with error bars), best-fit SaXS model components (red: BKC, orange: CO, blue: FL-AVG, green: FLX9), total model (solid line), and fit residuals (bottom panel). Segments 1–14 and 18–20 achieve acceptable fits with $\chi^2_{\mathrm{red}} \sim 1$–2. Segments 15–17 and 21–34 show systematic high-energy residuals above 2–3 keV.

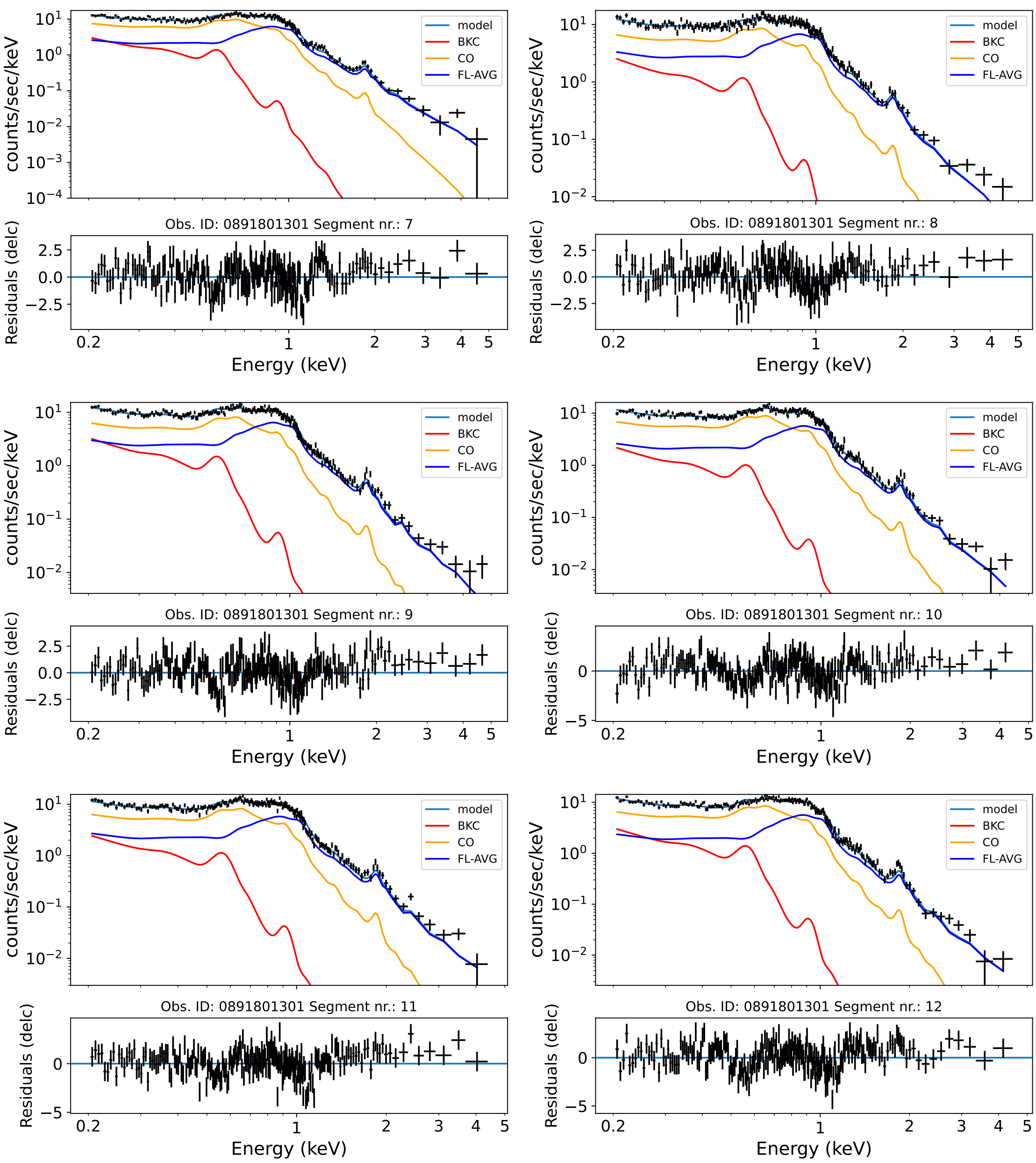

Figure D.1: continued

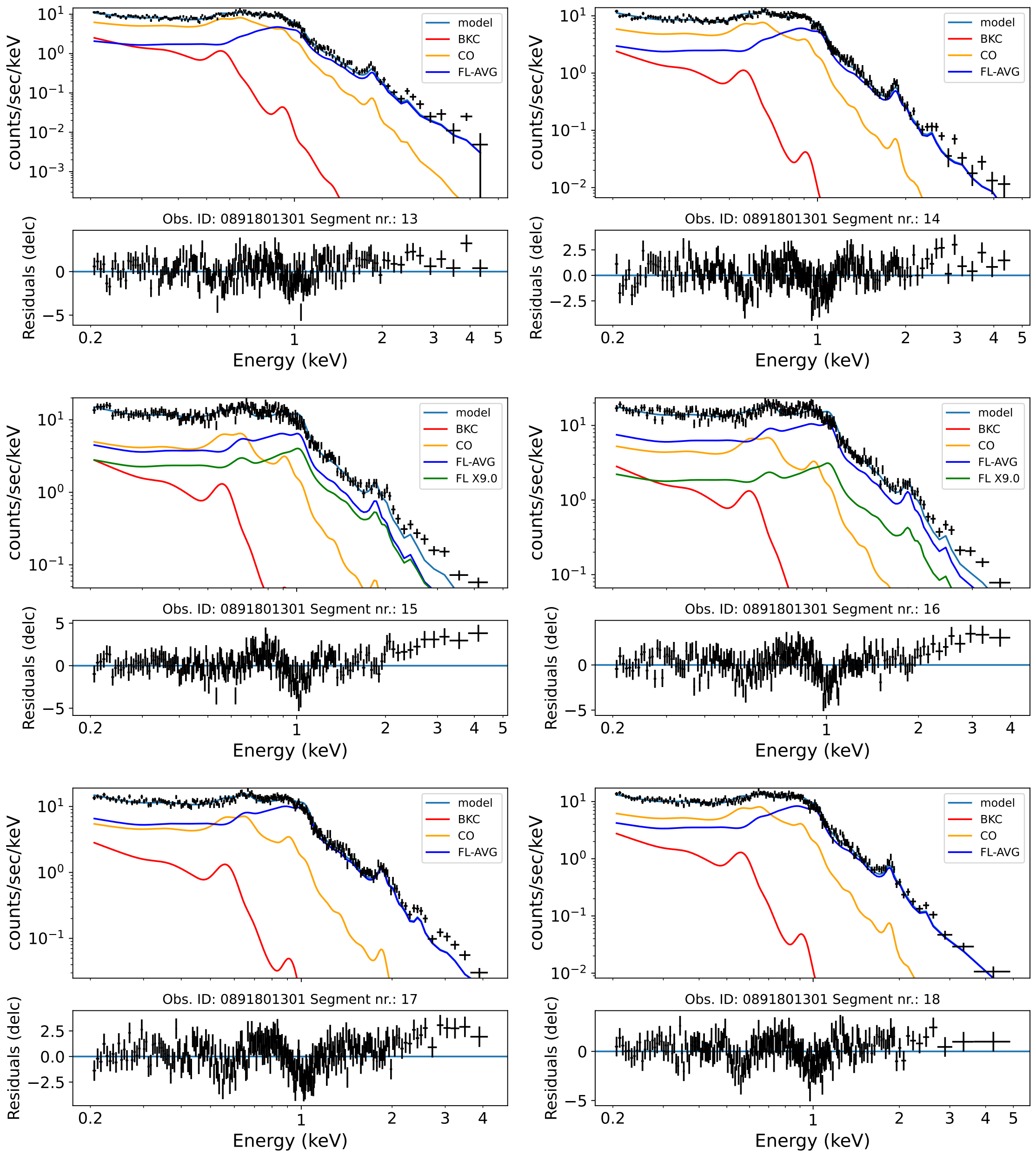

Figure D.1: continued

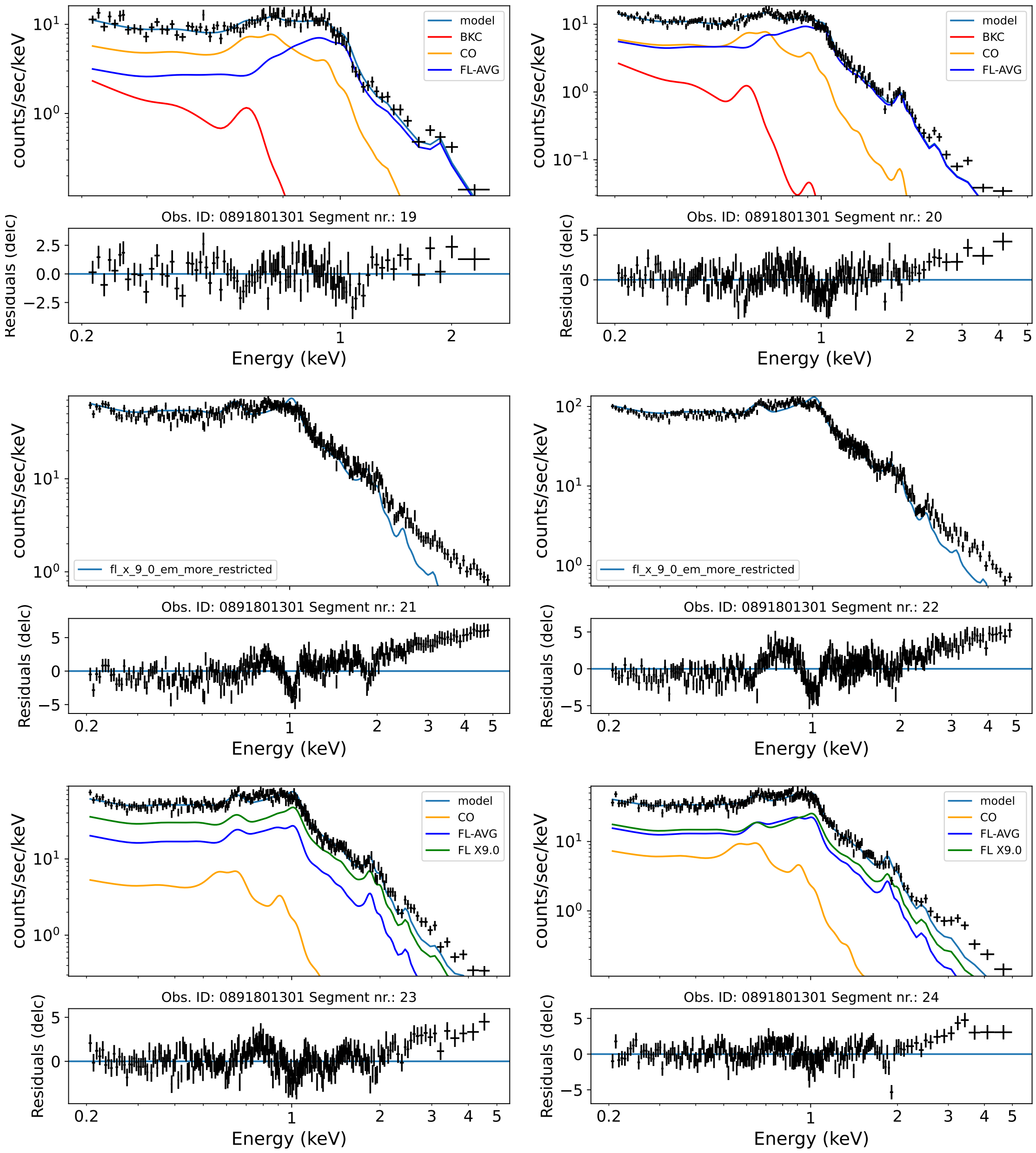

Figure D.1: continued

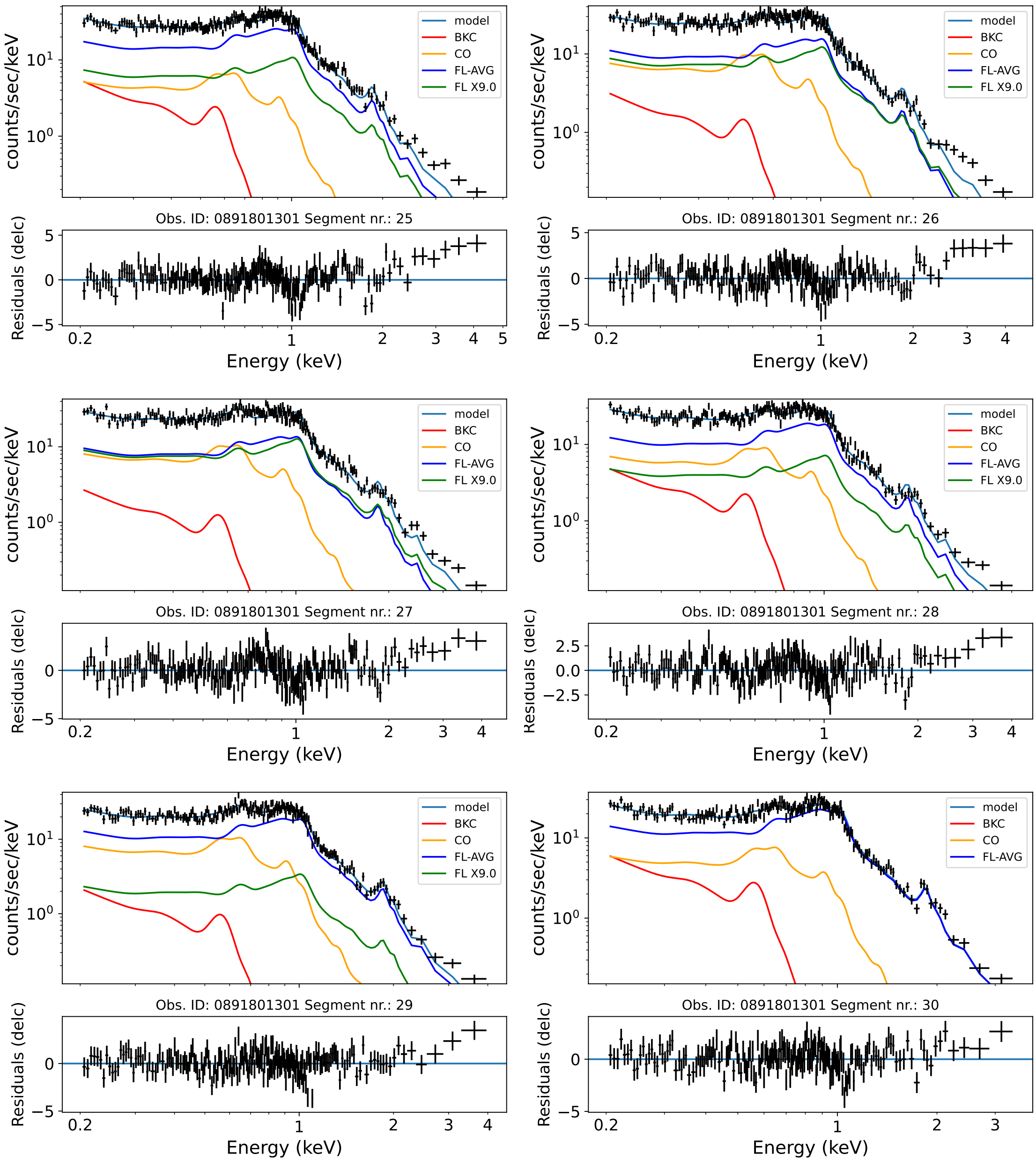

Figure D.1: continued

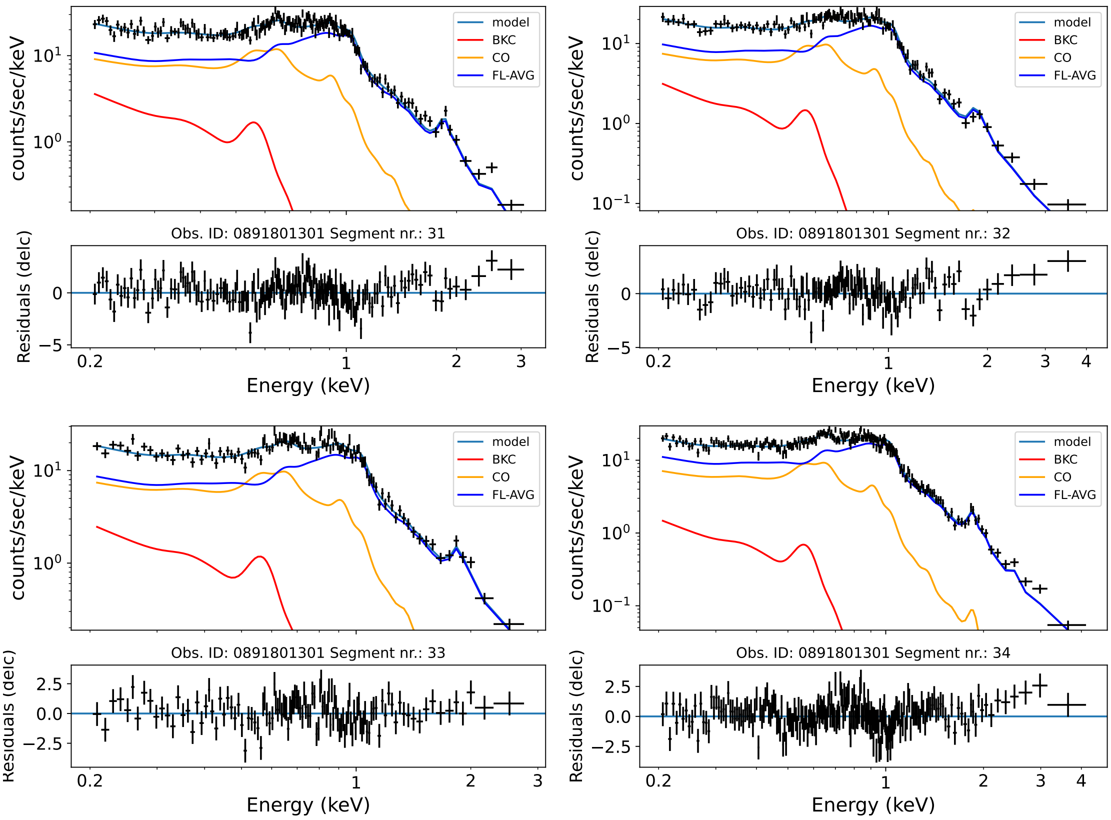

Figure D.1: continued

D.2 | Refined SaXS+VAPEC fits for problematic segments

Spectral fits for segments 15–17 and 21–34 using Solution 1. Baseline SaXS components (BKC, CO, FL-AVG) are frozen to mean values from non-problematic segments. One or two high-temperature VAPEC components are added to capture super-solar flare emission. All refined fits achieve $\chi^2_{\rm red} \lesssim 2$ with VAPEC temperatures ranging from $\sim$1 keV to $>$5 keV.

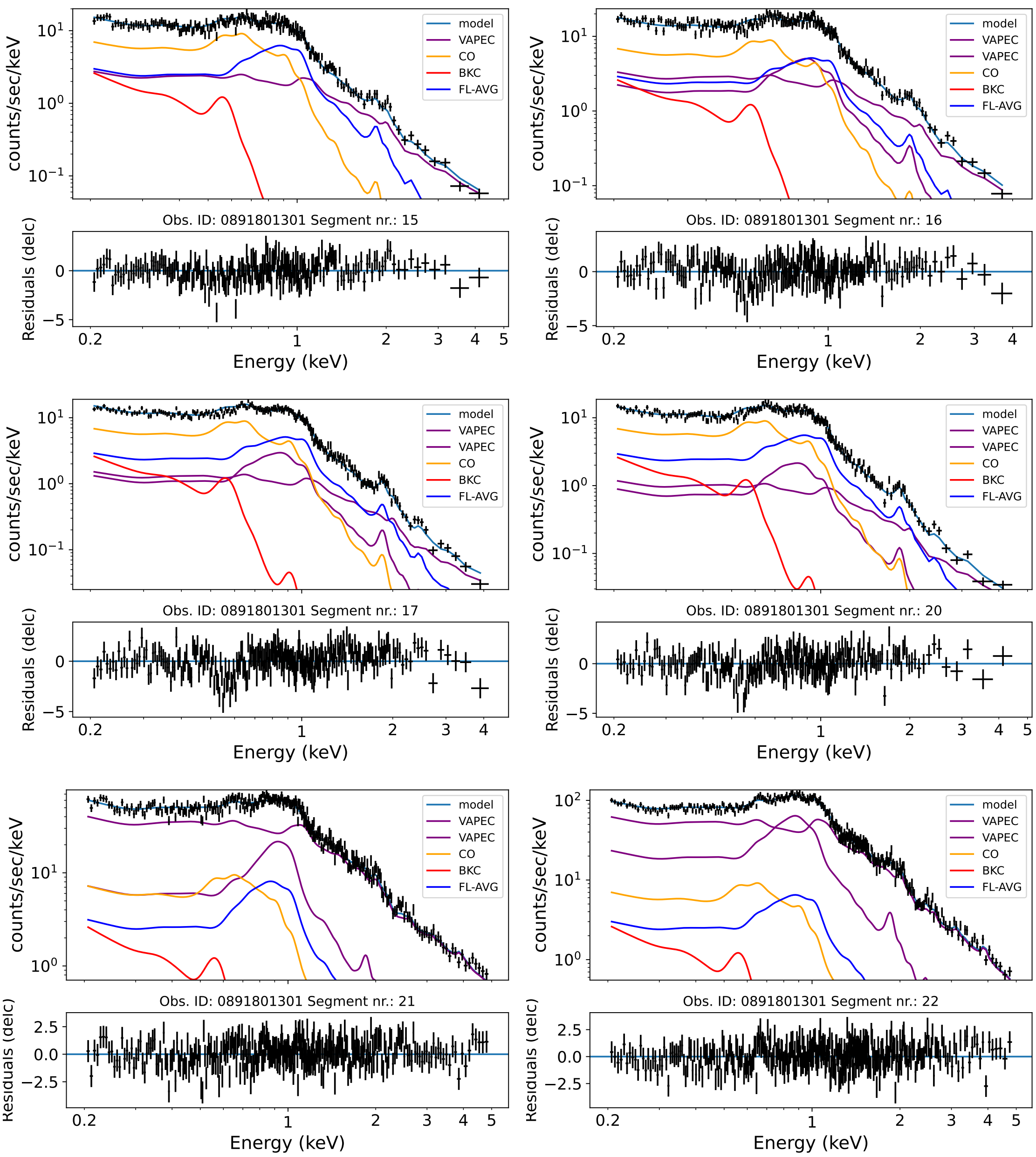

Figure D.2: Refined SaXS+VAPEC spectral fits for problematic segments 15–17 and 21–34. Each panel shows the observed *XMM-Newton* EPIC/pn spectrum (black points with error bars), frozen baseline SaXS components (red: BKC, orange: CO, blue: FL-AVG), additional high-temperature VAPEC components (purple), total model (solid line), and fit residuals (bottom panel). All refined fits achieve $\chi^2_{\mathrm{red}} \sim 1$ with high-energy residuals eliminated.

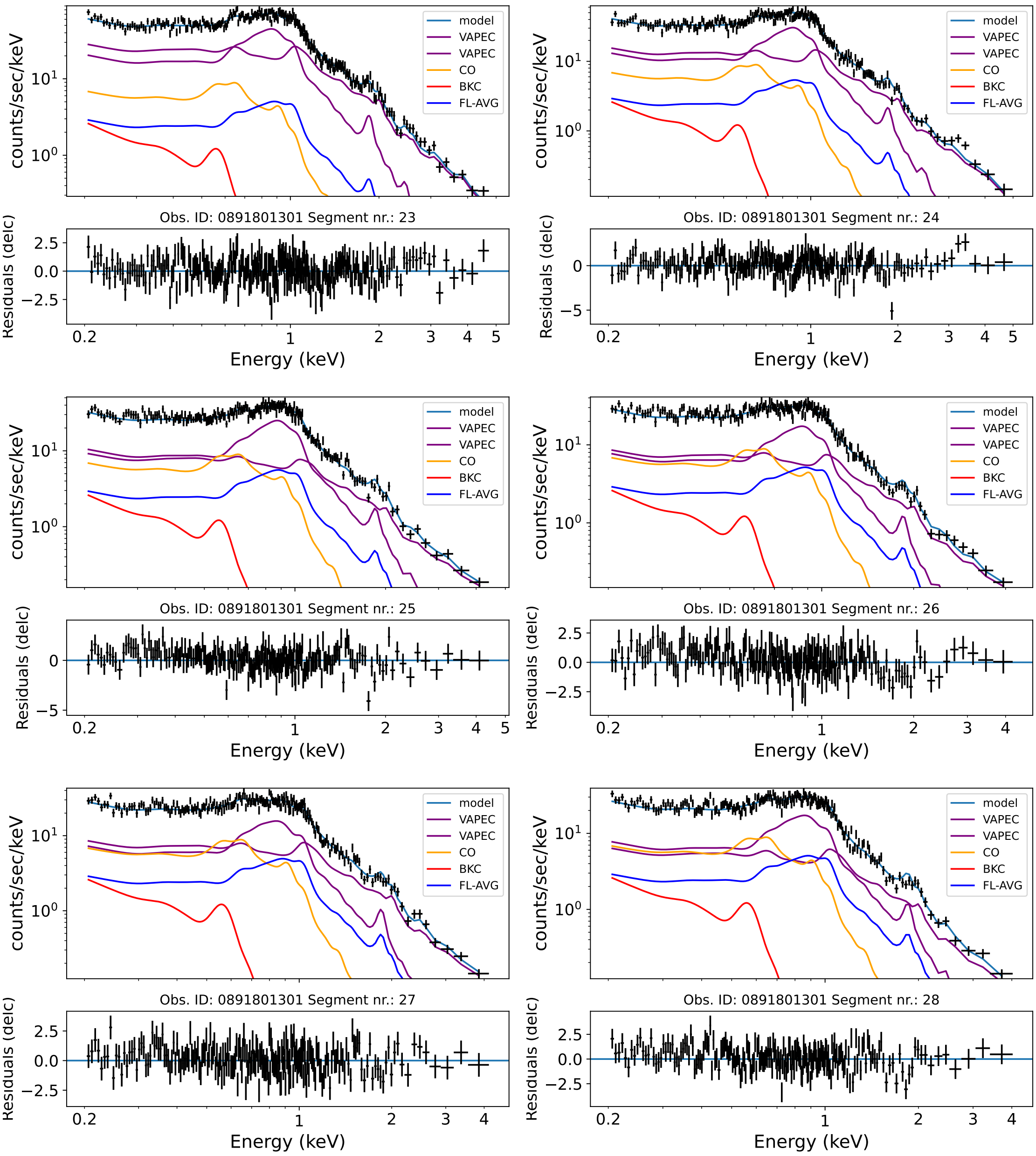

Figure D.2: continued

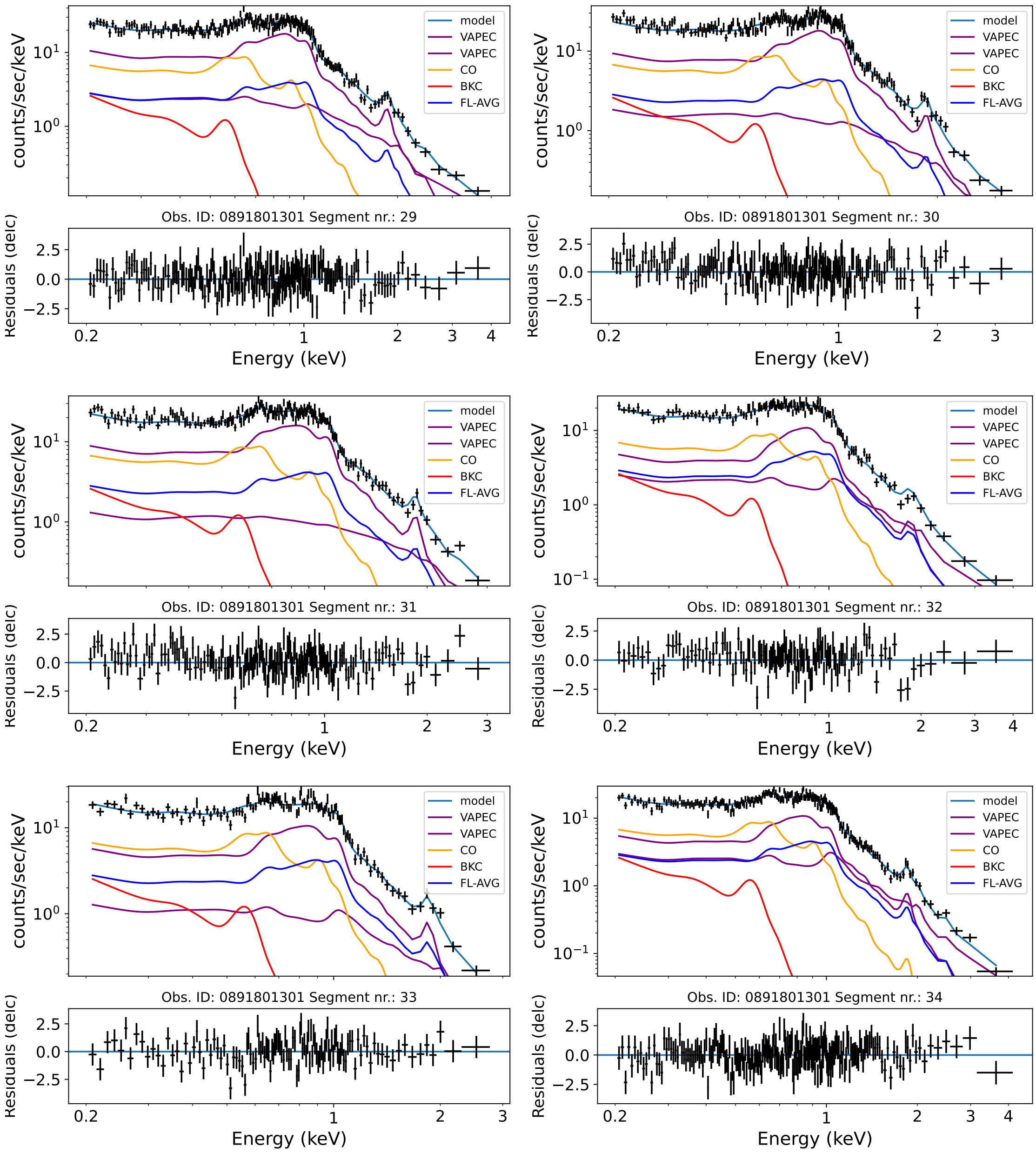

Figure D.2: continued

References

H. N. Adithya, Rangaiah Kariyappa, Imada Shinsuke, Kusano Kanya, Joe Zender, Luc Damé, Giono Gabriel, Edward DeLuca, and Mark Weber. Solar Soft X-ray Irradiance Variability, I: Segmentation of Hinode/XRT Full-Disk Images and Comparison with GOES (1 - 8 Å) X-Ray Flux. *Solar Physics*, 296(4): 71, April 2021. doi: 10.1007/s11207-021-01785-6.

Vladimir S. Airapetian, Alex Glocer, George V. Khazanov, R. O. P. Loyd, Kevin France, Jan Sojka, William C. Danchi, and Michael W. Liemohn. How Hospitable Are Space Weather Affected Habitable Zones? The Role of Ion Escape. *ApJ*, 836(1):L3, February 2017. doi: 10.3847/2041-8213/836/1/L3.

Keith Arnaud, Ben Dorman, and Craig Gordon. XSPEC: An X-ray spectral fitting package. Astrophysics Source Code Library, record ascl:9910.005, October 1999.

Markus J. Aschwanden and Clare E. Parnell. Nanoflare Statistics from First Principles: Fractal Geometry and Temperature Synthesis. *ApJ*, 572(2):1048–1071, June 2002. doi: 10.1086/340385.

Arnold O. Benz. Flare Observations. *Living Reviews in Solar Physics*, 14(1):2, December 2017. doi: 10.1007/s41116-016-0004-3.

D. A. Biesecker, J. M. Ryan, and G. J. Fishman. Observations of small solar flares with batse. In *High-Energy Solar Phenomena – A New Era of Spacecraft Measurements*, volume 294 of *AIP Conference Proceedings*, pages 183–186, 1994.

John J. Bochanski, Suzanne L. Hawley, Kevin R. Covey, Andrew A. West, I. Neill Reid, David A. Golimowski, and Željko Ivezić. The Luminosity and Mass Functions of Low-mass Stars in the Galactic Disk. II. The Field. , 139(6):2679–2699, June 2010. doi: 10.1088/0004-6256/139/6/2679.

S. Bowyer and R. F. Malina. The Extreme Ultraviolet Explorer Mission. In Roger F. Malina and Stuart Bowyer, editors, *Extreme Ultraviolet Astronomy*, page 397, January 1991.

A. C. Brinkman, C. J. T. Gunsing, J. S. Kaastra, R. L. J. van der Meer, R. Mewe, F. Paerels, A. J. J. Raassen, J. J. van Rooijen, H. Bräuninger, W. Burkert, V. Burwitz, G. Hartner, P. Predehl, J.-U. Ness, J. H. M. M. Schmitt, J. J. Drake, O. Johnson, M. Juda, V. Kashyap, S. S. Murray, D. Pease, P. Ratzlaff, and B. J. Wargelin. First Light Measurements of Capella with the Low-Energy Transmission Grating Spectrometer aboard the Chandra X-Ray Observatory. *ApJ*, 530(2):L111–L114, February 2000. doi: 10.1086/312504.

Claude R. Canizares, John E. Davis, Daniel Dewey, Kathryn A. Flanagan, Eugene B. Galton, David P. Huenemoerder, Kazunori Ishibashi, Thomas H. Markert, Herman L. Marshall, Michael McGuirk, Mark L. Schattenburg, Norbert S. Schulz, Henry I. Smith, and Michael Wise. The Chandra High-Energy Transmission Grating: Design, Fabrication, Ground Calibration, and 5 Years in Flight. , 117(836):1144–1171, October 2005. doi: 10.1086/432898.

R. C. Carrington. Description of a Singular Appearance seen in the Sun on September 1, 1859. *MNRAS*, 20:13–15, November 1859. doi: 10.1093/mnras/20.1.13.

G. Chabrier, I. Baraffe, F. Allard, and P. Hauschildt. Evolutionary Models for Very Low-Mass Stars and Brown Dwarfs with Dusty Atmospheres. *ApJ*, 542(1):464–472, October 2000. doi: 10.1086/309513.

Paul Charbonneau. Solar Dynamo Theory. , 52:251–290, August 2014. doi: 10.1146/annurev-astro-081913-040012.

E. W. Cliver and L. Svalgaard. The 1859 Solar-Terrestrial Disturbance And the Current Limits of Extreme Space Weather Activity. *Solar Physics*, 224(1-2): 407–422, October 2004. doi: 10.1007/s11207-005-4980-z.

M. Coffaro, B. Stelzer, S. Orlando, J. Hall, T. S. Metcalfe, U. Wolter, M. Mittag, J. Sanz-Forcada, P. C. Schneider, and L. Ducci. An X-ray activity cycle on the young solar-like star ε Eridani. *A&A*, 636:A49, April 2020. doi: 10.1051/0004-6361/201936479.

M. Coffaro, B. Stelzer, and S. Orlando. X-ray activity of the young solar-like star Kepler-63 and the structure of its corona. *A&A*, 661:A79, May 2022. doi: 10.1051/0004-6361/202142298.

J. W. den Herder, A. C. Brinkman, S. M. Kahn, G. Branduardi-Raymont, K. Thomsen, H. Aarts, M. Audard, J. V. Bixler, A. J. den Boggende, J. Cottam, T. Decker, L. Dubbeldam, C. Erd, H. Goulooze, M. Güdel, P. Guttridge, C. J. Hailey, K. Al Janabi, J. S. Kaastra, P. A. J. de Korte, B. J. van Leeuwen, C. Mauche, A. J. McCalden, R. Mewe, A. Naber, F. B. Paerels, J. R. Peterson, A. P. Rasmussen, K. Rees, I. Sakelliou, M. Sako, J. Spodek, M. Stern, T. Tamura, J. Tandy, C. P. de Vries, S. Welch, and A. Zehnder. The Reflection Grating Spectrometer on board XMM-Newton. *A&A*, 365:L7–L17, January 2001. doi: 10.1051/0004-6361:20000058.

Mausumi Dikpati and Peter A. Gilman. Global solar dynamo models: Simulations and predictions. *Journal of Astrophysics and Astronomy*, 29(1-2):29–39, June 2008. doi: 10.1007/s12036-008-0004-3.

F. Favata, G. Micela, and F. Reale. The corona of the dMe flare star AD Leo. *A&A*, 354:1021–1035, February 2000. doi: 10.48550/arXiv.astro-ph/9912462.

F. Favata, G. Micela, S. Orlando, J. H. M. M. Schmitt, S. Sciortino, and J. Hall. The X-ray cycle in the solar-type star HD 81809. XMM-Newton observations and implications for the coronal structure. *A&A*, 490(3):1121–1126, November 2008. doi: 10.1051/0004-6361:200809694.

Uri Feldman. REVIEW: Elemental abundances in the upper solar atmosphere. *Phys. Scr.*, 46(3):202–220, September 1992. doi: 10.1088/0031-8949/46/3/002.

L. Fletcher, B. R. Dennis, H. S. Hudson, S. Krucker, K. Phillips, A. Veronig, M. Battaglia, L. Bone, A. Caspi, Q. Chen, P. Gallagher, P. T. Grigis, H. Ji, W. Liu, R. O. Milligan, and M. Temmer. An Observational Overview of Solar Flares. , 159(1-4):19–106, September 2011. doi: 10.1007/s11214-010-9701-8.

Howard A. Garcia. Temperature and Emission Measure from Goes Soft X-Ray Measurements. *Solar Physics*, 154(2):275–308, October 1994. doi: 10.1007/BF00681100.

L. Golub, C. Maxson, R. Rosner, G. S. Vaiana, and S. Serio. Magnetic fields and coronal heating. *ApJ*, 238:343–348, May 1980. doi: 10.1086/157990.

L. Golub, E. DeLuca, G. Austin, J. Bookbinder, D. Caldwell, P. Cheimets, J. Cirtain, M. Cosmo, P. Reid, A. Sette, M. Weber, T. Sakao, R. Kano, K. Shibasaki, H. Hara, S. Tsuneta, K. Kumagai, T. Tamura, M. Shimojo, J. McCracken, J. Carpenter, H. Haight, R. Siler, E. Wright, J. Tucker, H. Rutledge, M. Barbera, G. Peres, and S. Varisco. The X-Ray Telescope (XRT) for the Hinode Mission. *Solar Physics*, 243(1):63–86, June 2007. doi: 10.1007/s11207-007-0182-1.

Craig Gordon and Keith Arnaud. PyXspec: Python interface to XSPEC spectral-fitting program. Astrophysics Source Code Library, record ascl:2101.014, January 2021.

M. Güdel, M. Audard, F. Reale, S. L. Skinner, and J. L. Linsky. Flares from small to large: X-ray spectroscopy of Proxima Centauri with XMM-Newton. *A&A*, 416:713–732, March 2004. doi: 10.1051/0004-6361:20031471.

David H. Hathaway. The Solar Cycle. *Living Reviews in Solar Physics*, 7(1):1, December 2010. doi: 10.12942/lrsp-2010-1.

Suzanne L. Hawley and Bjorn R. Pettersen. The Great Flare of 1985 April 12 on AD Leonis. *ApJ*, 378:725, September 1991. doi: 10.1086/170474.

Suzanne L. Hawley, James R. A. Davenport, Adam F. Kowalski, John P. Wisniewski, Leslie Hebb, Russell Deitrick, and Eric J. Hilton. Kepler Flares. I. Active and Inactive M Dwarfs. *ApJ*, 797(2):121, December 2014. doi: 10.1088/0004-637X/797/2/121.

Hisashi Hayakawa, Mike Lockwood, Matthew J. Owens, Mitsuru Sôma, Bruno P. Besser, and Lidia van Driel-Gesztelyi. Graphical evidence for the solar coronal structure during the Maunder minimum: comparative study of the total eclipse drawings in 1706 and 1715. *Journal of Space Weather and Space Climate*, 11:1, June 2021. doi: 10.1051/swsc/2020035.

Todd J. Henry, Wei-Chun Jao, John P. Subasavage, Thomas D. Beaulieu, Philip A. Ianna, Edgardo Costa, and René A. Méndez. The Solar Neighborhood. XVII. Parallax Results from the CTIOPI 0.9 m Program: 20 New Members of the RECONS 10 Parsec Sample. , 132(6):2360–2371, December 2006. doi: 10.1086/508233.

N. Hurlburt, M. Cheung, C. Schrijver, L. Chang, S. Freeland, S. Green, C. Heck, A. Jaffey, A. Kobashi, D. Schiff, J. Serafin, R. Seguin, G. Slater, A. Somani, and R. Timmons. Heliophysics Event Knowledgebase for the Solar Dynamics Observatory (SDO) and Beyond. *Solar Physics*, 275(1-2):67–78, January 2012. doi: 10.1007/s11207-010-9624-2.

F. Jansen, D. Lumb, B. Altieri, J. Clavel, M. Ehle, C. Erd, C. Gabriel, M. Guainazzi, P. Gondoin, R. Much, R. Munoz, M. Santos, N. Schartel, D. Texier, and G. Vacanti. XMM-Newton observatory. I. The spacecraft and operations. *A&A*, 365:L1–L6, January 2001. doi: 10.1051/0004-6361:20000036.

Wilhelmina Maryann Joseph, Beate Stelzer, Salvatore Orlando, and Moritz Klawin. The Sun as an X-ray star V.: A new method to retrieve coronal filling factors. *arXiv e-prints*, art. arXiv:2510.23161, October 2025. doi: 10.48550/arXiv.2510.23161.

James A. Klimchuk. On Solving the Coronal Heating Problem. *Solar Physics*, 234(1):41–77, March 2006. doi: 10.1007/s11207-006-0055-z.

James A. Klimchuk. Key aspects of coronal heating. *Philosophical Transactions of the Royal Society of London Series A*, 373(2042):20140256–20140256, April 2015. doi: 10.1098/rsta.2014.0256.

T. Kosugi, K. Matsuzaki, T. Sakao, T. Shimizu, Y. Sone, S. Tachikawa, T. Hashimoto, K. Minesugi, A. Ohnishi, T. Yamada, S. Tsuneta, H. Hara,

K. Ichimoto, Y. Suematsu, M. Shimojo, T. Watanabe, S. Shimada, J. M. Davis, L. D. Hill, J. K. Owens, A. M. Title, J. L. Culhane, L. K. Harra, G. A. Doschek, and L. Golub. The Hinode (Solar-B) Mission: An Overview. *Solar Physics*, 243 (1):3–17, June 2007. doi: 10.1007/s11207-007-9014-6.

Helmut Lammer, Herbert I. M. Lichtenegger, Yuri N. Kulikov, Jean-Mathias Grießmeier, N. Terada, Nikolai V. Erkaev, Helfried K. Biernat, Maxim L. Khodachenko, Ignasi Ribas, Thomas Penz, and Franck Selsis. Coronal Mass Ejection (CME) Activity of Low Mass M Stars as An Important Factor for The Habitability of Terrestrial Exoplanets. II. CME-Induced Ion Pick Up of Earth-like Exoplanets in Close-In Habitable Zones. *Astrobiology*, 7(1):185–207, February 2007. doi: 10.1089/ast.2006.0128.

David H Lumb, Norbert Schartel, and Fred A Jansen. XMM-Newton (X-Ray Mulit-Mirror Mission) Observatory. *arXiv e-prints*, art. arXiv:1202.1651, February 2012. doi: 10.48550/arXiv.1202.1651.

A. Maggio, J. J. Drake, V. Kashyap, F. R. Harnden, Jr., G. Micela, G. Peres, and S. Sciortino. X-Ray Spectroscopy of the Unsteady Quiescent Corona of AD Leonis with Chandra. *ApJ*, 613(1):548–566, September 2004. doi: 10.1086/422904.

D. E. McKenzie. Supra-arcade downflows in long-duration solar flare events. *Solar Physics*, 195:381–399, 2000.

Y.-J. Moon, G. S. Choe, H. Wang, and Y. D. Park. Sympathetic coronal mass ejections. *The Astrophysical Journal*, 588:1176–1184, 2003.

Kosuke Namekata, Takahito Sakaue, Kyoko Watanabe, Ayumi Asai, Hiroyuki Maehara, Yuta Notsu, Shota Notsu, Satoshi Honda, Takako T. Ishii, Kai Ikuta, Daisaku Nogami, and Kazunari Shibata. Statistical Studies of Solar White-light Flares and Comparisons with Superflares on Solar-type Stars. *ApJ*, 851 (2):91, December 2017. doi: 10.3847/1538-4357/aa9b34.

Donald F. Neidig. The Importance of Solar White-Light Flares. *Solar Physics*, 121(1-2):261–269, March 1989. doi: 10.1007/BF00161699.

J. U. Ness, M. Güdel, J. H. M. M. Schmitt, M. Audard, and A. Telleschi. On the sizes of stellar X-ray coronae. *A&A*, 427:667–683, November 2004. doi: 10.1051/0004-6361:20040504.

Y. Ogawara, T. Takano, T. Kato, T. Kosugi, S. Tsuneta, T. Watanabe, I. Kondo, and Y. Uchida. The SOLAR-A Mission - An Overview. *Solar Physics*, 136(1): 1–16, November 1991. doi: 10.1007/BF00151692.

S. Orlando, G. Peres, and F. Reale. The Sun as an X-Ray Star. I. Deriving the Emission Measure Distribution versus Temperature of the Whole Solar Corona from theYohkoh/Soft X-Ray Telescope Data. *ApJ*, 528(1):524–536, January 2000. doi: 10.1086/308137.

S. Orlando, G. Peres, and F. Reale. The Sun as an X-Ray Star. IV. The Contribution of Different Regions of the Corona to Its X-Ray Spectrum. *ApJ*, 560(1): 499–513, October 2001. doi: 10.1086/322333.

S. Orlando, G. Peres, and F. Reale. The Sun as an X-ray star: Active region evolution, rotational modulation, and implications for stellar X-ray variability. *A&A*, 424:677–689, September 2004. doi: 10.1051/0004-6361:20040207.

S. Orlando, F. Favata, G. Micela, S. Sciortino, A. Maggio, J. H. M. M. Schmitt, J. Robrade, and M. Mittag. Fifteen years in the high-energy life of the solar-type star HD 81809. XMM-Newton observations of a stellar activity cycle. *A&A*, 605:A19, September 2017. doi: 10.1051/0004-6361/201731301.

Rachel A. Osten, Suzanne L. Hawley, Joel Allred, Christopher M. Johns-Krull, Alexander Brown, and Graham M. Harper. From Radio to X-Ray: The Quiescent Atmosphere of the dMe Flare Star EV Lacertae. *ApJ*, 647(2):1349–1374, August 2006. doi: 10.1086/504889.

G. Peres, S. Orlando, F. Reale, R. Rosner, and H. Hudson. The Sun as an X-Ray Star. II. Using theYohkoh/Soft X-Ray Telescope-derived Solar Emission Measure versus Temperature to Interpret Stellar X-Ray Observations. *ApJ*, 528(1):537–551, January 2000. doi: 10.1086/308136.

N. Pizzolato, A. Maggio, G. Micela, S. Sciortino, and P. Ventura. The stellar activity-rotation relationship revisited: Dependence of saturated and non-saturated X-ray emission regimes on stellar mass for late-type dwarfs. *A&A*, 397:147–157, January 2003. doi: 10.1051/0004-6361:20021560.

D. Porquet, R. Mewe, J. Dubau, A. J. J. Raassen, and J. S. Kaastra. Line ratios for helium-like ions: Applications to collision-dominated plasmas. *A&A*, 376: 1113–1122, September 2001. doi: 10.1051/0004-6361:20010959.

D. Porquet, J. Dubau, and N. Grosso. He-like Ions as Practical Astrophysical Plasma Diagnostics: From Stellar Coronae to Active Galactic Nuclei. , 157 (1-4):103–134, December 2010. doi: 10.1007/s11214-010-9731-2.

F. Reale, R. Betta, G. Peres, S. Serio, and J. McTiernan. Determination of the length of coronal loops from the decay of X-ray flares I. Solar flares observed with YOHKOH SXT. *A&A*, 325:782–790, September 1997.

F. Reale, G. Peres, and S. Orlando. The Sun as an X-Ray Star. III. Flares. *ApJ*, 557 (2):906–920, August 2001. doi: 10.1086/321598.

Fabio Reale. Coronal Loops: Observations and Modeling of Confined Plasma. *Living Reviews in Solar Physics*, 11(1):4, December 2014. doi: 10.12942/lrsp-2014-4.

Katharine K. Reeves, Harry P. Warren, and Terry G. Forbes. Theoretical Predictions of X-Ray and Extreme-UV Flare Emissions Using a Loss-of-Equilibrium Model of Solar Eruptions. *ApJ*, 668(2):1210–1220, October 2007. doi: 10.1086/521291.

R. Rosner, W. H. Tucker, and G. S. Vaiana. Dynamics of the quiescent solar corona. *ApJ*, 220:643–645, March 1978. doi: 10.1086/155949.

S. H. Saar and J. L. Linsky. The photospheric magnetic field of the dM3.5e flare star AD Leonis. *ApJ*, 299:L47–L50, December 1985. doi: 10.1086/184578.

J. Sanz-Forcada and G. Micela. The EUVE point of view of AD Leo. *A&A*, 394: 653–661, November 2002. doi: 10.1051/0004-6361:20021158.

C. J. Schrijver and A. M. Title. Long-range magnetic couplings between solar flares and coronal mass ejections. *Journal of Geophysical Research: Space Physics*, 116:A04108, 2011. doi: 10.1029/2010JA016224.

Bennet D. Schwab, Robert H. A. Sewell, Thomas N. Woods, Amir Caspi, James Paul Mason, and Christopher Moore. Soft X-Ray Observations of Quiescent Solar Active Regions Using the Novel Dual-zone Aperture X-Ray Solar Spectrometer. *ApJ*, 904(1):20, November 2020. doi: 10.3847/1538-4357/abba2a.

Bennet D. Schwab, Thomas N. Woods, and James Paul Mason. Modeling the Daily Variations of the Coronal X-ray Spectral Irradiance with Two Temperatures and Two Emission Measures. *ApJ*, 945(1):31, March 2023. doi: 10.3847/1538-4357/acb774.

Antígona Segura, Lucianne M. Walkowicz, Victoria Meadows, James Kasting, and Suzanne Hawley. The Effect of a Strong Stellar Flare on the Atmospheric Chemistry of an Earth-like Planet Orbiting an M Dwarf. *Astrobiology*, 10(7): 751–771, September 2010. doi: 10.1089/ast.2009.0376.

Jr. Sheeley, N. R., J. D. Bohlin, G. E. Brueckner, J. D. Purcell, V. E. Scherrer, and R. Tousey. The reconnection of magnetic field lines in the solar corona. *The Astrophysical Journal Letters*, 196:L129–L131, 1975.

Randall K. Smith, Nancy S. Brickhouse, Duane A. Liedahl, and John C. Raymond. Collisional Plasma Models with APEC/APED: Emission-Line Diagnostics of Hydrogen-like and Helium-like Ions. *ApJ*, 556(2):L91–L95, August 2001. doi: 10.1086/322992.

Y. L. Song, H. Tian, M. Zhang, and M. D. Ding. Observations of white-light flares in NOAA active region 11515: high occurrence rate and relationship with magnetic transients. *A&A*, 613:A69, June 2018. doi: 10.1051/0004-6361/201731817.

B. Stelzer, M. Caramazza, S. Raetz, C. Argiroffi, and M. Coffaro. The Great Flare of 2021 November 19 on AD Leonis. Simultaneous XMM-Newton and

TESS observations. *A&A*, 667:L9, November 2022. doi: 10.1051/0004-6361/202244642.

F. R. Stephenson, J. E. Jones, and L. V. Morrison. The solar eclipse observed by Clavius in A.D. 1567. *A&A*, 322:347–351, June 1997.

L. Strüder, U. Briel, K. Dennerl, R. Hartmann, E. Kendziorra, N. Meidinger, E. Pfeffermann, C. Reppin, B. Aschenbach, W. Bornemann, H. Bräuninger, W. Burkert, M. Elender, M. Freyberg, F. Haberl, G. Hartner, F. Heuschmann, H. Hippmann, E. Kastelic, S. Kemmer, G. Kettenring, W. Kink, N. Krause, S. Müller, A. Oppitz, W. Pietsch, M. Popp, P. Predehl, A. Read, K. H. Stephan, D. Stötter, J. Trümper, P. Holl, J. Kemmer, H. Soltau, R. Stötter, U. Weber, U. Weichert, C. von Zanthier, D. Carathanassis, G. Lutz, R. H. Richter, P. Solc, H. Böttcher, M. Kuster, R. Staubert, A. Abbey, A. Holland, M. Turner, M. Balasini, G. F. Bignami, N. La Palombara, G. Villa, W. Buttler, F. Gianini, R. Lainé, D. Lumb, and P. Dhez. The European Photon Imaging Camera on XMM-Newton: The pn-CCD camera. *A&A*, 365:L18–L26, January 2001. doi: 10.1051/0004-6361:20000066.

Aki Takeda, Keiji Yoshimura, and Steven H. Saar. The Hinode/XRT Full-Sun Image Corrections and the Improved Synoptic Composite Image Archive. *Solar Physics*, 291(1):317–333, January 2016. doi: 10.1007/s11207-015-0823-8.

Neil R. Thomson, Craig J. Rodger, and Richard L. Dowden. Ionosphere gives size of greatest solar flare. , 31(6):L06803, March 2004. doi: 10.1029/2003GL019345.

D. Tripathi, V. Bothmer, and H. Cremades. The basic characteristics of euv post-eruptive arcades and their role as tracers of coronal mass ejection source regions. *Astronomy and Astrophysics*, 422:337–349, 2004. doi: 10.1051/0004-6361:20035815.

Joy Velasquez, Nicholas Murphy, Katharine Reeves, Jonathan Slavin, Mark Weber, and Will Barnes. XRTpy: A Hinode-X-Ray Telescope Python Package. *The Journal of Open Source Software*, 9(100):6396, August 2024. doi: 10.21105/joss.06396.

A. Vourlidas, R. A. Howard, E. Esfandiari, S. Patsourakos, S. Yashiro, and G. Michalek. Comprehensive Analysis of Coronal Mass Ejection Mass and Energy Properties Over a Full Solar Cycle. *ApJ*, 722(2):1522–1538, October 2010. doi: 10.1088/0004-637X/722/2/1522.

Z. Švestka. The Phase of Particle Acceleration in the Flare Development. *Solar Physics*, 13(2):471–489, August 1970. doi: 10.1007/BF00153567.

Martin C. Weisskopf, Harvey D. Tananbaum, Leon P. Van Speybroeck, and Stephen L. O'Dell. Chandra X-ray Observatory (CXO): overview. In Joachim E. Truemper and Bernd Aschenbach, editors, *X-Ray Optics, Instruments, and Missions III*, volume 4012 of *Society of Photo-Optical Instrumentation Engineers (SPIE) Conference Series*, pages 2–16, July 2000. doi: 10.1117/12.391545.

Andrew A. West, Suzanne L. Hawley, John J. Bochanski, Kevin R. Covey, I. Neill Reid, Saurav Dhital, Eric J. Hilton, and Michael Masuda. Constraining the Age-Activity Relation for Cool Stars: The Sloan Digital Sky Survey Data Release 5 Low-Mass Star Spectroscopic Sample. , 135(3):785–795, March 2008. doi: 10.1088/0004-6256/135/3/785.

Thomas N. Woods, Bennet Schwab, Robert Sewell, Anant Kumar Telikicherla Kandala, James Paul Mason, Amir Caspi, Thomas Eden, Amal Chandran, Phillip C. Chamberlin, Andrew R. Jones, Richard Kohnert, Christopher S. Moore, Stanley C. Solomon, and Harry Warren. First Results for Solar Soft X-Ray Irradiance Measurements from the Third-generation Miniature X-Ray Solar Spectrometer. *ApJ*, 956(2):94, October 2023. doi: 10.3847/1538-4357/acef13.

XMM-Newton Science Operations Centre. *XMM-Newton Users Handbook*. European Space Agency (ESA), issue 2.23 edition, 2025. URL `https://xmm-tools.cosmos.esa.int/external/xmm_user_support/documentation/uhb/XMM_UHB.pdf`. Online; accessed <your access date>.

S. Yashiro, N. Gopalswamy, S. Akiyama, G. Michalek, and R. A. Howard. Visibility of coronal mass ejections as a function of flare location and intensity.

Journal of Geophysical Research (Space Physics), 110(A12):A12S05, December 2005. doi: 10.1029/2005JA011151.